

Quantitative analysis of the focused ultrasound-induced blood-brain barrier opening with
applications in neurodegenerative disorders

Maria Eleni Karakatsani

Submitted in partial fulfillment of the
requirements for the degree of
Doctor of Philosophy
in the Graduate School of Arts and Sciences

COLUMBIA UNIVERSITY

2020

Maria Eleni Karakatsani

© 2020

ALL RIGHTS RESERVED

Abstract

Quantitative analysis of the focused ultrasound-induced blood-brain barrier opening with applications in neurodegenerative disorders

Maria Eleni Karakatsani

The blood-brain barrier poses a formidable impediment to the treatment of adult-onset neurodegenerative disorders, by prevention of most drugs from gaining access to the brain parenchyma. Focused ultrasound (FUS), in conjunction with systemically administered microbubbles, has been shown to open the blood-brain barrier (BBB) locally, reversibly and non-invasively both in rodents and in non-human-primates. Initially, we demonstrate a monotonic increase of the BBB opening volume with close to normal incidence angle, detectable by diffusion tensor imaging; the employed contrast-free magnetic resonance protocol that revealed the anisotropic nature of the diffusion gradient. Implementation of this optimized BBB opening technique in Parkinsonian mice, coupled with the administration of trophic growth factors, induced restorative effects in the dopaminergic neurons, the main cellular target of the pathological process in Parkinson's disease. The immune response initiated by the FUS-induced BBB disruption has been proven pivotal in reducing proteinaceous aggregates from the brain through the activation of a gliosis cascade. Therefore, we investigated this immunomodulatory effect in Alzheimer's disease. The neuropathological hallmarks of Alzheimer's disease include aggregation of amyloid beta into plaques and accumulation of tau protein into neurofibrillary tangles. Tau pathology correlates well with impaired neuronal activity and dementia and was found to be attenuated after the application of ultrasound that correlated with increased microglia

activity. Given the beneficial effect of this methodology on the Alzheimer's pathologies when studied separately, we explored the application of FUS in brains subjected concurrently to amyloidosis and tau phosphorylation. Our findings indicate the reduction of tau protein and decrease in the amyloid load from brains treated with ultrasound, accompanied by spatial memory improvement. Overall, in this dissertation, we established an optimized targeting and detection protocol, pre-clinical implementation of which confirmed its ameliorative effects as a drug-delivery adjuvant or an immune response stimulant. These preclinical findings support the immense potential of such a methodology that significantly contributes to the treatment of different neurodegenerative disorders curbing their progression.

Table of Contents

List of Figures	iv
List of Tables	xix
Abbreviations	xx
Acknowledgements	xxiii
Chapter 1. Background and Motivation.....	1
1.1 Central nervous system barriers	1
1.2 The blood-brain barrier	1
1.3 Neurodegenerative disorders.....	5
1.3.1 Alzheimer’s disease	5
1.3.2 Parkinson’s disease.....	6
1.4 Focused ultrasound.....	7
Chapter 2: Specific Aims	17
Chapter 3: Optimization of the focused ultrasound targeting and the blood-brain barrier opening detection.....	19
3.1 Targeting effects on the volume of the focused ultrasound-induced blood-brain barrier opening in non-human primates in vivo.	19
3.1.1 Abstract.....	19
3.1.2 Introduction	20
3.1.3 Materials and Methods	22
3.1.4 Results and Discussion	29
3.1.5 Limitations and Conclusions	33

3.2	Contrast-free detection of the focused ultrasound-induced blood-brain barrier opening with magnetic resonance imaging in non-human primates, in vivo.	35
3.2.1	Abstract.....	35
3.2.2	Introduction	36
3.2.3	Materials and Methods	39
3.2.4	Results and Discussion	47
3.2.5	Limitations and Conclusions	52
3.3	Contribution	53
Chapter 4: Focused ultrasound-facilitated neurotrophic delivery in an early-stage Parkinsonian mouse model.		
4.1	Abstract	56
4.2	Introduction	57
4.3	Materials and Methods	59
4.4	Results and Discussion.....	67
4.5	Limitations and Conclusions.....	82
4.6	Contribution	84
Chapter 5: Focused ultrasound-induced blood-brain barrier opening initiates pathological changes in two different Alzheimer’s mouse models.		
5.1	Unilateral focused ultrasound-induced blood-brain barrier opening reduces phosphorylated tau from the rTg4510 tauopathy mouse model.	86
5.1.1	Abstract.....	86
5.1.2	Introduction	87
5.1.3	Materials and Methods	89

5.1.4	Results and Discussion	98
5.1.5	Limitations and Conclusions	111
5.2	Focused ultrasound-induced blood-brain barrier opening initiates pathological changes in the 3xTg-Alzheimer's mouse model.....	113
5.2.1	Abstract.....	113
5.2.2	Introduction	114
5.2.3	Materials and Methods	117
5.2.4	Results and Discussion	126
5.2.5	Limitations and Conclusions	133
5.3	Contribution	135
Chapter 6: Conclusion and Future Work		137
References.....		144

List of Figures

Figure 1: The central nervous system barriers. a. The blood-brain barrier between the brain parenchyma and the blood lumen. b. The blood-CSF barrier at the Choroid plexus. c. The meningeal barriers consisted of the arachnoid barrier between the CSF in the subarachnoid space and the overlying structures, as well as the PIA/glia limitans barrier and the brain parenchyma. d. The CSF-brain barrier is important only in the embryo while it is governed by free exchange in the adult brain⁴..... 2

Figure 2: The neurovascular unit. The capillary is surrounded by an endothelial cell, with its two ends connected by a tight junction, and ensheathed by astrocytic processes. The pericytes are located in the basal lamina space while the microglia in the interstitial fluid of the extracellular compartment⁷..... 4

Figure 3: Alzheimer's pathology is characterized by the accumulation of amyloid- β in plaques (brown) in the brain parenchyma and intraneuronal aggregation of hyperphosphorylated tau into neurofibrillary tangles (blue). Image courtesy of the National Institute on Aging/National Institutes of Health..... 6

Figure 4: The nigrostriatal pathway describes the dopaminergic neuron (orange) and the structures involved. The neuronal cells lie in the substantia nigra pars compacta region (SNpc in green) with their axons innervating the striatum (blue). Figure generated utilizing the Allen Institute library..... 8

Figure 5: Left: Representative confocal image revealing close interaction between microglia (Iba1, green) and endothelial cells (IsolectinB4, red) ⁷⁸ . Right: Representative confocal image showing the proximity of the microglia (Iba1, purple) to the area of biocytin-TMR leakage (red) from the vessels (Glut1, white) following FUS-induced BBB opening (T. Kugelman et al. <i>submitted</i>).....	14
Figure 6: Microglia phenotypes during the phases of neurodegeneration ⁸⁰	15
Figure 7: Overview of the research conducted in the field of sonication optimization and application.....	17
Figure 8: Overview of the specific aims in terms of the optimization and application fields.	18
Figure 9: a. 3D representation of the NHP skull obtained from the CT. The transducer in solid color is aligned with the skull in a matching curvature regimen while the transparent transducers represent cases of not aligned curvatures. Aligned curvatures result in sonications with normal incidence angle. b. 3D reconstruction of the BBB opening with the focal region of the axial vector (red cylinder), the tangent plane on the skull (green plane) and the incidence angle (α) projected. c. Schematic of the skull and definitions of the abbreviations used. d. Closer look at the schematic to define the incidence angle. e. Closer look at the schematic to define the skull thickness factor, sf, for two different incidence angles. f. Closer look at the schematic to define the refraction angle.	26

Figure 10: a. Linear regression of the opening volume with increasing incidence angle at three different pressures. The variables are listed in the table preceding the graphs. b. Linear regression of the opening volume with increasing pressure at three different incidence angles. The variables are listed in the table preceding the graphs. c. Repeatability of the opening volume at fixed pressure and incidence angles. The variables are listed in the table preceding the graphs. 30

Figure 11: a. Qualitative results showing increase of the volume of opening with incidence angle for fixed pressure, 0.4MPa. The NHP in the blue outline was sonicated at $73 \pm 1.5^\circ$ yielding an opening of $142 \pm 20 \text{ mm}^3$ while the NHP in the red outline yielded an opening of $481 \pm 30 \text{ mm}^3$ when sonicated at $88 \pm 1.2^\circ$. b. Brain images showing the increase of the volume of opening with pressure given a constant incidence angle, $76 \pm 1.5^\circ$. The NHP in the blue outline was sonicated at 0.35 MPa and yielded an opening of $246 \pm 22 \text{ mm}^3$ while the NHP in the red outline was sonicated at 0.6MPa yielding an opening of $854 \pm 50 \text{ mm}^3$. c. Qualitative results showing the repeatability of the technique. Both NHPs were sonicated at $84 \pm 0.19^\circ$ and 0.3MPa and yielded openings of $451 \pm 60 \text{ mm}^3$ and $440 \pm 60 \text{ mm}^3$ respectively..... 31

Figure 12: Numerical simulations with increasing incidence angle and constant pressure at 0.3 MPa, Axial and lateral profile for the five angles respectively, 78.46, 80.784, 82.21, 86.19 and 88.02. The PNP field was normalized with the maximum pressure across simulations..... 32

Figure 13: a. Transducer orientation relative to the brain fixed on the stereotactic frame. b. Gradient direction coordinates are presented to confirm that diffusion sampling occurred in the entire sphere, a requirement imposed by the eddy current correction accuracy. c. Flowchart of the

DTI processing pipeline. The raw data were transformed from DICOM to NIFTI format and all the directions were registered to the weight- and gradient-free image of the scan acquired before the sonications. The registered images were combined in a 4D format that was isolated from the surrounding brain tissue and corrected for eddy current artifacts. Then, the calculation of the tensor and the corresponding eigenvalues and eigenvectors resulted from the DTIFIT. The mean diffusivity and the fractional anisotropy maps were quantified by employing the appropriate equations. The difference in the FA values is reported herein, denoted as ΔFA , and resulted from the subtraction of the FA map obtained before the sonication from the FA map acquired following the sonication..... 41

Figure 14: BBB detection with Gadolinium-Enhanced T1-weighted imaging and FA maps. Each case corresponds to a different experiment conducted on the same animal targeting a similar structure (Caudate nucleus). The T1-weighted images' ratio, $RGd-T1$, is presented against the difference in FA maps, ΔFA . Longitudinal assessment of the opening surface area shows comparability of the two modalities both qualitatively and quantitatively. Accordingly, the average BBB opening surface area is similar between modalities. The FA value increased in all four cases following the sonication while increased on average by 82% from 0.21 ± 0.02 to 0.38 ± 0.03 ($t[3]=27.73$; $P=0.0001$). 49

Figure 15: DTI eigenvectors overlaid onto the ΔFA map for the entire axial brain plane and the magnified striatal region. BBB opening initiates an increase in the directionality of the water molecule diffusion compared to the intact barrier shown by the consistent direction of the arrows in the sonicated area compared to the contralateral side. Polar and azimuthal angle distributions

in the ipsilateral and contralateral hemispheres are presented showing the narrow range of polar and azimuthal angles of the principal eigenvector only at the site of sonication ($V_{IPOST-IPSI}$). Cumulative results showed a decrease in the polar angle range on the order of 35.58% ($t[3]=3.921$; $P=0.0295$) compared to the ipsilateral side, $V_{IPRE-IPSI}$, and 53.86% ($t[3]=4.887$; $P=0.0164$) compared to the contralateral side, $V_{IPOST-CONTRA}$. Similarly, the azimuthal angle range of the $V_{IPOST-IPSI}$ decreased by 82.44% ($t[3]=3.699$; $P=0.0343$) compared to $V_{IPRE-IPSI}$, and 84.55% ($t[3]=7.462$; $P=0.005$) compared $V_{IPOST-CONTRA}$ 52

Figure 16: Upregulation of the dopaminergic pathway following focused ultrasound-facilitated drug delivery. The dopaminergic pathway can be downregulated similar to Parkinson's disease in toxin-based mouse models. Application of focused ultrasound results in increased blood-brain barrier permeability allowing the diffusion of pharmacological agents in the brain. Depending on the number of administrations and the delivery vehicle, the deliverable compounds can have beneficial effects of varying degree. 57

Figure 17: The MPTP effect. a. The timeline shows degeneration following MPTP application and the interval until immunohistochemistry was performed. b. Representative coronal images of the SNc for control and MPTP injected groups. SNc cell body quantification for each brain hemisphere is presented. A ~22% reduction of SNc TH⁺ cell body number is observed in the MPTP- vs saline-injected mice (two-way ANOVA for $n=7$, $F[1, 12] = 3.191$; $P=0.0993$). c. Higher magnification (4x) images focusing on the SNr shows a loss of fibers of ~33% in MPTP- vs. saline-injected mice (two-way ANOVA for $n=5$, $F[1, 8] = 5.335$; $P=0.0497$). The area quantification is presented per hemisphere and per brain. d. Representative images of the CPu

TH+ terminal density for the saline and MPTP groups showing a ~40% reduction of CPu TH+ immunoreactivity in MPTP- vs saline-injected mice (two-way ANOVA for $n=5$, $F[1, 8] = 25.64$; $P=0.0010$). Area quantification shows the decrease in TH+ immunoreactivity for the MPTP mice per side per brain..... 69

Figure 18: Neurorestoration effect at the level of the SN. a. Single treatment at the SN: The descriptive timeline of the procedure is followed by representative TH immunohistochemistry images. The plus/minus signs indicate whether the corresponding side of the brain received MPTP, FUS and NTN. b. Triple treatment at the level of the SN: The corresponding timeline provides information regarding the additional steps followed for this part of the study. The plus/minus signs indicate whether the brains received MPTP, FUS and NTN and the three plus signs denote the times the treatment was repeated. c. Cell body counts at the level of the SNc region. Results are shown as the relative ratio by dividing the contralateral side into the ipsilateral side. The statistical significance occurs with one-way ANOVA ($n=5-7$; $F[4, 27] = 8.892$; $P=0.0001$) after correcting the multiple measurements with Newman-Keuls method. d. The area quantification of the fibrotic density at the SNr region. The results are shown as the relative ratio by dividing the contralateral side into the ipsilateral side. The statistical significance occurs with one-way ANOVA ($n=5-7$; $F[4, 22] = 11.31$; $P<0.0001$) after correcting the multiple measurements with Newman-Keuls method. 72

Figure 19: Neurorestoration effect at the Caudate-Putamen (CPu) region. a. The descriptive timeline of the procedure is followed by representative TH immunohistochemistry images. The pixels surpassing a certain threshold are presented in dark red to enhance the differences between

the ipsilateral and contralateral side. The plus/minus signs indicate whether the corresponding side of the brain received MPTP, FUS and NTN. b. Triple treatment at the CPu: The corresponding timeline provides information regarding the additional steps followed for this part of the study. The plus/minus signs indicate whether the brains received MPTP, FUS and NTN and the three plus signs denote the number of times the treatment was repeated. c. The area quantification of the terminal density at the CPu region. Results are shown as the relative ratio by dividing the contralateral side into the ipsilateral side. The statistical significance occurs with one-way ANOVA ($n=5-7$; $F[4, 24] = 3.527$; $P=0.0212$) after correcting the multiple measurements with Newman-Keuls method permeate the CPu as effectively as in the SNr, it may be that the stronger regimen of FUS/NTN is required to achieve the desired effect. Furthermore, within the CPu, TH-positive fibers represent less than 10% of the fiber pool hence, most of the NTN molecules in the CPu might interact with neuronal structures other than TH-positive fibers.

..... 75

Figure 20: FUS-facilitated AAV-GDNF delivery induced neuronal upregulation in MPTP mice. a. Experimental timeline where MPTP was given first followed by sonication and a 12-week survival period. Behavioral studies were performed 1 week prior to sonication and repeated at the end of the survival period. b. TH staining of the SN region in mice receiving a combination of AAV/FUS treatments ($n=6-10$). c. TH⁺ neurons were counted and intra-group comparisons were made. Significantly higher number of TH⁺ neurons were found on the AAV+/FUS+ side of the brain compared to the contralateral side. d. TH⁺ dendrite density was calculated and intra-group comparisons were performed. Significantly higher dendrite density was observed on the AAV+/FUS+ side of the brain. e. Immunofluorescent TH staining revealed much more

dopaminergic projections on the AAV+/FUS+ side of the brain. Dendritic densities of the SN region were compared across groups and significantly higher dendritic fiber network ($n=4-5$; $F[3, 13] = 7.514$; $P=0.0036$) was identified comparing AAV+/FUS+ to the MPTP group. f. TH staining of the striatum illustrates the ameliorated dopaminergic projections on the AAV+/FUS+ hemisphere. Quantitative analysis of the optical density ratio demonstrated significant difference ($n=4-5$; $F[3, 17] = 4.733$; $P=0.014$) between the AAV+/FUS+ to the MPTP group. g. Amphetamine-elicited behavioral studies revealed more frequent clockwise (toward the remaining lesion side) rotation, signifying more prominent dopaminergic function on the hemisphere receiving AAV+/FUS+ treatment. 80

Figure 21: Quantification algorithms. (a) The structural algorithm performed color-based segmentation with k-means clustering on the red channel filtering out weaker intensities. The Hough transform detected the cells as bright circular objects on a dark background, providing their total count and the corresponding coordinates. Singular value decomposition (SVD) was used to filter the image followed by morphological operators that skeletonized and revealed the spine of the process. The coordinates of each cell were then used to initiate a stemming process search until an endpoint was reached. The distance of the endpoint to the cell center was measured. (b) The intensity algorithm utilized the composite image as input to generate a hippocampal mask, omitting the irrelevant neighboring structures. The mask was applied to all three channels separately followed by color-based segmentation via k means clustering. For every channel the density is reported as the ratio of the pixels belonging to the cluster with the highest value over the pixels constituting the entire hippocampal mask. Scale bar, 100 μ m. 95

Figure 22: Volumetric analysis of the blood-brain barrier opening from the contrast-enhanced T1-weighted MR coronal images. The volumes of the transgenic animals were at the order of $54.8 \pm 2.02 \text{ mm}^3$, $52.46 \pm 6.59 \text{ mm}^3$, $54.22 \pm 7.44 \text{ mm}^3$ and $52.5 \pm 5.64 \text{ mm}^3$, while $52.83 \pm 8.81 \text{ mm}^3$, $54.98 \pm 5.97 \text{ mm}^3$, $55.48 \pm 3.75 \text{ mm}^3$ and $54.49 \pm 9.76 \text{ mm}^3$ of the wild-type mice for the four consecutive weeks. Longitudinal analysis did not show any significant difference across weeks. Additionally, the opening volumes did not differ between transgenic and wild-type animals within the same week interval. 99

Figure 23: The timeline of the experimental procedure is shown at the top. Briefly, five mice of the rTg4510 line at 3.5 months of age were recruited for four sonications, once per week and were sacrificed a day after the last treatment. MRI was performed after each sonication to confirm targeting accuracy and successful opening. Two slices per transgenic brain were counterstained for neuronal cells with the anti-NeuN and anti- β -tubulin III antibodies along with brain slices from a wild-type mouse to assess neuronal integrity. Neuronal compromise could be qualitatively observed in transgenic animals compared to healthy mice by the decrease in the NeuN signal and the non-uniform signal emitted by the neuronal processes. However, no significant differences emerged from the application of ultrasound as shown by the quantitative measures. The mean (\pm standard deviation) neuronal cell density was $39.18 \pm 4.25 \%$ and $36.46 \pm 3.77\%$, for the sham contralateral and ipsilateral side while $37.87 \pm 4.14\%$ and $39.18 \pm 4.09\%$ for the corresponding sides of the sonicated brains. Respectively, the mean value (\pm standard deviation) for the neuronal processes density was $39.31 \pm 1.91\%$ and $39.43 \pm 2.93\%$ for the sham contralateral and ipsilateral side while $38.25 \pm 2.13\%$ and $39.56 \pm 3.3\%$ for the corresponding sides of the sonicated brains. Scale bar, $100\mu\text{m}$ 102

Figure 24: The timeline of the experimental procedure. For this immunohistochemical analysis brain slices from the transgenic animals were counterstained for phosphorylated tau with the AT8 antibody and immune cell activation with the CD68 antibody while imaged by confocal microscopy. (b) Representative composite images of the sham and sonicated ipsilateral hemispheres are shown with the red channel corresponding to the signal emitted from phosphorylated tau, the green channel reflecting the immune response and the blue channel representing the cell-dye Hoechst 33342. (c) Bar scatter plot representation of the samples showing a significant reduction in the p-tau signal when comparing the hemispheres of the sham and the sonicated brain. In particular, we observed a reduction in the p-tau signal on the order of 57.35% ($F[1,8] = 34.32; P=0.0004$) when comparing the contralateral hemispheres of the sham and the sonicated brains, while 72.65% ($F[1,8] = 34.32; P<0.0001$) when comparing the ipsilateral hemispheres. (d) On the other hand, the total cell numbers detected by the algorithm did not differ among the groups or the hemispheres (e) Immune cell activation was confirmed by the signal obtained from the CD68 marker. Immune system upregulation was expected due to pathology but a 54.41% increase ($F[1,8] = 46.4; P<0.0001$) was observed in the hemisphere treated with ultrasound while a 41.6% ($F[1,8] = 46.4; P=0.0064$) increase in its contralateral side compared to the control brains. (f) Regression analysis between the p-tau signal and the immune cell activation yielded a significant deviation of the slope from the zero value suggesting a correlation between the two parameters ($r^2=0.3285; \beta=-2.136; P<0.0001$). Scale bar, 100 μ m. 104

Figure 25: (a) Phosphorylated tau signal emitted from the affected pyramidal neurons of the ipsilateral and contralateral side in the CA1 sector of the sham and sonicated brains. (b)

Comparison of the cumulative density function (CDF) of the p-tau processes length as obtained from each group (sham contra, sham ipsi, sonic contra and sonic ipsi). This graph describes the probability (y-axis) of finding p-tau processes of a certain or smaller length (x-axis). The 95th percentile (upper red line) crosses the CDF of the sonicated ipsilateral side at 300 μ m (dotted red line), while at 700 μ m (dotted red line) for the untreated brain. This finding suggests that the probability of finding a p-tau neuronal process equal or smaller than 300 μ m in the sonicated brain and 700 μ m in the unsonicated brain is 0.95. (c) The cumulative density function of the difference in p-tau processes length between the sham and sonicated hemisphere (ipsi sham-ipsi sonic). The zero crossing denote the probability of p-tau processes having the same length between the two hemispheres. From this CDF it can be observed that 68% of the neurons on the sham ipsilateral side are longer than those on the sonicated ipsilateral side. Scale bar, 100 μ m. 107

Figure 26: Microglia colocalization with phosphorylated tau protein. For this immunohistochemical analysis, two brain slices from the transgenic animals were counterstained for phosphorylated tau and microglia presence with the AT8 (red) and the Iba1 (green) antibody. Three Z-stack series were captured on a 60x objective covering the CA1 region. (a-d) Qualitative evaluation of the biomarker colocalization. The three planes, XY (main), XZ and YZ (orthogonal) are presented for a microglia cell. The images are magnified versions of the 60x objective and the corresponding video included in the Supplementary Material. (a, c) The microglia are shown to verge on the phosphorylated tau but not engulf it as indicated by the lack of the channel overlap in all three planes. (b, d) The microglia seem to engulf fragments of phosphorylated tau after the application of ultrasound in both hemispheres of the sonicated brains. The overlap of the two channels is consistent in all three planes. (e-h) The four panels

follow the same structure: a composite image showing the merged and monochromatic images of the isolated CA1 sector and the scatterplot of the two channels. The scatterplot colormap indicates the pixels density. (e) The neuronal processes are largely affected by phosphorylated tau while the presence of microglia is evident in the ipsilateral sham hemisphere. The scatterplot has a slope (the slope obtained by performing linear regression between the two channels) of 0.022 suggesting that more pathological tau is present (higher red channel values) than microglia (smaller green channel values) while Pearson's correlation coefficient (PCC) is 0.0345 suggesting minor statistical dependence between the biomarkers. (f) The sonicated hemisphere experienced a reduction in phosphorylated tau and an increase in microglia presence indicated by the higher value of the fitted slope equal to 0.207, while the PCC increased for this case to 0.068. (g) Similar findings to the ipsilateral hemisphere can be extracted from the contralateral sides where the slope is 0.038 and the PCC of 0.058 in the sham brain while (h) the slope reached 0.122 and the PCC 0.068 in the sonicated brain. (i-l) Cumulative results on the dependency metrics. Comparable PCC values suggest that ultrasound did not affect the covariance of the two biomarkers. However, a significant increase in the slope of the linear regression line by 43% can be observed between the ipsilateral hemispheres ($F[1.6]=6.214; P=0.047$). Furthermore, the percent of red-to-green channel contribution, measured here by Manders' M1 overlap coefficient, increased significantly by 43% ($F[1.6]=162.5; P<0.0001$) while the M2 coefficient decreased significantly by 36% ($F[1.6]=258.9; P<0.0001$) suggesting greater overlap of the green with the red channel in the ipsilateral hemisphere. Similarly, M1 overlap coefficient increased by 42.6% and M2 coefficient decreased by 31.7% in the contralateral hemispheres. Scale bar, 10 μ m.

..... 110

Figure 27: Repeated sonications improve spatial memory in transgenic and non-transgenic mice:

A. The schematic of the Morris Water Maze setup that was used to behaviorally examine the animals in respect to their spatial memory functionality. The circular maze is considered to consist of four quadrants, the target, the opposite and the adjacent. B. Learning curves of the escape latency and the distance traveled to find the hidden platform are presented herein and plotted against the days of training. Both the distance traveled ($F[4,144] = 15.57$; $P < 0.0001$) and the escape latency ($F[3,36] = 7.542$; $P = 0.0005$) significantly deteriorated for the sham transgenic animals the last day of the training while all other groups continued to improve. C. Representative individual heatmaps of the time spent in every quadrant followed by the cumulative results on the probe trial. The sham transgenic animals did not show preference over any quadrant while the sonicated transgenic animals spent significantly more time in the target quadrant ($F[1.637, 16.37] = 4.051$; $P = 0.044$). Respectively the non-transgenic mice spent more time in the target quadrant with the sonicated group at a much higher percentage (sham non-transgenic: $F[1.965, 17.68] = 6.375$; $P = 0.0085$, sonicated non-transgenic $F[1.776, 15.99] = 16.48$; $P = 0.0002$)..... 128

Figure 28: Repeatability of FUS-induced BBB opening and association with behavioral outcomes in the transgenic animals. The BBB opening volume was measured on the order of $57.5 \pm 8.3 \text{ mm}^3$, $51.4 \pm 12.5 \text{ mm}^3$, $51.00 \pm 9.3 \text{ mm}^3$ and $46.3 \pm 14.2 \text{ mm}^3$ for the four weeks respectively. Statistical analysis revealed comparable opening sizes across weeks. Regression analysis between the cumulative BBB opening volume and the time spent in the target quadrant showed a linear relationship ($r^2 = 0.42$) with a significant deviation of the slope from the zero

value (slope=0.3941; $F[1.9] = 6.43$; $P = 0.0319$). Brain schematics were constructed using Brain Explorer 2 provided by Allen Brain Atlas. 130

Figure 29: Amyloid plaque quantification. A. $A\beta$ immunoreactivity was examined using the $A\beta 42$ specific antibody used in both immunohistochemistry and ELISA while Hoechst 33342 was employed for anatomical navigation. B. Plaque quantification revealed a decrease in the population and volume on the order of 41.14% ($t[7]=1.968$; $P=0.08$) and 28.4% ($t[7]=1.277$; $P=0.24$), respectively, in the sonicated brains. Along the same lines, $A\beta 42$ quantification with sandwich ELISA confirmed the decreasing trend following sonications by 9.33%, yet lacking significance ($t[9]=0.851$; $P=0.41$). Scale bar: 100 μ m. 131

Figure 30: Human total tau quantification. A. Immunohistochemical analysis of the hHT7 antibody detecting human total tau protein revealed a decrease of the neuronal processes affected by tau on the order of 58.31% ($t[6] = 2.802$; $P = 0.0311$). B. Tau removal from the hippocampus shown by immunoblot analysis. Taking the ratio of the HT7 over the GAPDH average intensity-band showed a significant reduction in the brains treated with ultrasound compared to the sham group on the order of 27.33% ($t[9] = 3.771$; $P = 0.004$). Scale bar: 100 μ m. 134

Figure 31: Microglia activation in different sonication regimes. All animals were sacrificed 24 h after the sonication, transcardially perfused and the brains extracted, sectioned and stained with the anti-Iba1 antibody. A. Brains were sonicated at high pressure resulting in large BBB opening volume and pronounced microglia activation shown immunohistochemically. Quantification of

the microglia processes' length and the number of endpoint showed a decrease indicative of activation. B. Sonication within the "safety window" results in microglia activation shown qualitatively and quantitatively. C. Animals were sonicated at 150 kPa without a detectable BBB opening. However, the activation of microglia follows the same trend as in the BBB detectable groups, A and B. D. Sonication in the absence of microbubbles at 1 MPa resulted in the activation of microglia without the occurrence of BBB opening. 142

List of Tables

Table I: Quantification of BBB opening area, fractional anisotropy, and primary eigenvector angular range.....	47
Table II: Summary of the experimental groups and the procedures undergone.	61

Abbreviations

AAV: Adeno-associated viral vector

A β : Amyloid- β

AD: Alzheimer's Disease

ANOVA: Analysis of Variance

ANTS: Advanced Normalization Tools

BBB: Blood-Brain Barrier

CCL: Counter Clockwise

CL: Clockwise

CPu: Caudate-Putamen

CSF: Cerebrospinal Fluid

DA: Dopaminergic

DCE: Dynamic Contrast-Enhanced

DAB: 3,3'-diaminobenzidine

DICOM: Digital Imaging and Communications in Medicine

DTI: Diffusion Tensor Imaging

DWI: Diffusion Weighted Imaging

ELISA: Enzyme-Linked Immunosorbent Assay

FA: Fractional Anisotropy

FUS: Focused Ultrasound

GBCAs: Gadolinium-Based Contrast Agents

GBM: Glioblastoma Multiforme

Gd: Gadolinium

GDNF: Glial-Derived Neurotrophic Factor

GM: Gray Matter

HPLC: High-performance Liquid Chromatography

hp-tau: Hyperphosphorylated tau

MPTP: 1-methyl-4-phenyl-1,2,3,6-tetrahydropyridine

MRI: Magnetic Resonance Imaging

NFT: Neurofibrillary Tangles

NGS: Normal Goat Serum

NHP: Non-Human-Primates

NIFTI: Neuroimaging Informatics Technology Initiative

NTN: Neurturin

PCC: Pearson's Correlation Coefficient

PCD: Passive cavitation detection

PD: Parkinson's Disease

PNP: Peak Negative Pressure

PRF: Pulse Repetition Frequency

p-tau: Phosphorylated tau

PRF: Pulse Repetition Frequency

ROI: Region Of Interest

SEM: Standard Error of the Mean

SN: Substantia Nigra

SNpc: Substantia Nigra pars compacta

SNpr: Substantia Nigra pars reticulata

SVD: Singular Value Decomposition

TBS: Tris-Buffered Saline

TH: Tyrosine Hydroxylase

VBBB: Volume of BBB opening

WM: White Matter

Acknowledgements

The toughest part in compiling more than six years of work in one document is writing this section. Partially because I find it easier to describe research data than my emotions after realizing that one long-lasting chapter of my life comes to a full circle and partially because in the effort to thank everyone who helped along, I recollect memories with people from the distant past like entering a time capsule. Typical signs of emotional writing: the long sentences!

Primarily I would like to thank my advisor Dr. Elisa Konofagou for giving me the opportunity to prove myself a valuable asset in her workforce. I first saw Elisa while in my Master's program at Rutgers University when she gave a seminar on a topic that later on would be the basis of my Dissertation. I followed the trail of her research that led me to her lab where I started as a research associate. I am grateful for gaining her trust that resulted in my transition into a PhD student, a role through which I gained loads of knowledge and experience in medical ultrasound, magnetic resonance imaging and neurodegeneration. Lastly, I feel obliged to thank Elisa for standing by me at a personal level and managing my mother's phone calls and text messages!

I would also like to thank my committee, Dr. Barclay Morrison, Dr. Paul Sajda, and Dr. Sachin Jambawalikar for their scientific guidance and their constructive comments regarding my work. Special thanks to Dr. Karen Duff for her scientific mentorship and agreeing to be a member of my committee despite the location and time-zone constraints.

Furthermore, I would like to specially thank Dr. Serge Przedborski because of his invaluable contribution and knowledge without whom the scientific contribution of Chapter 4 could have

been diminished. On a personal level, he nurtured my understanding in statistics, project design and shaped my problem solving skills. His most memorable quote is: “50% of a publication’s success lies in the design”.

From my UEIL family I would like to specially thank Shutao Wang and Gesthimani Samiotaki who inspired me with their work ethic, guided me in my first years and taught me to own every part of my project no matter the available resources. I would like to also thank all the co-authors, with whom I had the pleasure to work with and especially Matthew Downs, who supported me by sharing his knowledge and giving me the space to grow, Antonios N. Pouliopoulos, who helped me complete Chapter 3.2 that was sitting in my hard drive for some time, Hermes A. S. Kamimura for always being there to assist and share his knowledge and Nancy Kwon for her help and our fiery discussions. Lastly, Tara Kugelman and Maria Murillo who tolerated the vast amount of work of Chapters 4 and 5, respectively, as well as Robin Ji, who stood by me every time I needed his help no matter his workload.

On a personal level I would like to thank my closest friends Grigorios Karageorgos, Iason Apostolakis, Lea Melki, Alexandre Yahi, and Niloufar Saharkhiz as well as Mark Burgess, Julien Grondin, Stephen Lee, Vincent Sayseng, Christian Aurup and Rachel Weber who all made the long days in the lab enjoyable and unique.

Many thanks also go to my UEIL colleagues with whom I shared interesting conversations and great times, Paul Kemper, Alina Shoder, Melina Tourni, Rebecca Noel, Alec Batts, Jad El Harake, Salah Mahmoudi, Judy Li, Ethan Bendau, Murad Hossain, Nirvedh Harshad, Yusuke

Niimi, Yang Han, Tao Sun, Ethan Bunting, Ronny Li, Matthew McGarry, Thomas Payen, Morgan Smith, Alexandre Costet, Hong Chen, Amanda Marie Buch, Cherry Chen, Shih-Ying Wu, Carlos Sierra Sánchez, Pierre Nauleau and Clement Papadacci.

Last but not least I owe my gratitude to Pablo Abreu who would always take the administrative burden that I couldn't hold, stand by me and share memories from back when I was in his interviewing committee while in my first months in the lab!

Additionally, I would like to thank from the bottom of my heart the people who became my family in the US, Anthi Tapiri, Ioanna Tsoulou, Denis Kalogerias, Fani Boukouvala, Natassa Boukouvala and Aris Karakatsanis, that made New York feel like home as well as my closest friends Stella, Stefi and Aggelos who despite the miles that separated us never let the distance discourage them from supporting and standing by my side. You all made this journey smoother and way more fun.

Finally, I would like to thank my family, Velina, Kosta, Dionysia and Ioannis. Emotionally and practically present at all times was my mother Velina, whom I would call while in the shuttle to the lab and she would ask me about the weather! Her most important lesson and constant reminder was that no matter how helpless you feel in the evening having exhausted your efforts, have faith in the rising sun of the coming day. My father Kostas, was most of the times (always actually!) right in his assessment no matter how hard I tried to believe otherwise. His devotion, knowledge and practice of medicine always inspired me to follow his path adjusted to my skills. My aunt, Dionysia, was always a role model for me through her research career. Finally, I would

like to thank Ioannis who shared this entire journey with me through tough and fun times, rough critics and tears, cold winters and humid summers that all made our relationship stronger and him integral part of this experience of mine. This one's for you!

Chapter 1. Background and Motivation

1.1 Central nervous system barriers

The central nervous system (CNS) integrates and coordinates information received from all parts of the body through its main structures, the brain and the spinal cord. The architectural characteristics of the CNS microvessels are uniquely suited to preserve ionic homeostasis¹ by formation of brain-barrier interfaces that restrain diffusion². Molecular exchange between the blood and the brain (interstitial fluid and cerebrospinal fluid (CSF)) is regulated through tight junctions³ by i. the blood-brain barrier in the neurovascular unit (Figure 1a), ii. the blood-CSF barrier at the choroid plexus (Figure 1b), iii. the arachnoid barrier between the subarachnoid space and the dura in the middle of the meninges (Figure 1c) and iv. the PIA/glia limitans barrier between the CSF and the extracellular fluid of the brain (Figure 1c). Of the various CNS barriers, the toughest compartmental control over the immediate microenvironment is exerted by the blood-brain barrier (BBB)²⁻⁴.

1.2 The blood-brain barrier

The anatomical substrate of the BBB, the cerebral vascular endothelium, along with pericytes, microglia, astrocytes and neurons constitute the neurovascular unit that encompasses a wide range of morphological characteristics and functional features. Cerebral endothelial cells lining the brain vessels circumferentially restrict diffusion by complex tight junctions, forcing molecular trafficking to take a transcellular route rather than paracellular²⁻⁵ (Figure 2). The tight junctions are intricate transmembrane and cytoplasmic proteins⁶ whose tightness is reflecting the permeability of the BBB. BBB permeation can occur through lipid membranes for small lipophilic molecules such as O₂ and CO₂, specific transport systems for nutrients among other

hydrophilic agents or metabolic transport by a combination of intracellular and extracellular enzymes⁷.

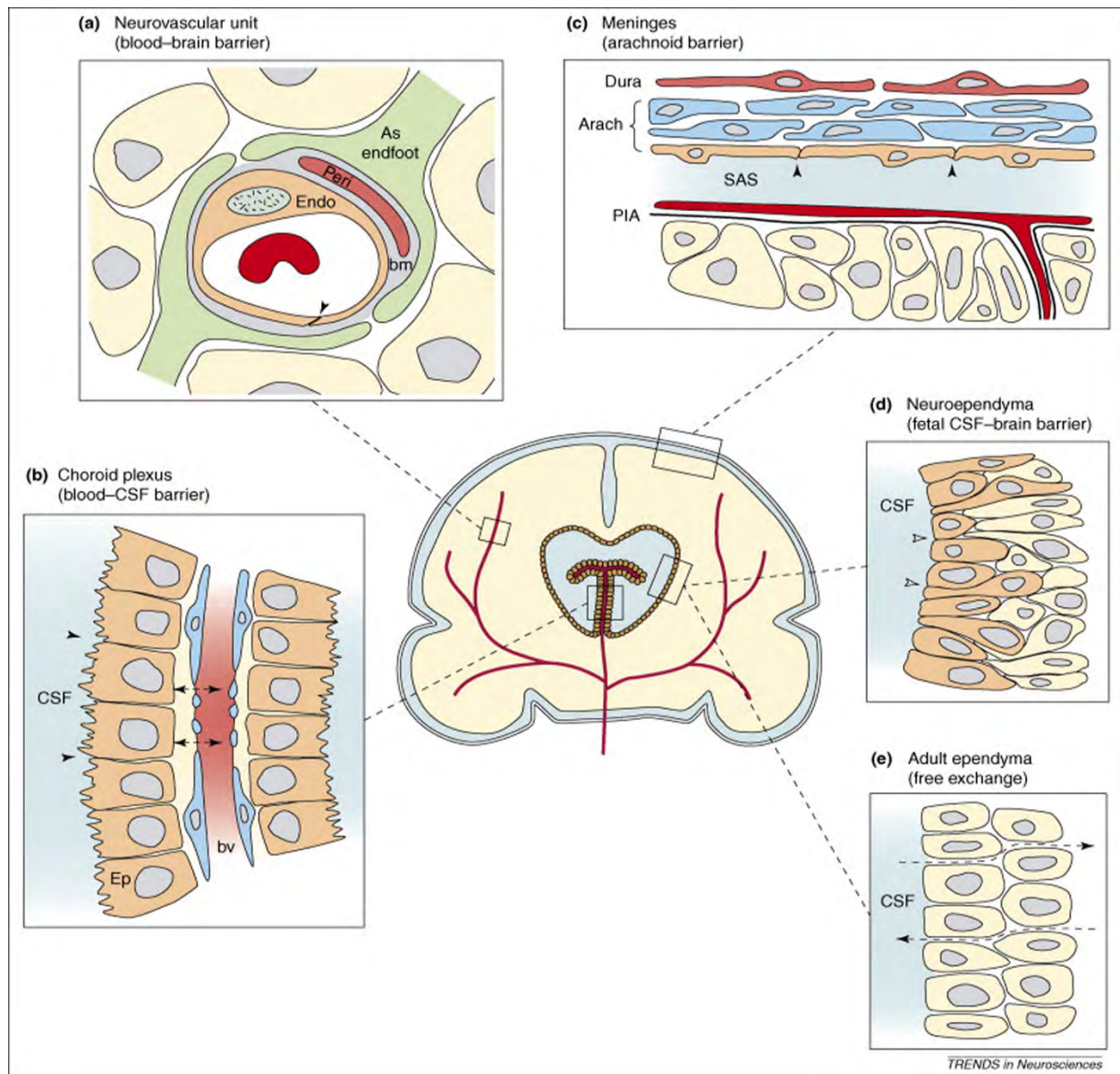


Figure 1: The central nervous system barriers. a. The blood-brain barrier between the brain parenchyma and the blood lumen. b. The blood-CSF barrier at the Choroid plexus. c. The meningeal barriers consisted of the arachnoid barrier between the CSF in the subarachnoid space and the overlying structures, as well as the PIA/glia limitans barrier and the brain parenchyma. d. The CSF-brain barrier is important only in the embryo while it is governed by free exchange in the adult brain⁴.

Large hydrophilic compounds necessitate receptor-mediated transcytosis. Attached to the abluminal part of the endothelium are the pericytes, cells necessary for the functionally effective BBB formation. Moreover, pericytes regulate tight junctions, vesicle transportation and the BBB permeability by inhibition of adhesion molecules increasing vascular permeability. The basal lamina of the endothelial cells is ensheathed by the astrocytic end feet that mediate the induction of phenotypic BBB features^{6,7}. Although astrocytes vary morphologically in regards to their location and cell association, 72% of the population interacts with the BBB features resulting in the tightening of the junctions, expression and localization of enzymes and transporters^{6,7}. Neurons innervate the vascular endothelium or the astrocytic processes or can be found in their near proximity, no further than 10 μm ⁷. Neuronal activity and the associated metabolic needs are met by the highly responsive microcirculation⁶. Finally, microglia are innate immune cells highly responsive to the blood-brain barrier by surveillance of their microenvironment. BBB dysfunction or infiltration of infectious agents in the brain parenchyma can morphologically alter their phenotype and properties. Synergistic functions involving more than one of the aforementioned cell types are a highly plausible scenario given the complexity of the barrier properties⁶.

The transport mechanisms discussed allow the BBB to control the efflux and supply of the brain with nutrients by restricting ionic and fluid exchange between the two compartments involved, providing ideal conditions for neuronal function. Furthermore, the BBB protects the brain from ionic fluctuations while preserving the separation of peripherally and centrally derived neurotransmitters or neuroactive material. Homeostatic stability can be disturbed though, in the

event of a dysfunctional barrier³. Oxidative stress, inflammatory mediators, malfunction of the

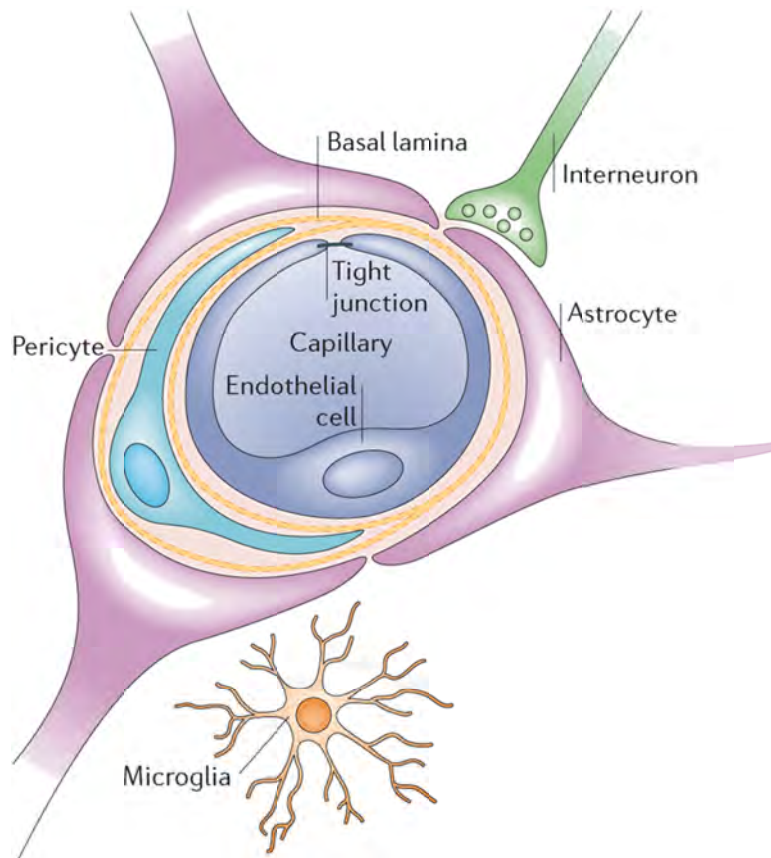


Figure 2: The neurovascular unit. The capillary is surrounded by an endothelial cell, with its two ends connected by a tight junction, and ensheathed by astrocytic processes. The pericytes are located in the basal lamina space while the microglia in the interstitial fluid of the extracellular compartment⁷.

transport mechanisms and abnormal angiogenesis constitute some of the factors initiating complex functional changes in the BBB⁴. Increased BBB permeability is critical for the expression or progression of neurological disorders. Leakage could be consequential to the disease (traumatic brain injury, ischemic stroke) whereas in some cases it is a precipitating event (multiple sclerosis)⁶.

In neurodegenerative diseases such as those studied here, Parkinson's and Alzheimer's disease, cerebrovascular abnormality and BBB breakdown are not fully understood⁶.

1.3 Neurodegenerative disorders

In spite of the broad use of the term “neurodegeneration”, the precise definition is yet an arduous effort⁸. In practice, neurodegeneration encompasses disorders related to the impairment of neurons in specific functional anatomic systems among which, Parkinson’s (PD) and Alzheimer’s disease (AD) belong to the lion’s share of attention along with amyotrophic lateral sclerosis and Huntington disease. Despite the complexity, classification of the neurological disorders can be performed based on the predominant clinical feature or the topography. Here, we focus on the two major age-related and chronically progressive neurodegenerative disorders affecting different neuronal networks, Alzheimer’s and Parkinson’s disease.

1.3.1 Alzheimer’s disease

Alzheimer’s disease is the most common age-related and chronic neurodegenerative disorder characterized histopathologically by the accumulation of insoluble forms of amyloid- β (A β) in plaques and the aggregation of hyperphosphorylated forms of the microtubule-associated protein-tau into neurofibrillary tangles (NFT) in neurons^{9,10} (Figure 3). Extensive research reports that these two hallmark lesions, and the accumulation of toxic intermediates from which they are formed, are implicated in the initiation and progression of dementia. The amyloid cascade hypothesis¹¹ suggests that A β promotes tauopathy which has been demonstrated in numerous experiments. The pathological cascade of events that leads to tauopathy and neurodegeneration includes tau hyperphosphorylation, misfolding and aggregation, destabilization of the microtubule network and the cytoskeleton, deficits in axonal transport, synaptic loss, neurodegeneration and cell death. Tauopathy has been shown to propagate

between brain regions, and it can undergo trans-cellular transfer either from the somatodendritic compartment or at the axon terminals across

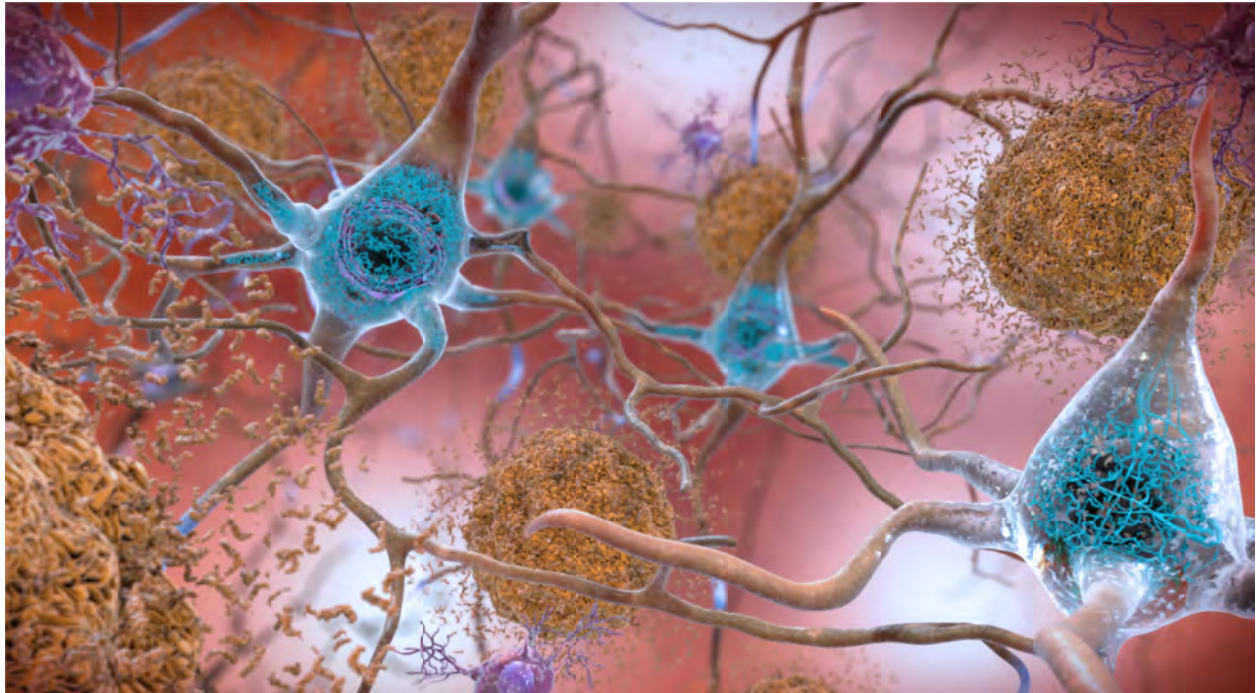


Figure 3: Alzheimer's pathology is characterized by the accumulation of amyloid- β in plaques (brown) in the brain parenchyma and intraneuronal aggregation of hyperphosphorylated tau into neurofibrillary tangles (blue). Image courtesy of the National Institute on Aging/National Institutes of Health.

the synapses. The mechanism of transfer is not known but it is likely vesicle-mediated or via the release and uptake of conformers that act as prion-like seeds^{12,13}. Biomarker association with disease progression shows tau accumulates at the earliest stages of dementia, and the density and distribution of hyperphosphorylated tau (hp-tau) has been linked to cognitive decline^{12,14–16} making tau an attractive therapeutic target¹⁷.

1.3.2 Parkinson's disease

Parkinson's disease is close enough to Alzheimer's disease in prevalence and its pathological characteristic is the progressively degenerating dopaminergic pathway¹⁸. Dopaminergic neurons

form the nigrostriatal pathway (Figure 4), whereas loss of neurons in the Substantia Nigra pars compacta (SNpc) results in striatal dopamine deficiency¹⁹. In advanced stages of PD, non-motor symptoms become a significant part of the disease, including cognitive impairment, psychiatric and autonomic dysfunction that can often become more troublesome than the cardinal motor manifestations of PD²⁰. These disabling non-motor manifestations have been attributed to the degeneration of non-dopaminergic pathways that arises over the course of the disease²¹ and which are typically not responsive to either dopaminergic therapies (e.g. L-DOPA administration) or deep brain stimulation. Conversely, in early stage PD, patients are highly responsive to dopaminergic stimulation²¹. This is particularly important as patients with early PD are physically and professionally active²² and most are reticent to use L-DOPA because of its known side effects. From a clinical standpoint, the cornerstone in prevention and management of the disease is the deceleration of the progression through non-pharmacological approaches - behavioral techniques and adjusted nutrition- and pharmacological agents targeting cognition enhancement and systemic complications management. Despite the importance of symptomatic amelioration, the development of a disease-modifying drug remains a priority.

1.4 Focused ultrasound

Treatment of the CNS diseases involves the engagement of the blood-brain-barrier to transport therapeutic agents to impaired brain structures. The BBB hinders the transcellular diffusion path, which is confined only to lipid soluble compounds smaller than 400 Da with fewer than nine hydrogen bonds crossing via lipid-mediated transport. To overcome this obstacle, current treatment strategies involve transcranial injection or infusion, trans-nasal delivery or employment of medicinal chemistry to chemically alter the nature of the compound so it can

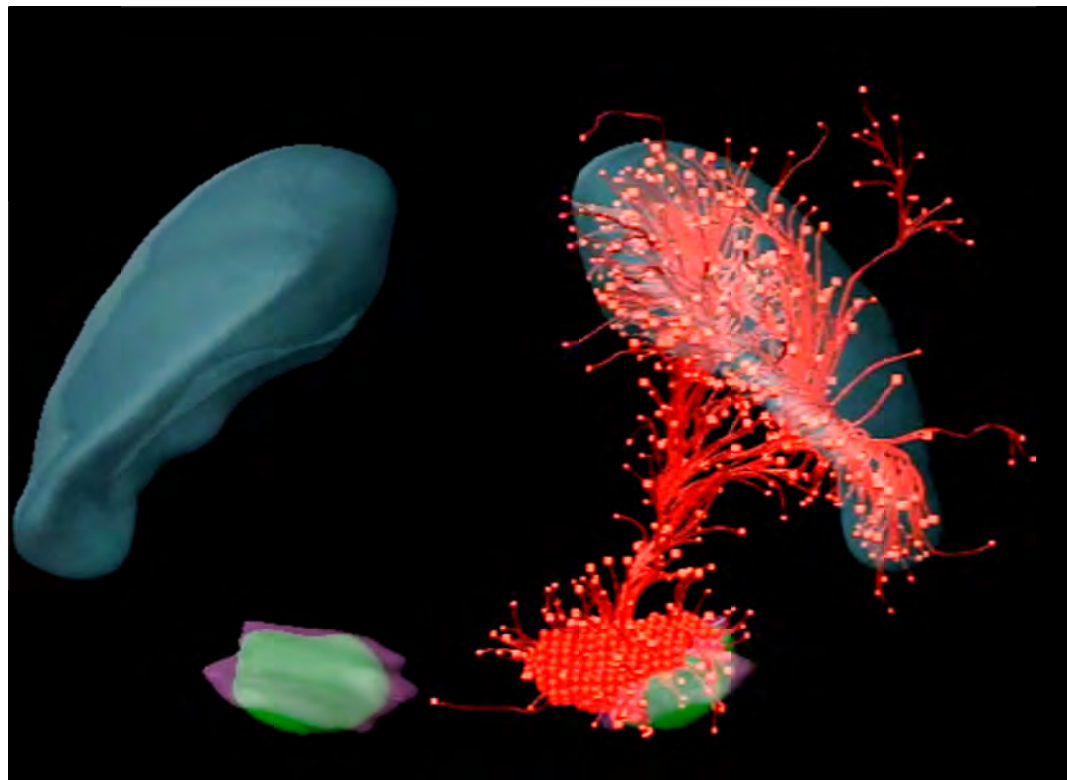


Figure 4: The nigrostriatal pathway describes the dopaminergic neuron (orange) and the structures involved. The neuronal cells lie in the substantia nigra pars compacta region (SNpc in green) with their axons innervating the striatum (blue). Figure generated utilizing the Allen Institute library.

through carrier-mediated, receptor-mediated or active efflux transport²³. However, all of these methods are either invasive, non-targeted and/or involve alteration of the drug composition. Direct injection, convection enhanced delivery and osmotic BBB disruption are some examples of targeted but invasive techniques while biological and chemical approaches as well as intranasal drug delivery are non-invasive but not targeted methods as well^{24,25}. The employment of focused ultrasound (FUS) coupled with microbubble administration has been proposed as the only noninvasive technique to transiently, locally and reversibly disrupt the BBB allowing a time and size window for molecules to cross to the brain parenchyma^{26,27}.

The microbubbles are perfluorocarbon-filled, lipid-coated microspheres on the order of a few microns in diameter, characterized by slow solubility and dissolution kinetics, attributed to their shell composition²⁸. The lipids form spontaneously a monolayer coating, with their hydrophobic tails facing the gas core, when their aqueous suspension is dispersed with perfluorocarbon and acoustically emulsified²⁹. Their stability in the blood vessels has been improved by increasing the hydrocarbon chain-length of the coat-constituent lipids improving their physicochemical properties and their overall efficiency^{28–31}.

The acoustic transducer is a piezoelectric element generating an acoustic pressure wave when electric energy drives it. Ultrasonic energy focused at the geometrical center can be tightly deposited deeply within the brain tissue while minimizing skull energy absorption. During focused ultrasound application the transmitted acoustic pulse generates a radiation force that drives the expansion and contraction (or collapse) of the microbubbles following the respective periodic cycles of rarefaction and compression³⁰. Acoustic cavitation describes the volumetric oscillations of the microbubbles that in turn deform the compliant boundary of the nearby vessel walls. Controlled oscillation of the microbubbles, stable cavitation, results in increased vascular permeability, while rapture of the bubbles, inertial cavitation³², has been associated with increased risk for damaging the surrounding microenvironment^{32,33}.

Hence the size-dependent resonance behavior of the microbubbles, their response to the acoustic field varies according primarily to the center frequency, the applied pressure and the pulse length²⁸. To compromise the tradeoff between irreversible cavitational effects at low frequencies and strong attenuation effects at high frequencies, the optimal frequency for transcranial

applications has been placed in the range of 0.2-1.5 MHz³⁴⁻³⁶. The relatively low frequencies combined with various pressures have been shown to successfully induce BBB openings of different sizes depending on the weight of the deliverable agent³⁵. Moreover, pairing lower pressures with longer pulse lengths has been found to induce similar opening sizes to higher pressures with shorter pulse lengths³⁷. The effect of the ultrasound parameters on the vascular permeability is linearly dependent on the microbubble concentration while the functional outcomes are more predictable for narrower size-distributions of microbubbles³⁴.

The closing timeline and the reversibility of the BBB opening have been extensively investigated to assess the safety profile of the intervention. The time necessary for the barrier to be fully restored has been found proportionally related to the opening volume assuming the induction of a single opening³⁸. Decoupling of this dependence has been achieved by substituting large openings with small multi-foci openings decreasing the necessary time for the barrier to be restored^{39,40}. Longitudinal studies on rodents and primates have shown that repeated ultrasound-induced BBB opening in the absence of vascular damage is a transient and reversible application^{41,42}.

Passive cavitation detection (PCD) captures the acoustic emissions from the oscillating microbubbles providing information regarding the cavitation signature⁴³. Accurate expectation of the induced BBB opening volume has been achieved through its association with the corresponding cavitation levels⁴³. Passive cavitation mapping expanded the single dimension of the PCD into spatial localization of the acoustic sources enabling the real time monitoring of the ultrasound therapy^{44,45}.

Although passive cavitation detection is a promising modality in spatially associating microbubble oscillations with BBB opening^{44,45}, the gold standard in confirming the occurrence of an opening, validating the accuracy of the targeting and assessing the barrier's restoration *in vivo* is contrast-enhanced T1-weighted magnetic resonance imaging (MRI)^{26,46}. T1-weighted imaging after the injection of contrast agents incapable of naturally crossing the BBB are employed as tracers to spatially localize the disruption site. Contrast agents are useful in the quantification of the BBB opening volume based on their diffusion area while their permeability changes over time provide information for mapping their transfer rate^{47,48}. T2-weighted imaging and susceptibility weighted imaging (SWI) have been extensively employed to assess potential edematous or inflammatory regions and hemorrhagic, respectively, following FUS application⁴¹.

Restoration of the barrier has not been only macroscopically evaluated by MRI but also neurologically by visual, cognitive, motivational and motor function behavioral testing^{41,42}. Although the interaction of systemically-administered microbubbles with the capillary walls has been proposed to drive the disruption of the BBB with FUS, the mechanism is not entirely clear as not fully understood are the downstream bioeffects. Disassembling of the tight junctional (TJs) molecular structure has been placed at the beginning of the induced biological cascade, explaining the paracellular passage of molecules that has been reported^{49,50}. Moreover, transcriptomic analysis in the acute stages following sonication revealed a transient upregulation in proinflammatory cytokines and chemokines including CCL2, CCL3, and Tnf that have been found to promote migration, proliferation, differentiation and survival of neural progenitor cells favoring neurogenesis⁵¹. Prominent presence of BrdU-positive cells in animals that survived for

a week after the last of six sonications has been linked to enhanced neurogenesis attributed to the expression of trophic factors such as brain-derived neurotrophic factor in the targeted brain⁵². Concurrent with the overexpression of inflammatory markers that mostly resolved within 24 hours, was the increase in angiogenetic-related genes and astrocytic activation⁵¹.

Despite the positive impact of the technique, reports on elevated microtubule-associated protein tau, phosphorylated at the Thr231 epitope⁵², and activated Nf- κ B pathway⁵³ following repeated sonications, alarmed the ultrasound field and surfaced important unmet needs. Although the uncontrolled phosphorylation of tau protein has been linked to Alzheimer's disease, phosphorylation has to occur at specific epitopes and proven to lead to pathological outcomes⁵⁴. Tau phosphorylation at the Thr231 epitope is associated with both physiological and pathological processes⁵⁴ and further experimentation is required to assess association with Alzheimer's disease as the upregulation alone does not suffice. Regarding the initiation of the Nf- κ B pathway, several reports argue on whether it is a byproduct of the sonication regime⁵³ or it is completely dissociated from the intervention⁵¹. Contradictory findings and ambiguous interpretations signify the need to fully characterize the biological changes specific to the selected sonication protocol.

So far, FUS has been studied extensively in a multitude of experiments involving the safe disruption of the BBB of various animal species (including rabbits^{55,56} mice⁵⁷, rats⁵⁸ and primates^{59,60}) and in different animal models^{61–67}. The integrity of the BBB is restored within hours and it remains intact⁶⁸ depending on the ultrasound parameters, regardless of the pathological state of the brain at least for early stages⁶⁹. FUS mediated BBB opening has been

proven indifferent in terms of energy requirements to achieve permeability and closing timeline between transgenic and wild type mice⁶⁹.

This intervention has shown efficacy in delivering various compounds of different molecular weights into the brain parenchyma including contrast agents³⁷, sugars⁷⁰, antibodies⁷¹, chemotherapeutics⁷² and neurotrophic factors^{66,67,70,73–76}. FUS-induced BBB opening was initially introduced as a surrogate to drug delivery techniques. It prevailed due to its non-invasive and targeted principles.

Aside from facilitating drug delivery, FUS-induced BBB opening has been introduced as an immunomodulatory stimulant associated with microglia activation⁵³ following a unique cascade that strongly depends on the ultrasound parameters (Figure 5). More importantly, it has been observed that FUS-induced BBB opening over the entire brain activated microglia leading to the 52% reduction of amyloid burden⁶². This important finding highlights the potential of inducing a beneficial immune response by ultrasound, using a safely tolerated paradigm^{61,62}. Such observations re-introduced the FUS-induced BBB opening as an immunomodulatory stimulant.

Microglia are self-proliferating resident cells, well integrated in the neurovascular unit in the healthy brain⁷⁷. Preservation of homeostasis is performed during their “resting state” by a scavenging function of the immediate neighborhood with the cell somas remain relatively stable while the processes undergo dynamic elongation and retraction to monitor the environment (Figure 5). Upon detection of a pathogen or alteration of the homeostatic status, microglia respond immediately to the stimulus by altering morphologically from a ramified “resting” to an

active state through retraction of their processes accompanied by the secretion of effector

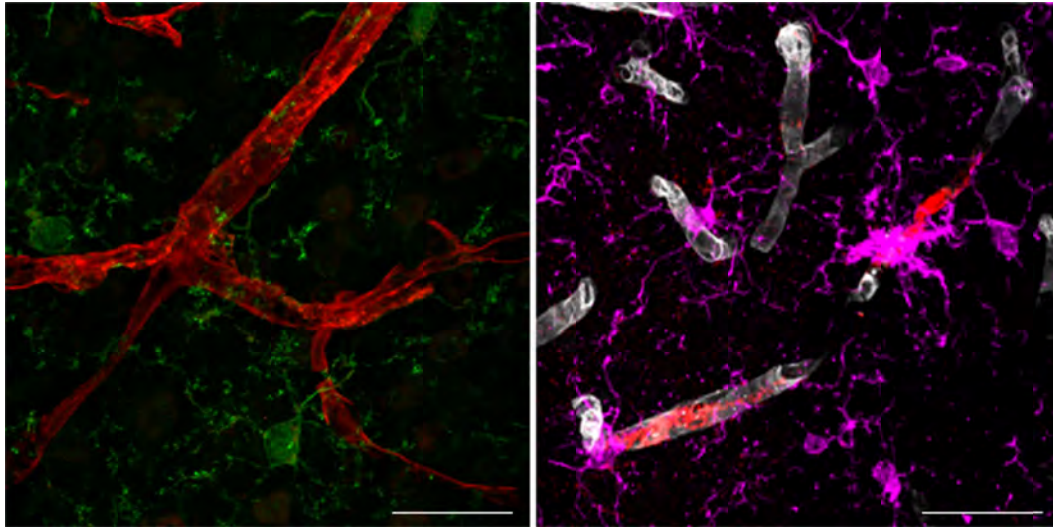


Figure 5: Left: Representative confocal image revealing close interaction between microglia (Iba1, green) and endothelial cells (IsolectinB4, red)⁷⁸. Right: Representative confocal image showing the proximity of the microglia (Iba1, purple) to the area of biocytin-TMR leakage (red) from the vessels (Glut1, white) following FUS-induced BBB opening (T. Kugelman et al. *submitted*).

molecules for further recruitment⁷⁷. A plethora of immune receptors could trigger microglia activation such as scavenger, cytokine and chemokine receptors⁷⁷. Although microglial activation was considered detrimental in the past, researchers have revealed the beneficial impact of alternative microglial activation⁷⁹.

The role of microglia in neurodegenerative diseases remains a controversial topic. Although microglia respond immediately to acute injury, morphologically activated microglia for an extended period of time fail to synthesize inflammatory mediators assaulting neuronal integrity. Prolonged activation of microglia is present in chronic neurodegenerative disorders such as Alzheimer's and Parkinson's disease, yet efforts to inhibit inflammatory mediators secreted from

microglia failed to ameliorate the degeneration⁸⁰ (Figure 6). These findings indicated a gap in

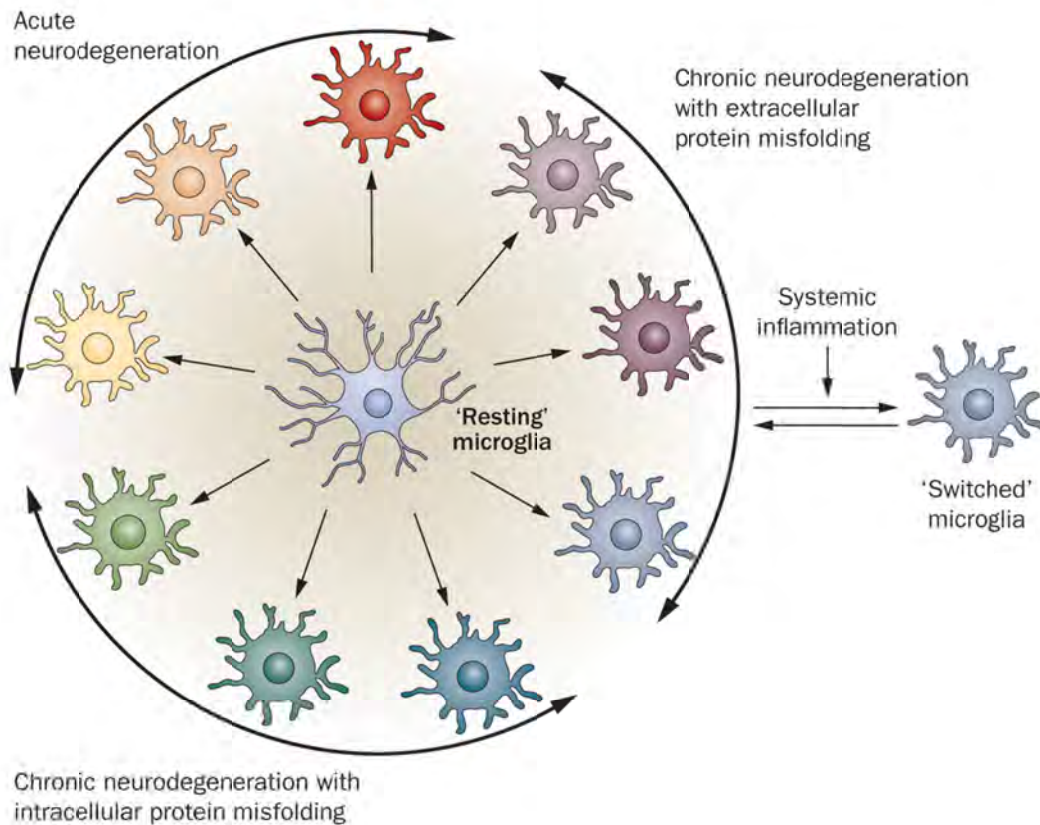


Figure 6: Microglia phenotypes during the phases of neurodegeneration⁸⁰.

understanding the molecular mechanisms connecting the inflammatory response to the progressive degeneration. In Alzheimer's disease, microglia acquire an "activated" phenotype with extended processes into the plaque core yet fail to reduce amyloidosis⁸¹ while considered mediators of tau spreading¹⁶. The link between microgliosis and tau pathology remains controversial^{79,82}. Stimulus-dependent conformational changes and dystrophy have been associated with tau pathology while re-programming of the microglia to healthier phenotypes has recently emerged as a therapeutic strategy^{83,84}. Similarly, phenotypic microglia activation leads to the loss of dopaminergic function in Parkinson's disease⁸⁵ while increased levels of anti-inflammatory agents resulted in protection from neurotoxicity. These findings suggest that

modulation of microglia and monocytes' recruitment can have a profound beneficial effect in ameliorating neurodegeneration while pointing towards the notion that the inflammatory environment impacts negatively the microglia to engage in their phagocytic role⁸¹. There is an immense potential in studying microglia functionality beyond their phenotypic changes⁸⁰. Whether FUS-induced BBB opening drives a “healthy” activation of microglia, or infiltrating blood-derived macrophages⁸² help ameliorate such pathologies remains unclear but these mechanisms could explain the positive effects established in the literature and herein.

Chapter 2: Specific Aims

This Dissertation entails three specific aims that rise from uncharted questions in the ultrasound field that were deemed critical to investigate. Despite the extensive experimentation on the optimization of the ultrasonic energy deposition, hardware- and parametric-wise (Figure 7), the correlation of the BBB opening volume with the sonication incidence angle remained an open question. The first part of specific aim one is dedicated in answering the aforementioned relationship considering the contribution of the skull thickness and the brain anatomy in the BBB volume variance (Figure 8).

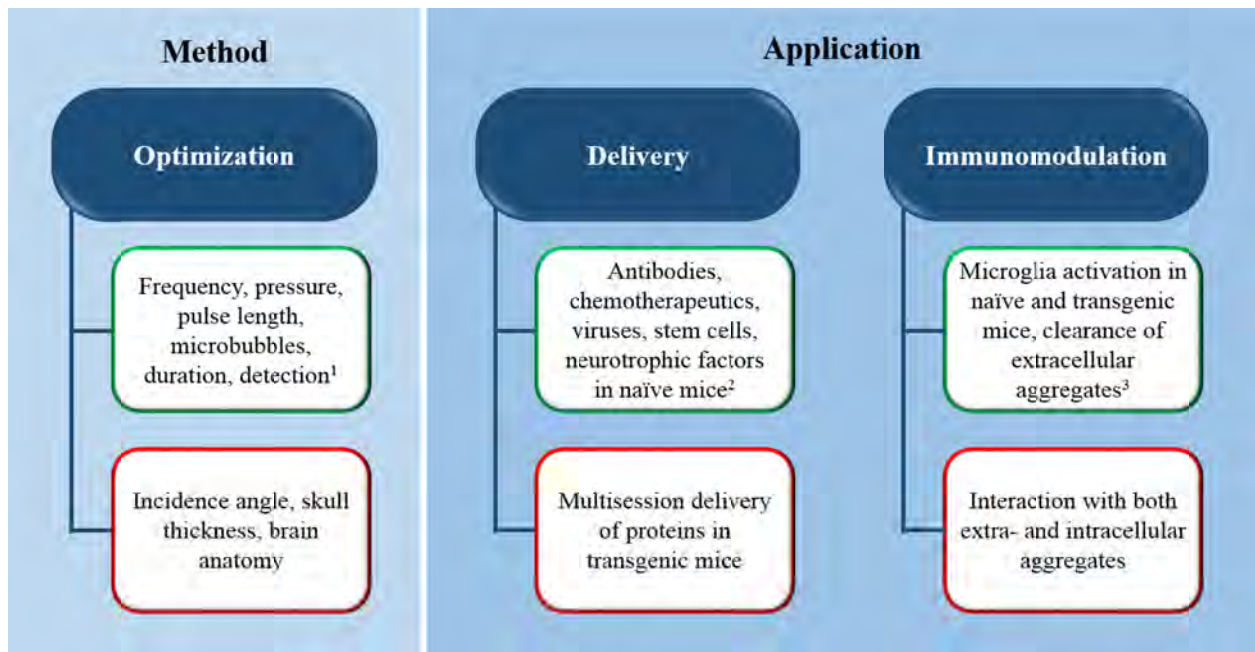


Figure 7: Overview of the research conducted in the field of sonication optimization and application.

Furthermore, optimization of the method design does not only refer to the induction of the BBB opening but also the detection. The second part of specific aim one entails the implementation of a contrast-free magnetic resonance sequence followed by rigorous analysis achieving BBB detection in the absence of Gadolinium (Gd).

Specific aims two and three belong to the application domain of FUS-induced BBB opening. Specific aim two constitutes a multisession protein (neurotrophic factor) delivery study in a PD mouse model resulting in neuronal upregulation (Figure 8).

The third specific aim investigates the immunomodulatory effects of FUS-induced BBB opening in transgenic mouse models that suffer from intracellular pathological aggregates, first part, or both intracellular and extracellular aggregates, second part (Figure 8).

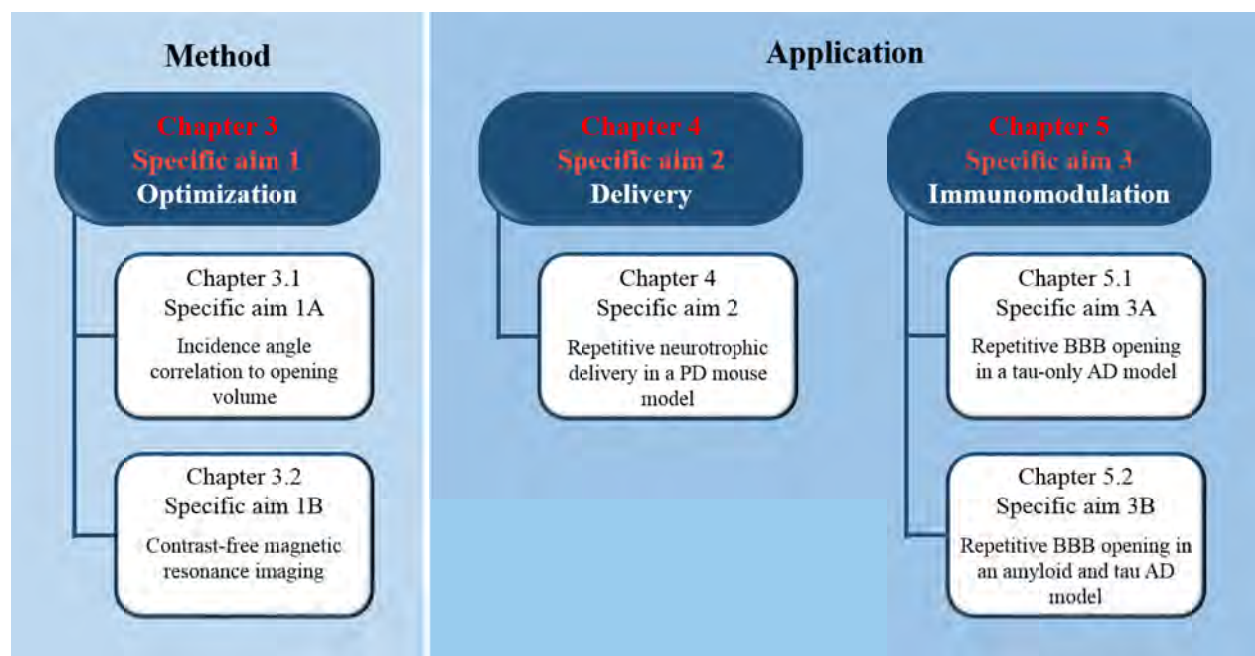


Figure 8: Overview of the specific aims in terms of the optimization and application fields.

Chapter 3: Optimization of the focused ultrasound targeting and the blood-brain barrier opening detection.

In this chapter, a thorough optimization maximizing the targeting efficiency in sonications employing single element transducers will be described followed by the exploration of contrast-free MRI to overcome the deleterious effects of Gd retention in the brain tissue.

3.1 Targeting effects on the volume of the focused ultrasound-induced blood-brain barrier opening in non-human primates in vivo.

3.1.1 Abstract

Drug delivery to subcortical regions is susceptible to the BBB impeding the molecular exchange between the blood stream and the brain parenchyma. Focused ultrasound coupled with the administration of microbubbles has been proven to open the BBB locally, transiently and non-invasively both in rodents and in Non-Human-Primates (NHPs). The development of this disruption technique independent of MRI monitoring is of primordial importance yet restrained to the targeting optimization. The current paper establishes the linear relationship of the incidence angle with the volume of BBB opening (V_{BBB}) and the Peak Negative Pressure (PNP) when sonicating the Caudate Nucleus and the Putamen region of five non-human-primates. In addition, the effect of central nervous system structures on the opening morphology is evaluated by identification of the gray-to-white-matter ratio at the opening site. Finally, the targeting accuracy is assessed through estimation of the geometric and angle shift of the opening from the targeted region. Interestingly, results prove a monotonic increase of the opening volume with close to normal incidence angles. Moreover, 80.35% of the opening lies on gray matter regions compared to only 19.41% attributed to the white matter. The opening was found to be shifted

axially, towards the transducer, and laterally with an average angle shift of 4.5°. Finally, we were capable of showing reproducibility of targeting accuracy with the same stereotactic and ultrasonic parameters. This study documents the a priori prediction of the opening volume through manipulation of the angle and pressure as well as establishing the predictability, accuracy and safety of FUS induced BBB opening in NHPs.

3.1.2 Introduction

The mechanism of BBB disruption with FUS is not entirely clear, however, it has been proven that the BBB can be mechanically disrupted by cavitation occurring from the oscillating microbubbles that pass through the focus of the ultrasound beam^{27,69,86}. Extensive research has been conducted to evaluate the microbubble properties affecting the BBB in the presence of ultrasound. The BBB opening volume has been shown to increase with concentration and microbubble size while small increases in the microbubble phospholipid chain length resulted in more efficient delivery of large molecules^{31,87,88}.

The transition from bench to bedside requires precise selection of parameters that would guarantee targeting accuracy, repeatability and safety. Several studies have been focused on the optimization of the acoustic parameters on various animal models including, mouse, rabbit and non-human primate aiming at safe and localized openings^{43,89–95}. While traversing from mouse to NHP, the parameters to be determined in terms of brain complexity and experimental setup increase. Furthermore, the targeting accuracy in NHPs is susceptible to skull aberrations. When sonicating NHPs, the preference of intermediate ultrasound frequencies around 500 kHz eliminates the tradeoff between irreversible cavitational effects and increased focus at lower

frequencies and high phase aberrations and attenuation at higher frequencies^{43,96–98}. Yet the frequency is not the only factor that could result in vascular damage as PNP is of equal contribution and importance. It has been reported that increased PNP yield larger openings in a linear trend while shorter pulse lengths and intermediate pulse repetition frequencies (PRFs) are preferred^{33,94,96,99}. However, PNP to opening volume correlations in NHP's yielded very low determination coefficients while the cross correlation among animals was inconclusive^{33,97,98,100,101}. It has been shown that the normal incidence angle yields larger openings but its relationship with the opening size and the PNP is yet to be established¹⁰². The necessity to alter the angle rose from the complexity of the NHP brain and the aim to avoid affecting neighboring areas and vascularized regions. Despite taking into account the angle, however, agreement across animals remains elusive. Therefore, the skull effect was investigated as of affecting the energy propagating to the targeted region. According to the incidence angle of preference, the beam propagates through a varying skull volume resulting in subsequent pressure alterations^{102–104}. Moreover, inter-animal skull variation adds to the complexity of the problem. The targeting accuracy subjected to the variation of these parameters has to be optimized before moving on to clinical trials.

In this study, we seek to provide insight into the uncorrelated results within and among animals by: (i) establishing the relationship between the incidence angle and the BBB opening volume, (ii) employing the skull effect as the correction factor among animals and (iii) evaluating the brain structures' effect on the opening morphology. The skull effect was evaluated at different incidence angles and was utilized as the correction factor to the results while the percent of gray and white matter regions overlapping with the BBB opening region was evaluated.

3.1.3 Materials and Methods

***In vivo* experiments**

The ultrasound procedure was performed in five male NHPs, i.e. four rhesus macaques (*Macaca mulatta*) and one marmoset (*Callithrix jacchus*) allowing for a minimum of two-week resting period before subsequent treatment. During each procedure, the animals were immobilized by intramuscular administration of a cocktail containing 1ml ketamine (5-15 mg/kg) and 1ml atropine (5-15 mg/kg) to provide a time window for endotracheal tube placement, catheterization and positioning on the stereotaxic frame. While in the operation room, the animals were anesthetized by inhalation of 1–3% isoflurane. The transducer was attached to the Kopf stereotaxic manipulator to allow for targeting the brain in the stereotaxic coordinate frame, the cornerstone of the targeting analysis. The animals were transferred to the MRI site after the sonication for assessing the safety of the method and verifying the BBB disruption.

Focused ultrasound

The sonications were carried out by a single-element, spherical-segment FUS transducer (H-107, Sonic Concepts, Bothell, WA) operating at 0.5 MHz (radius: 32 mm; geometric focal length: 62.6 mm, focal length: 34 mm and focal width: 5.85 mm), under the application of a function generator (Agilent, Palo Alto, CA, USA) through a 50-dB power amplifier (E&I, Rochester, NY, USA). A flatband, spherically focused hydrophone (Y107, Sonic Concepts, WA, USA; sensitivity: 10 kHz to 15 MHz; focal depth: 60 mm, radius 19.75 mm) was confocally mounted at the central void of the transducer to achieve overlap of the two foci. The hydrophone was driven by a pulser–receiver (Olympus, Waltham, MA, USA) connected to a digitizer (Gage

Applied Technologies, Lachine, QC, Canada). The acoustic beam profile and the -6 dB focal zone were measured during the calibration process accomplished by the use of a needle hydrophone (HGL-0400, Onda, Sunnyvale, CA, USA). According to previous reports^{100–104}, the global attenuation due to absorption, reflection and scattering phenomena resulting from the skull thickness was estimated to be equal to 4.92 dB/mm at the center frequency. In-house manufactured, lipid-shell, monodisperse microbubbles with a mean diameter of 4 to 5 μm were diluted to 2×10^5 # bubbles/mL. The microbubbles at a dosage of 2.5×10^8 # bubbles/kg were intravenously injected through the saphenous vein 10 sec after the onset of sonication to allow for real-time monitoring of the microbubble cavitation described elsewhere²⁹. The animals were sonicated in one or two locations for 120 sec each, allowing a 20-minute waiting period for microbubbles to be cleared from the circulation, at a pulse repetition frequency (PRF) of 2 Hz, pulse length of 10 ms and PNP varying from 0.25 MPa to 0.6 MPa.

Targeting

Individualized targeting of the ultrasound focus to the brain region of interest was accomplished by employment of a Kopf stereotaxic instrument. The system provided the user with 9 degrees of freedom; the medio-lateral drive (ML), the stereotaxic arm along the anterior-posterior (AP) direction oriented perpendicularly to the ML drive, the manipulator determining the dorso-ventral (DV) setting oriented perpendicularly to the ML-AP plane, the rotation of the manipulator around the DV-axis (azimuth), the rotation of the manipulator around the ML- or AP- axis (elevation), the selection of right or left stereotactic arm (arm), the relative alignment of the ML- and DV- drives (stereo) and finally the attachment of the transducer to the stereotactic manipulator (finger). In order to predict and evaluate the targeting accuracy, the geometric

characteristics of the stereotactic device were analytically implemented into a custom algorithm in MATLAB based on the relative positioning of the nine aforementioned parameters in terms of the stereotaxic coordinate frames. This routine yielded the coordinates of the focal spot and the surrounding ellipsoidal area denoting the focal region in the global coordinate system translated into spatial domain by superposition onto the stereotactically aligned T1-weighted scan accounting for the reference scan for each NHP.

Opening verification with MRI

Magnetic resonance imaging was employed to verify the opening and detect potential damage. High-resolution structural T1-weighted sequences (T1 Pre; 3D Spoiled Gradient-Echo, TR/TE = 20/1.4 ms/ms; flip angle: 30°; NEX = 2; spatial resolution: $500 \times 500 \mu\text{m}^2$; slice thickness: 1 mm with no interslice gap) were acquired at two time-points for each NHP, before and after BBB opening. The first scan was acquired 30 minutes after IV administration of 0.2 ml/kg Gd (gadodiamide), as the contrast agent, without preceding sonication accounting as the pre-sonication scan for each NHP while the second scan was acquired after each sonication corresponding to the post-sonication scan. Gd does not naturally cross the intact BBB because of its molecular size exceeding the threshold (400 Da) and solubility pattern and therefore was utilized as a means of visualizing vessels or structures with increased BBB permeability attributed to hyperintense pixelation. Prior to the sonications, a structural T1-weighted sequence of the same acquisition parameters but spatial resolution of $250 \times 250 \mu\text{m}^2$ was obtained while the animal was positioned on the stereotactic frame accounting for the reference image. 3D T2-weighted sequence (TR/ TE = 3000/80 ms/ms; flip angle: 90°; NEX = 3; spatial resolution: $400 \times 400 \mu\text{m}^2$; slice thickness: 2 mm with no interslice gap) and 3D Susceptibility-weighted

imaging (SWI) (TR/TE = 19/27 ms/ms; flip angle: 15°; NEX = 1; spatial resolution: $400 \times 400 \mu\text{m}^2$; slice thickness: 1 mm with no interslice gap) were utilized to detect edematous and hemorrhagic regions if any^{60,105}.

Data analysis

Analysis of the data was performed in two parallel independent processes, the targeting and the imaging analysis.

Targeting analysis

The targeting pipeline yielded the focal area, the incidence angle and the skull thickness scaling factor. The input values to the algorithm were limited to the nine parameters utilized for the stereotactic configuration at the sonication site and resulted in the vector of axial propagation and the focal area after the application of linear transformations. To visualize the targeting on the monkey brain, the resulting ellipsoidal shape was projected on the reference T1-weighted image as shown in Figure 9b. The information provided by this step was used to estimate the focal area and the center of the focus (Figure 9c). The next step was the skull extraction from the reference T1-weighted scan by segmentation. Although MRI is not the preferred imaging modality for skull information, the correlation between the MR-estimated and the CT-estimated skull thickness results in a correlation coefficient on the order of 0.8 and therefore the calculations were performed on the MR images. The skull line was isolated and mapped onto the global coordinate system by a custom curve fitting algorithm. The superposition of the axial vector on the skull print resulted in their point of intersection I (x_I, y_I, z_I), utilized to obtain the tangent to the skull. The tangent vector was estimated as the derivative of the skull curvature at the point of

intersection.

The

incidence

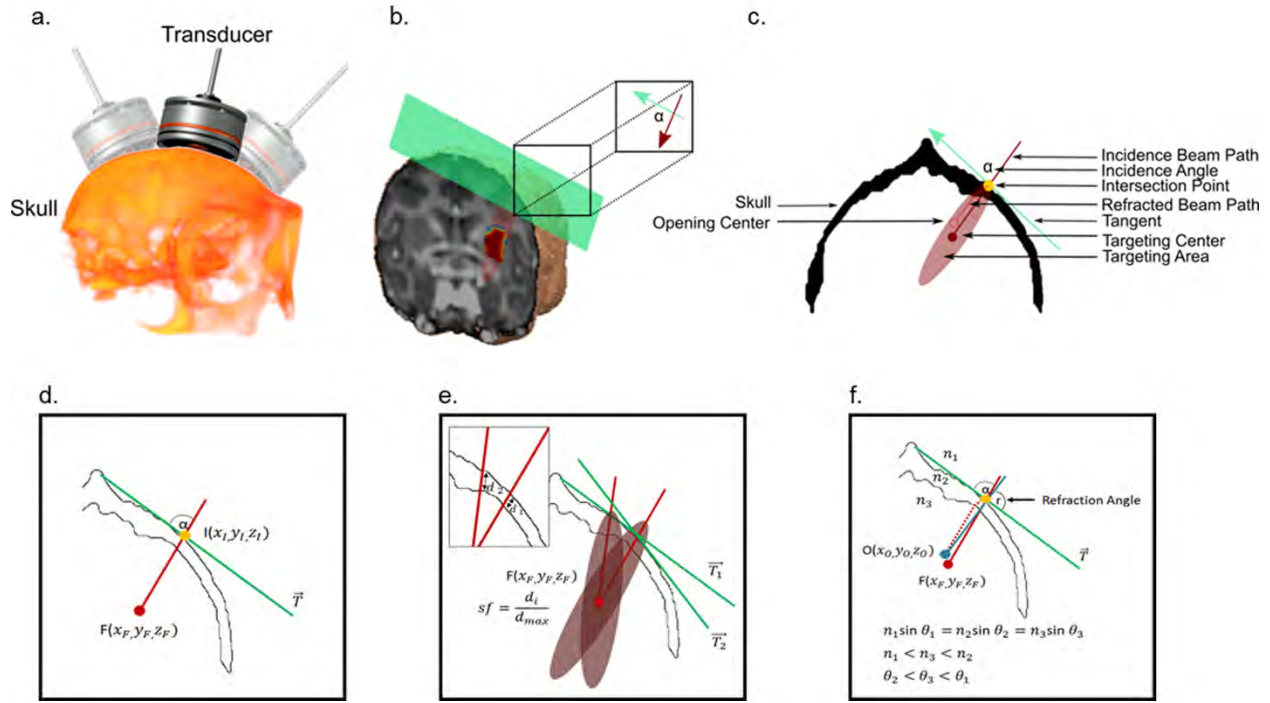


Figure 9: a. 3D representation of the NHP skull obtained from the CT. The transducer in solid color is aligned with the skull in a matching curvature regimen while the transparent transducers represent cases of not aligned curvatures. Aligned curvatures result in sonications with normal incidence angle. b. 3D reconstruction of the BBB opening with the focal region of the axial vector (red cylinder), the tangent plane on the skull (green plane) and the incidence angle (α) projected. c. Schematic of the skull and definitions of the abbreviations used. d. Closer look at the schematic to define the incidence angle. e. Closer look at the schematic to define the skull thickness factor, sf , for two different incidence angles. f. Closer look at the schematic to define the refraction angle.

angle was calculated as the angle (α) between the axial vector (\vec{V}) and the tangent (\vec{T}) as illustrated in Figure 9d based on their dot product.

$$\alpha = \cos^{-1} \frac{\vec{V} \cdot \vec{T}}{|\vec{V}| \cdot |\vec{T}|} \quad (1)$$

The process of incidence angle calculation was repeated for several times per experiment to minimize the variance resulting from the tangent vector estimation. The values presented here correspond to the mean incidence angle followed by the variance as the error of the measurement. The analysis was performed in the 3D domain but the angle of interest is being

formed by the axial direction (z-direction) described by two complementary planes, the z-x and the z-y planes. Therefore, the effect of the angle in one of these planes holds for the other as well. The coronal plane reported here corresponds to the z-x plane. The projection of the beam vector onto the skull yielded the thickness to which the corresponding incidence angle was associated. The scaling factor, “sf”, was calculated as the ratio of the skull thickness measured at each sonication (d_i) over the maximum measured thickness (d_{max}) to scale the factor to unity.

$$sf = \frac{d_i}{d_{max}} \quad (2)$$

The targeting accuracy was evaluated by the Euclidian distance of the BBB opening center O (x_O, y_O, z_O) from the targeting center F (x_F, y_F, z_F). The magnitude of the geometric shift ($\Delta g = \overline{FO}$) is susceptible to the refraction resulting from the variance in the media indices, an estimate of which is given by the corresponding angle shift ($\Delta\alpha = |\alpha - r|$, with r the refraction angle).

Finally, the reference scan of each NHP was utilized to construct a five level segmentation map of the monkey brain by employing the K-means segmentation method. Overlaying the focal area onto the segmentation map revealed the percentage of gray and white matter targeted.

Image processing

The image processing algorithm resulted in the volume of opening quantification, the targeting accuracy estimation and the percentage of opened gray-to-white matter ratio. Precise analysis imposed the registration of all T1-weighted images to the reference stereotactically aligned T1-weighted image using FSL’s FLIRT routine. According to the sequence fundamentals, bright areas corresponded to increased contrast agent concentration and distribution including

vasculature tracts. It is expected though, that in the T1w-post images enhancement should also be observed at the BBB disruption site. For each experiment the T1w-pre image and the corresponding T1w-post image were scaled with the muscle intensity to bring the images in comparable range. Aiming at the extraction of the V_{BBB} , the ratio of the T1w-post over the T1w-pre image was obtained, generating the ratio-image. Physiological and magnetic inhomogeneities and asymmetric vasculature resulted in unrelated to opening enhancements that were treated with filtering. Finally, the BBB opening was defined as the integration of the hyperintense voxels exceeding the threshold of 1.1 of the ratio image. The quantification of the distance between the focal center and the center of mass yielded the axial and lateral shift of the BBB opening from the targeted region. To perform this analysis centroid of the opening was established as the most hyperintense voxel in the surrounding spherical region of interest (ROI) (radius=3 mm) of the focal center, assuming linearity between the voxel intensity and the tracer concentration.

In silico numerical simulations

To strengthen the robustness of the in vivo measurements, numerical simulations were employed to investigate the incidence angle-effect on the pressure distribution. Therefore, the 3D k-space pseudospectral method (k-Wave) was employed to simulate the acoustic wave propagation with the second-order wave equation resulting in the transcranial PNP profile under the varying incidence angle concept. The acoustic emission source was the single element ring-shaped transducer while the sonication parameters (frequency, PRF, duration and duty cycle) were identical to the in vivo part of the study¹⁰⁶. CT images (helical scan, resolution = $200 \times 200 \times 600 \mu\text{m}^3$; Siemens) were acquired for one of the NHP's included in this study, providing the acoustic properties of the skull (density and speed of sound) converted from the Hounsfield units

in CT, with an attenuation of 20dB/cm and the power law absorption exponent of 1.1^{107} . The medium properties around the skull were the same as water at body temperature (37°C, speed of sound = 1524 m/s, density = 1000 kg/m³, attenuation = 3.5×10^{-4} dB/cm)¹⁰⁸. The CT enabled also the estimation of the skull thickness for every emission angle, while its segmentation was utilized to estimate the incidence angle and compare it to the results obtained from the MRI segmentation.

3.1.4 Results and Discussion

The analysis of 64 sonications resulted in the identification of the correlation between the incidence angle of the axial vector and V_{BBB} , the estimation of the geometric shift of the V_{BBB} from the target, the skull thickness interference with the incidence angle and finally the V_{BBB} overlap with the underlying physiological structures of white- (WM) and gray matter (GM).

The linear increase of the opening volume with incidence angle was confirmed by sonicating at three different pressures for five or more times resulting in the three corresponding scatter plots illustrated in Figure 10a. The table is summarizing the samples' number, the fixed pressure and the determination coefficient for each plot. It was also confirmed with extensive experiments that the variability in opening volume at different pressures resulted from the variability in the incidence angle. Therefore, when the incidence angle was fixed at a certain value the linearity was restored. Figure 10b demonstrates this effect for three different incidence angles. Finally, the reproducibility of our technique was confirmed by repeated sonications with fixed acoustic and stereotactic parameters. The results are presented as the mean with the standard error of the mean (SEM) for three sets of parameters tested in Figure 10c.

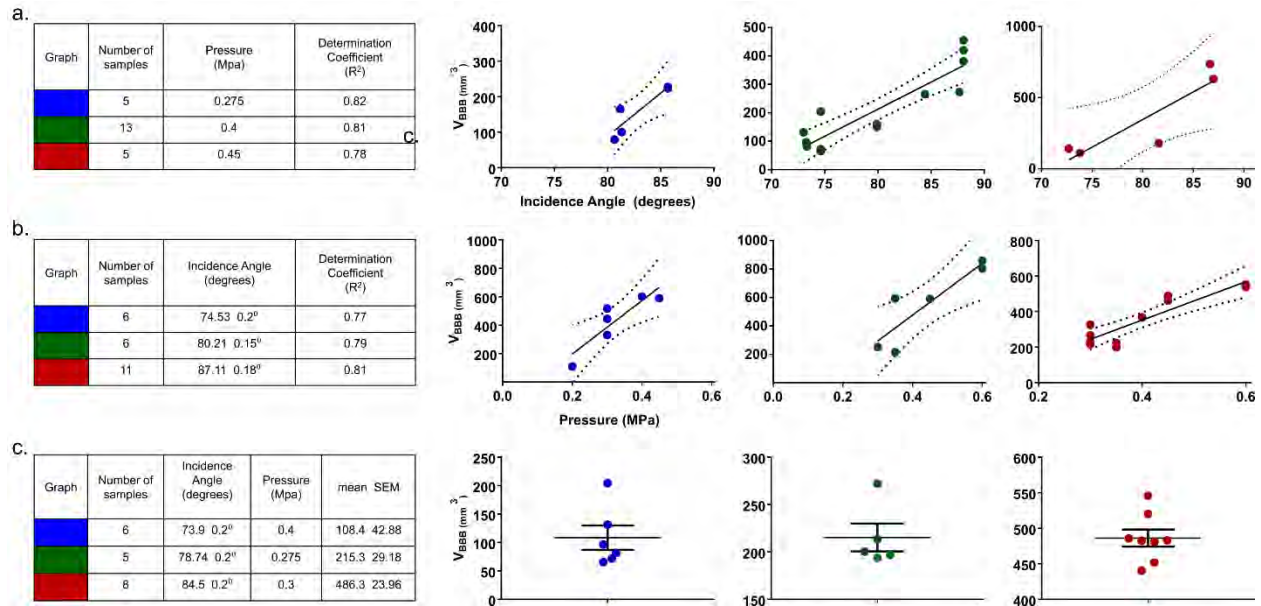


Figure 10: a. Linear regression of the opening volume with increasing incidence angle at three different pressures. The variables are listed in the table preceding the graphs. b. Linear regression of the opening volume with increasing pressure at three different incidence angles. The variables are listed in the table preceding the graphs. c. Repeatability of the opening volume at fixed pressure and incidence angles. The variables are listed in the table preceding the graphs.

Pairwise observations provide further insight into the correlations. The most interesting finding in this study was the strong dependence of the V_{BBB} on the incidence angle of the propagating wave. Figures 10 and 11 show that at a fixed PNP, a strong correlation exists between the incidence angle and the V_{BBB} . The pressure applied was kept constant and the angle against the opening size was plotted to demonstrate that the opening increases with incidence angle, confirming the hypothesis that a normal angle is preferred for larger openings. This is true due to the shorter propagation path through the skull after alignment of the transducer curvature to the skull lines and thus lower susceptibility to attenuation effects. By maintaining the incidence angle fixed and increasing the PNP, the BBB opening volume was steadily increased confirming previous findings in rodents. This observation was confirmed by both qualitative and quantitative findings. Ultimately, by varying both the PNP and angle the BBB opening volume can be altered

accordingly to achieve the desired treatment by simultaneously protecting the neighboring regions. On the other hand, by keeping both parameters fixed over the course of treatments the same opening can be reproduced (Figures 10c and 11c). This indicates a priori planning of the incidence angle and the applied pressure for each subject separately.

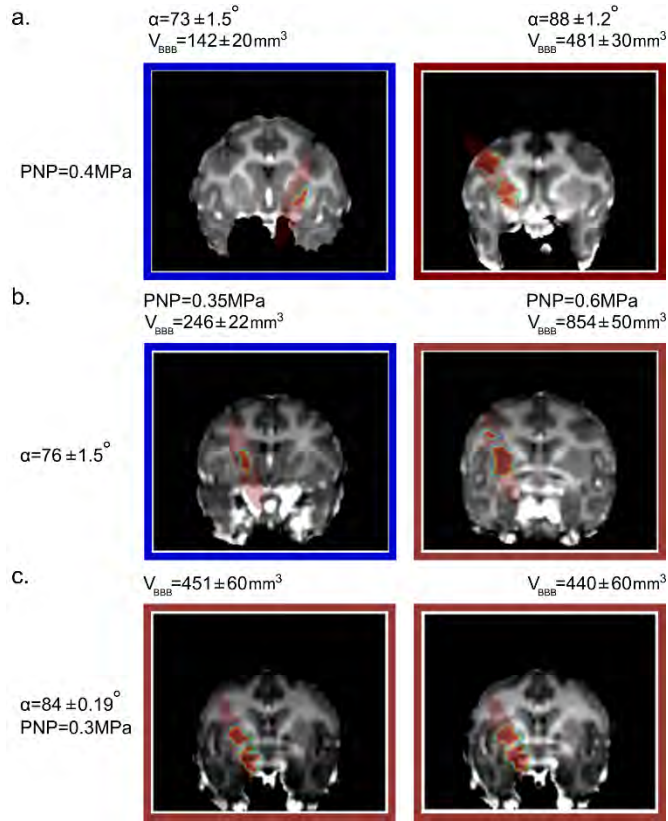


Figure 11: a. Qualitative results showing increase of the volume of opening with incidence angle for fixed pressure, 0.4MPa. The NHP in the blue outline was sonicated at $73 \pm 1.5^\circ$ yielding an opening of $142 \pm 20 \text{ mm}^3$ while the NHP in the red outline yielded an opening of $481 \pm 30 \text{ mm}^3$ when sonicated at $88 \pm 1.2^\circ$. b. Brain images showing the increase of the volume of opening with pressure given a constant incidence angle, $76 \pm 1.5^\circ$. The NHP in the blue outline was sonicated at 0.35 MPa and yielded an opening of $246 \pm 22 \text{ mm}^3$ while the NHP in the red outline was sonicated at 0.6MPa yielding an opening of $854 \pm 50 \text{ mm}^3$. c. Qualitative results showing the repeatability of the technique. Both NHPs were sonicated at $84 \pm 0.19^\circ$ and 0.3MPa and yielded openings of $451 \pm 60 \text{ mm}^3$ and $440 \pm 60 \text{ mm}^3$ respectively.

These findings were confirmed in silico by numerical simulations showing that increase of the incidence angle resulted in a more uniform PNP profile shifted towards higher pressures (Figure 12). Manipulation of the incidence angle and the pressure is of immense importance since various configurations of angle and pressure could be achieved. In the case of clinical trials, angle variation is valuable in avoiding specific structures while lower pressures will be applied. Furthermore, numerical simulations were comparable to the in vivo results in the context of incidence angle estimation and skull thickness effect.

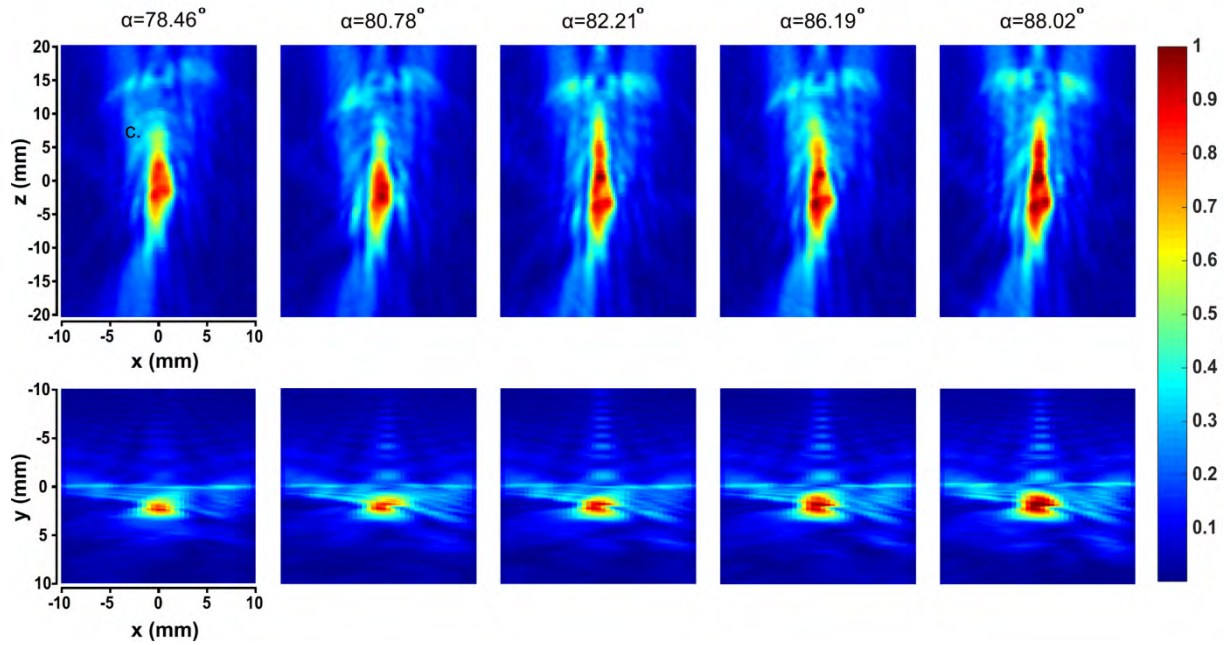


Figure 12: Numerical simulations with increasing incidence angle and constant pressure at 0.3 MPa, Axial and lateral profile for the five angles respectively, 78.46, 80.784, 82.21, 86.19 and 88.02. The PNP field was normalized with the maximum pressure across simulations.

Another interesting observation is the non-uniform shape of the opening site in several cases, some of which are presented in Figure 11. This observation suggested a more thorough investigation of the underlying physiology that could affect the BBB opening volume distribution. Therefore, measurements of the gray-to-white matter ratio at the targeted and the opened site showed that regardless of the targeting trajectory, the opening percentage on gray

matter is in the range of 75-90% while the white matter occupies only 10-25% of the opening site. This finding was observed in all NHPs and was found invariant of the ultrasound parameters. Regional differences in vascularization and subsequent microbubble concentration play a significant role in the probability of inducing an opening. It has been established that gray matter is highly dense in capillaries unlike white matter while variation even within gray matter depends on the structure's metabolic demand and synaptic needs^{109,110}.

The targeting accuracy was estimated by the axial shift on the order of 2.36 ± 1.74 mm towards the direction of the transducer and the lateral shift on the order of 1.18 ± 1.05 mm to the lateral direction when targeting the Putamen region. For the Caudate nucleus the displacements were 1.58 ± 1.02 mm towards the direction of the transducer and 1.05 ± 0.37 mm to the lateral direction. The errors correspond to the standard deviations. Apart from the geometric displacement of the opening, its orientation is of equal importance whereas the divergence of the refraction angle from the incidence angle was $4.5 \pm 3^\circ$ when targeting the Putamen region and $3.65 \pm 1.3^\circ$ at the Caudate nucleus. Finally, T2-weighted and SWI imaging confirmed the safety of the repeated sonications under the selected sonication regime.

3.1.5 Limitations and Conclusions

As described in the methods' section, the angle estimation was based on the superposition of the stereotactic geometry on the skull line and therefore the angle calculation could be considered indirect. This indirect method is susceptible to errors resulting from image artifacts, skull extraction algorithm or tangent plane estimation. Averaging eliminates these analysis' errors but a direct method of the angle calculation would be more robust.

Furthermore, erroneous positioning of the manipulator and the drivers could result in divergence from the desired and designed focus resulting to misleading interpretations of the results on geometric shift. Further investigation in the white and gray matter diffusion mechanisms is necessary and is pointing towards the direction of diffusion- and perfusion-based MRI techniques.

Further investigation of the diffusion components affecting the physiology of the targeted structures should give more insight into the mechanisms involved in BBB opening.

In this aim, the dependence of the BBB opening volume on the incidence angle, the effect of the gray-to-white matter ratio on the BBB opening shape and the targeting accuracy were established. It was found that the BBB opening volume increased monotonically with both the incidence angle and PNP. Pairwise observations revealed the linearity between the V_{BBB} and the incidence angle at the same pressure and interchangeably the monotonic increase of the V_{BBB} with PNP at the same angle. As expected, the V_{BBB} induced by the same incidence angle and PNP over the course of several sonications at different days resulted in comparable results. These findings indicate that the BBB opening volume can be predicted and planned by the selection of the corresponding combination of incidence angle and PNP. Additionally, the opening was found to be five times more pronounced in the gray matter than in the white matter indicating the effect of gray-to-white matter ratio on the BBB opened region. Finally, the technique was proven accurate and safe, given the shifts were deemed acceptable and the corresponding safety scans did not show evidence of damage.

3.2 Contrast-free detection of the focused ultrasound-induced blood-brain barrier opening with magnetic resonance imaging in non-human primates, in vivo.

3.2.1 Abstract

FUS has emerged as a non-invasive technique to locally and reversibly disrupt the blood-brain barrier (BBB). Here, we investigate the use of diffusion tensor imaging (DTI) as a means of detecting FUS-induced BBB opening at the absence of an MRI contrast agent. A non-human primate was treated with FUS and preformed circulating microbubbles to transiently disrupt the BBB ($n = 4$). T1- and diffusion-weighted MRI scans were acquired after the ultrasound treatment, with and without gadolinium-based contrast agent, respectively. Both scans were registered with a high-resolution T1-weighted scan of the NHP to investigate signal correlations. DTI detected an increase in the fractional anisotropy from 0.21 ± 0.02 to 0.38 ± 0.03 (82.6 ± 5.2 % change) within the targeted area one hour after BBB opening. Enhanced DTI contrast correlated with hyper-intense areas of gadolinium-enhanced T1-weighted scans, indicating diffusion enhancement only within the BBB opening area. Diffusion enhancement was highly anisotropic and unidirectional within the treated brain region, as indicated by the direction of the principal diffusion eigenvectors. Polar and azimuthal angle ranges decreased by 35.6% and 82.4%, respectively, following BBB opening. In conclusion, DTI may be used as a contrast-free MR imaging modality in place of contrast-enhanced T1 mapping for detecting BBB opening during focused-ultrasound treatment or evaluating BBB integrity in brain-related pathologies.

3.2.2 Introduction

Brain tumors and neurodegenerative diseases remain undertreated largely due to the presence of the BBB. FUS in conjunction with pre-formed microbubbles has been studied for more than 15 years as a means to facilitate the delivery of a wide range of therapeutic agents^{76,111–115} through the BBB. Following a large body of promising pre-clinical work, a number of clinical trials are currently in progress, aiming to efficiently and safely open the BBB in patients with Alzheimer's disease¹¹⁶, glioblastoma¹¹⁷ and amyotrophic lateral sclerosis¹¹⁸. The gold standard for the detection of FUS-induced BBB opening is contrast-enhanced T1-weighted MRI^{64,101,116,117,119}. Gd-based contrast agents (GBCAs) typically have a molecular weight of approximately 600 Da and are naturally impermeable to the intact BBB. Given their size, GBCAs can delineate even moderate BBB opening and also provide spatiotemporal information of vascular permeability variation via dynamic contrast-enhanced (DCE) MRI^{48,101,120,121}.

Although GBCAs have an established safety profile, there are raising concerns regarding their toxicity and tissue retention. Linear GBCAs have been occasionally correlated with hypersensitivity reactions and nephrogenic systemic fibrosis^{122,123}. There has been evidence that Gd is retained within certain areas of the brain (e.g., the dentate nucleus) following repeated administration of linear GBCAs^{124–127}, an effect which is exacerbated in subjects with renal impairment^{128,129} and in pediatric patients^{130,131}. Regulatory authorities have therefore recommended the gradual replacement of linear GBCAs with macrocyclic GBCAs that have a lower retention rate and limited deposition into the brain^{132,133}. However, the long-term effects of Gd retention in the brain are currently still unknown.

The growing safety concerns over GBCAs surfaced the necessity to explore non-Gd alternatives. The carboxymethyldextran coated-iron oxide nanoparticle, Ferumoxytol, has been investigated as a potential candidate¹³⁴. However, lacking the molecular characteristics and pharmacokinetic properties of GBCAs, it provided only complementary information and was deemed unsuitable for BBB disruption detection¹³⁴. To overcome the shortfalls of iron oxide nanoparticles, complexes of manganese-based contrast agents were developed^{135,136}. Manganese is a trace element, essential for physiological body functions, with strong paramagnetic properties inducing increased relaxation^{135,136}. However, engineering effective and stable manganese-based contrast agents has been proven challenging but promising following the development of the Mn-PyC3A compound¹³⁵. Additionally, arterial spin labeling has been also introduced as a substitute to contrast-enhanced imaging techniques, primarily focusing on the quantitative measurement of tissue perfusion¹³⁷. Despite the alternatives, further investigation is needed to completely replace contrast-enhanced MRI with contrast-free MRI as the gold standard for evaluating spatial variations in BBB integrity and FUS-induced BBB opening in particular.

Herein, we explore and evaluate the potential of diffusion-weighted imaging (DWI) as a promising candidate for replacing contrast-enhanced T1-weighted imaging in detecting BBB permeability. DWI has been extensively used in brain applications including the diagnosis of stroke^{138–140}, edema formation¹⁴¹, subarachnoid hemorrhage¹⁴² and multiple sclerosis^{143,144}. In this context, diffusion refers to the random translational motion of molecules (i.e., Brownian motion) driven by the thermal energy carried by the molecules^{145,146}. During displacement, molecules probe the surrounding tissue at a microscopic scale. The resulting displacement distribution, reflecting differences in tissue organization, is captured in the DWI image

contrast¹⁴⁷. The capabilities of this technique expand further to the detection of the displacement directionality (isotropic or anisotropic) associated with gradient pulses driven at different directions sensitizing displacements along that direction¹⁴⁶, namely the diffusion tensor imaging (DTI)^{146,148}. In DTI, diffusion-weighted images are acquired along multiple directions (i.e. at least 6 directions) along with an image acquired without weighting ($b = 0 \text{ s/mm}^2$) in order to populate the diffusion tensor, which is a three-by-three, symmetric, positive definite matrix¹⁴⁸. Diffusion tensor D is connected with the diffusion-weighted signal intensity S_k and the $b = 0 \text{ s/mm}^2$ signal S_0 via the Stejskal and Tanner equation^{149,150}:

$$S_k = S_0 e^{-\hat{g}_k b \hat{g}_k^T D}, \text{ with } b = \gamma^2 G^2 \delta^2 \left(\Delta - \frac{\delta}{3} \right) \quad (3)$$

where \hat{g}_k is the k th gradient direction, γ is the gyromagnetic ratio, G is the amplitude of the diffusion gradients, δ is the diffusion gradient duration, and Δ is the interval between two successive diffusion gradients on either side of the refocusing pulse¹⁴⁹. The eigenvectors (v_1, v_2, v_3) and eigenvalues ($\lambda_1, \lambda_2, \lambda_3$ with $\lambda_1 \geq \lambda_2 \geq \lambda_3$) of the diffusion tensor D can be computed to characterize the diffusion ellipsoid in each voxel. Spherical ellipsoids ($\lambda_1 \approx \lambda_2 \approx \lambda_3$) indicate symmetric and isotropic water diffusion, while planar ($\lambda_1 \approx \lambda_2 > \lambda_3$) and tubular ($\lambda_1 > \lambda_2 \approx \lambda_3$) ellipsoids indicate asymmetric and anisotropic water diffusion. Anisotropic water diffusion is routinely employed to identify white matter tracts at high resolution, in MR tractography applications^{150–152}. A frequently used metric of diffusion anisotropy in the interval $[0,1]$ is fractional anisotropy (FA), a non-linear combination of the eigenvalues defined as^{153,154}:

$$FA = \sqrt{\frac{3}{2} \frac{(\lambda_1 - \lambda_2)^2 + (\lambda_1 - \lambda_3)^2 + (\lambda_2 - \lambda_3)^2}{\lambda_1^2 + \lambda_2^2 + \lambda_3^2}} \quad (4)$$

FA maps have been previously used to identify the causes of epilepsy¹⁵⁵, schizophrenia¹⁵⁶, amyotrophic lateral sclerosis¹⁵⁷, and dyslexia¹⁵⁸. Additionally, FA mapping can identify morphological changes in axons following traumatic brain injury¹⁵⁹. Interestingly, FA values change following repeated BBB disruption induced by traumatic brain injury in football players¹⁶⁰. In the context of FUS-mediated BBB opening, DTI revealed normal microstructure and tissue integrity in repeatedly treated rodents over a period of months¹⁶¹.

In this study, we hypothesized that a localized FUS-induced BBB opening will induce a change in the diffusion ellipsoids within the targeted area. The direction of the principal diffusion vector v_1 and the FA values were both expected to locally change after FUS treatment due to the anisotropic stresses exerted by asymmetric microbubble oscillations within the microvasculature¹⁶². This hypothesis was investigated in a NHP model, which closely resembles the human brain and skull. The correlation between the contrast-enhanced T1-weighted and DTI was examined in terms of accurately detecting and quantifying the FUS-induced BBB opening. The overall aim is to provide an alternative to the potentially toxic GBCA systemic injection required for T1-weighted MRI with a Gd-free MR sequence.

3.2.3 Materials and Methods

***In vivo* experiments**

The experimental procedure was similar to the one described previously (section 3.1.4). Briefly a male rhesus macaques (*Macaca mulatta*) was employed for this study while at least two weeks were interleaved between sessions. During each procedure, the animal was immobilized by intramuscular administration of a cocktail containing 1ml ketamine (5-15 mg/kg) and 1ml

atropine (5-15 mg/kg), while in the operation room, the animals were anesthetized by inhalation of 1–3% isoflurane. The transducer was attached to the Kopf stereotaxic manipulator to allow for targeting the brain in the stereotaxic coordinate frame and the animals were transferred to the MRI site immediately after the sonication (Figure 13a).

Focused ultrasound

Similar to the previous section (section 3.1.3), the sonications were carried out by a single-element, spherical-segment FUS transducer operating at 0.5 MHz with a flatband, spherically focused hydrophone confocally alligned at the central void of the transducer. In-house manufactured, lipid-shell, monodisperse microbubbles with a mean diameter of 4 to 5 μm were diluted to 2×10^5 # bubbles/mL. The microbubbles at a dosage of 2.5×10^8 # bubbles/kg were intravenously injected through the saphenous vein 10 sec after the onset of sonication to allow for real-time monitoring of the microbubble cavitation described elsewhere. The animals were sonicated in the Caudate nucleus for 120 sec, at an incidence angle of $85 \pm 2^\circ$, pulse length pulse repetition frequency of 2 Hz, pulse length of 10 ms and PNP at 0.45 MPa.

The targeting optimization performed previously (section 3.1.4) resulted in the selection of optimal stereotactic parameters with a normal incidence angle. This parametric space was utilized in this aim to achieve the largest opening volume in the Caudate nucleus under the safety regime while was kept constant to ensure repeatability. Evaluation of the targeting accuracy was performed by implementation of the stereotactic device's geometric characteristics into the MATLAB algorithm described previously (section 3.1.4) resulting into the overlay of the focal beam to the BBB opening.

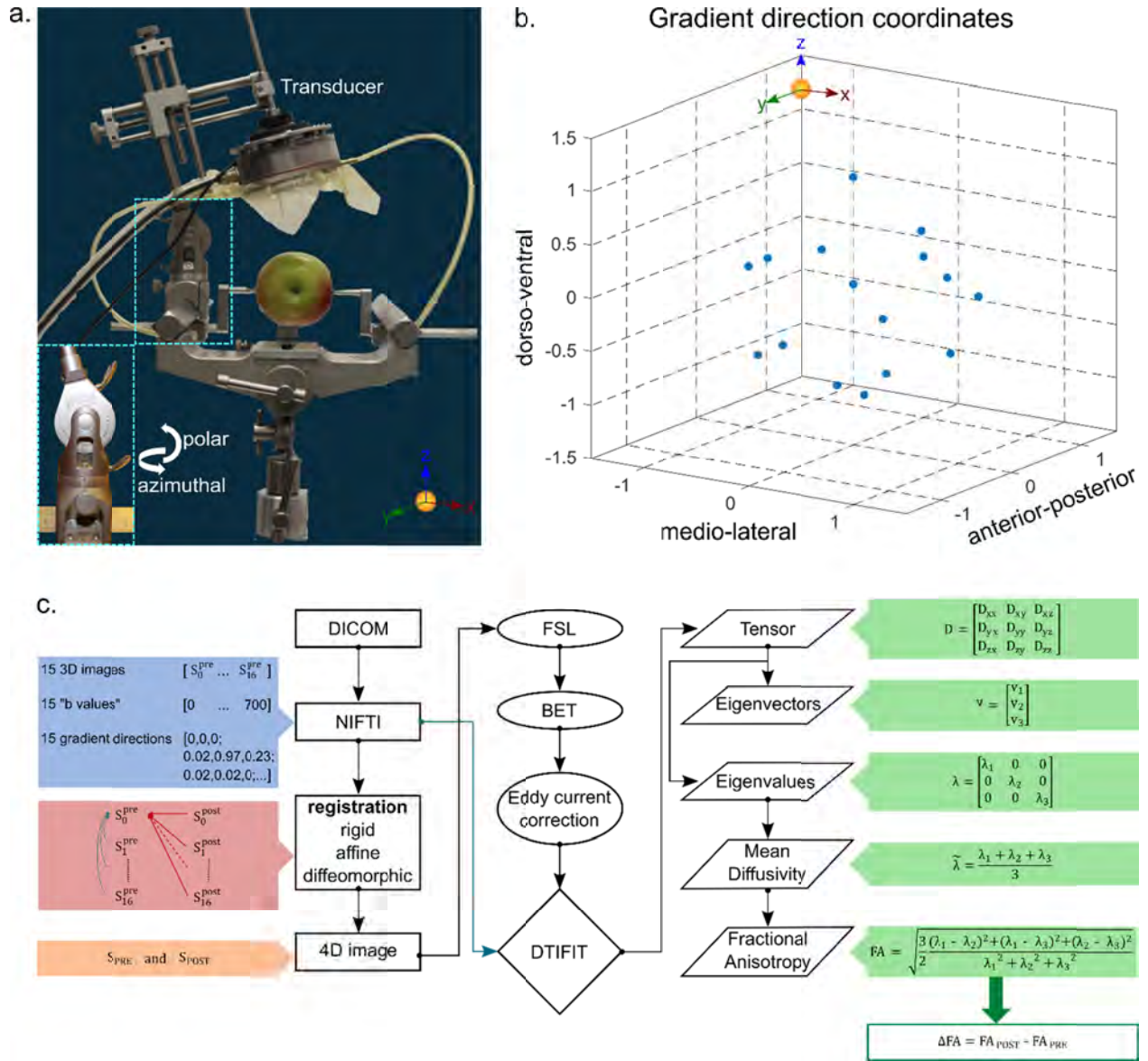


Figure 13: a. Transducer orientation relative to the brain fixed on the stereotactic frame. b. Gradient direction coordinates are presented to confirm that diffusion sampling occurred in the entire sphere, a requirement imposed by the eddy current correction accuracy. c. Flowchart of the DTI processing pipeline. The raw data were transformed from DICOM to NIFTI format and all the directions were registered to the weight- and gradient-free image of the scan acquired before the sonications. The registered images were combined in a 4D format that was isolated from the surrounding brain tissue and corrected for eddy current artifacts. Then, the calculation of the tensor and the corresponding eigenvalues and eigenvectors resulted from the DTIFIT. The mean diffusivity and the fractional anisotropy maps were quantified by employing the appropriate equations. The difference in the FA values is reported herein, denoted as ΔFA , and resulted from the subtraction of the FA map obtained before the sonication from the FA map acquired following the sonication.

Contrast-enhanced T1-weighted imaging protocol

Following the FUS procedure, the animal was transferred to the MRI scanner (3T Philips Achieva) for contrast-free DTI and contrast-enhanced T1-weighted imaging. As previously described¹¹⁹ high-resolution structural contrast-enhanced T1-weighted images were acquired (Gradient Echo, TR/TE= 11.16 ms /5.14 ms, flip angle= 8°, FOV= 120 x 120 mm², matrix size: 176 x 176, NSA=1, slice thickness 0.7 mm, 171 slices) at two time-points. The pre-sonication scan (T1_{PRE}) was acquired 30 minutes after intravenous administration of 0.2 ml/kg GBCA (gadodiamide) preceding any sonication while the post-sonication scan (T1_{POST}) was acquired after every sonication. T1-weighted imaging was employed as the gold standard in BBB opening detection to compare with the new imaging modality. DTI always preceded any contrast injection to avoid signal distortion due to the Gd presence.

DTI protocol and analysis

DTI sequence

The DTI protocol consisted of a multi-shot spin-echo echo planar DTI sequence with TR/TE= 3475/72 ms/ms, flip angle= 90°, FOV= 120 × 120 mm², matrix size: 128 × 128, NSA= 1, slice thickness 2 mm, 28 slices, 15 different weighted gradient directions and a b-value equal to 700 s/mm². An accelerated DTI scan with SENSE (Sensitivity encoding) factor 2 was acquired (scan time < 10 min) prior to the initiation of the experiments (DTI_{PRE}) and one immediately after every sonication (DTI_{POST}) to enable intra-brain comparison of the diffusion metrics before and after the BBB opening.

DTI registration with ANTS library

The raw data collected from the MRI scanner were converted from a digital imaging and communications in medicine (DICOM) format to a neuroimaging informatics technology initiative (NIFTI) format prior to the analysis (Figure 13c). The susceptibility of this technique to various artifacts and the necessity of single pixel precision dictated the need for a sophisticated registration algorithm. The Advanced Normalization Tools (ANTs) library was employed to register all directions of the DTI scans (DTI_{PRE} and DTI_{POST}) to the reference scan, which in this case was the diffusion gradient-free ($b = 0$ s/mm²), weight-free direction of the DTI_{PRE} scan, S_0^{PRE} (Figure 13c). ANTs is a software package, built on an Insight Toolkit framework, comprised of powerful tools for image registration and segmentation¹⁶³ that belongs to the highest-ranking registration methods¹⁶⁴. The default executable “antsRegistrationSyN” that was implemented, performs a symmetric, geodesic diffeomorphic transformation. It follows the principles of an extended Lagrangian diffeomorphic technique¹⁶⁵, that based on a time-varying velocity field optimization results in the alignment of two images. Symmetric mapping guarantees that the path from the “moving” image to the “reference” image is the same as the path from the “reference” to the “moving” image regardless of the similarity metric and the optimization parameters¹⁶⁵. In this deformation space, the shortest paths between elements are termed geodesic while diffeomorphism refers to a differentiable map with a differentiable inverse¹⁶⁵.

The registration was initialized with rigid and affine mapping (Figure 13c) to linearly transform the “moving” image to the orientation of the “reference” image. Linear transformation is necessary to meet the symmetric diffeomorphisms’ assumption of homogeneous boundary conditions (image borders map to themselves) for solutions restricted to the diffeomorphic

space¹⁶⁵. Hence, ANTs assumes that a diffeomorphism “ ϕ ” defined on the image domain “ Ω ” maintains an affine transform at the boundaries. Over time, the map “ ϕ ” parametrizes a group of diffeomorphisms by integrating a time-dependent, smooth velocity field described largely by^{163,165}:

$$u = \operatorname{argmin} \left\{ \int_0^1 ||Lu||^2 dt + \lambda \int \prod_{\sim} (I, \phi(x, t), J) d\Omega \right\}, \text{with} \quad (5)$$

$$\int_0^1 ||Lu||^2 dt \text{ the regularization term and} \quad (6)$$

$$\lambda \int \prod_{\sim} (I, \phi(x, t), J) d\Omega \text{ the similarity metric} \quad (7)$$

where u denotes the velocity, L the smoothing operator, t the time, λ controls the matching exactness, x is the spatial position, \prod_{\sim} is the similarity metric and I is the moving image to be transformed to the reference image J . In the registration schema employed herein, geodesic transformation with Gaussian regularization was the transformation model of choice along with the Mutual Information metric as the similarity measure and Gradient Descent accounting as the optimization method¹⁶³.

Following the registration, all directions per scan were organized into a 4D matrix (one 3D image per gradient) that along with the corresponding gradient directions and the weighting factors was used by FSL’s FDT Diffusion platform as input¹⁶⁶. Prior to further processing, the brain tissue was isolated from the skull and the muscle by employing FSL’s Brain Extraction Tool (BET) with the default fractional intensity threshold, 0.5¹⁶⁷. Eddy current correction followed the brain masking by simulating the diffusion signal using a Gaussian Process assuming that: i) the signal from two acquisitions acquired with diffusion weighting along two vectors with a small angle between them is more similar than for two acquisitions with a large angle between them and, ii) the signal from two acquisitions along vectors v and $-v$ is identical.

The diffusion encoding directions have been chosen to span the entire sphere (Figure 13b) facilitating the distinction between signal variation caused by diffusion and that caused by eddy currents/movements¹⁶⁸. Finally, estimation of the tensor matrix was accomplished by utilizing FSL's DTIFIT command resulting in the calculation of the associated eigenvectors/eigenvalues (V_1 , V_2 , V_3 , L_1 , L_2 and L_3) and the corresponding maps.

Upon the local directionality of the water diffusion, every structure has a distinct FA value, while a change in that value was hypothesized to occur after BBB opening. To detect the change in the local diffusivity pattern, the difference in the FA maps was calculated, $\Delta FA = FA_{POST} - FA_{PRE}$. The resulting maps were smoothed using a two-dimensional median finite impulse response filter (2 x 1 pixels), in order to eliminate the noisy background. To visualize the local changes and their correlation to the BBB opening and the underlying anatomy, the ΔFA images were superimposed onto the anatomical images and the BBB opening. These T1-weighted high-resolution anatomical images were registered to the diffusion reference scan in MATLAB using a multimodal, three-dimensional, intensity-based, affine registration. This approach provided acceptable overlap between structures observed in T1 and DTI images, therefore more advanced registration was not attempted.

Quantification

Quantification of the BBB opening was performed in MATLAB for both imaging sequences. To detect the BBB opening, the ratio $RGd-T1 = Gd-T1_{POST} / Gd-T1_{PRE}$ was calculated following reference-intensity scaling between each $T1_{PRE}$ and $T1_{POST}$ pair¹¹⁹. The within-plane surface area of the BBB opening was calculated as the sum of the pixels with intensity surpassing the

threshold of 1.1. A similar approach was followed for the FA maps by calculating the Δ FA difference following reference-intensity normalization. Integration of the pixels surpassing zero resulted in the estimation of the within-plane BBB opening area. Although the entire volume of the BBB opening could be estimated from the anatomical images, that was not the case for the DTI. To minimize the acquisition time while increasing the number of gradient directions during DWI acquisition, the number of slices was decreased resulting in the observation of the BBB opening in primarily a single plane. Therefore, for consistency and comparability of the BBB opening between the two modalities, the BBB surface area is being compared between the FA and the gold standard.

To assess any changes in the diffusion pattern following BBB opening, the average FA value within the BBB opening area has been quantified. To report on the directionality of the molecules, the polar and azimuthal angles of the primary eigenvectors have been summarized in polar plots with an angle bin of 5°. Finally, the polar and azimuthal angle ranges have been quantified for both ipsilateral and contralateral hemisphere, used here as the control.

Statistical analysis

Data shown here are presented as mean \pm standard deviation (n = 4 FUS treatments). Comparisons between FA_{PRE} and FA_{POST} values and angle ranges were analyzed using a two-tailed paired Student's t-test while comparison of the BBB opening size between modalities was conducted with two-tailed unpaired Student's t-test. In all analyses, the null hypothesis was rejected at the 0.05 level. All statistical analyses were performed using Prism 8 (GraphPad Software, San Diego, CA, USA).

3.2.4 Results and Discussion

Diffusion tensor imaging and the corresponding metrics succeeded not only in detecting the site of blood-brain barrier leakage but more importantly, in unveiling, for the first time, the direction of the diffusion gradient. Figure 14 summarizes the results from four consecutive experiments conducted in a non-human primate. The first row corresponds to the RGd-T1 of the BBB opening (jet colormap), resulting from the analysis of the T1-weighted imaging, overlaid onto the anatomical scan (gray colormap) in the axial plane. The targeting trajectory was similar across experiments while the similarity in the opening site indicated successful repeatability. The ΔFA , the difference in the fractional anisotropy maps (jet colormap), is presented in the second row, overlaid on the same anatomical scan. Strong signal is detected at the site of the BBB opening, similar to the T1-weighted images. Quantification of the BBB opening surface area on the axial plane corresponding to the center of the opening showed comparable sizes across experiments for both sequences. The opening size was measured to be on the order of $34.01 \pm 6.37 \text{ mm}^2$ and $28.56 \pm 7.61 \text{ mm}^2$ for the Gd-T1-weighted sequence and the ΔFA map, respectively (Figure 14 and Table I).

Table I: Quantification of BBB opening area, fractional anisotropy, and primary eigenvector angular range.

		Surface area Gd-T1w (mm ²)	Surface area ΔFA (mm ²)	ΔFA increase (%)	FA_{PRE}	FA_{POST}	Polar Ipsilateral Post BBB (degrees)	Polar Ipsilateral Pre BBB (degrees)	Polar Contralateral Post BBB (degrees)	Azimuthal Ipsilateral Post BBB (degrees)	Azimuthal Ipsilateral Pre BBB (degrees)	Azimuthal Contralateral Post BBB (degrees)
NHP1	Experiment 1	42.13	36.91	75.83	0.24	0.43	42.11	63.14	70.50	20.45	43.27	174.99
	Experiment 2	27.06	18.46	84.03	0.21	0.39	53.48	92.34	116.67	28.10	174.07	110.81
	Experiment 3	35.31	29.88	88.40	0.18	0.33	46.38	89.08	135.17	12.71	169.47	174.94
	Experiment 4	31.56	29.00	82.26	0.21	0.39	65.41	77.34	127.10	36.43	169.47	171.62
	Average \pm Std	34.02 ± 6.37	28.56 ± 7.61	82.63 ± 5.22	0.21 ± 0.03	0.38 ± 0.04	51.84 ± 10.19	80.47 ± 13.23	112.36 ± 28.91	24.42 ± 10.18	139.07 ± 63.9	158.09 ± 31.56

The mean FA was also quantified from the FA maps (FA_{PRE} and FA_{POST}) and found to significantly increase by 82% from 0.21 ± 0.02 to 0.38 ± 0.03 following the application of

ultrasound ($t[3]=27.73$; $P=0.0001$). The increase of FA was reversible, e.g. the region with opened BBB in the first FUS treatment was not enhanced in subsequent scans. This suggests that the detected FA increase is due to the reversible BBB opening and not to a permanent change within the gray matter, such as persisting edema or scar tissue.

The local change in diffusivity that co-localizes with the BBB opening was found to follow a preferred direction, hence the positive change in the FA value. This finding was confirmed by the vector field that depicts the vectors of the voxels corresponding to the BBB opening pointing towards one direction, with a high degree of anisotropy. In Figure 15, the BBB opening is overlaid on the primary vector field (v_1) and the magnified part of the brain shows the directionality of the vectors in the ipsilateral and contralateral caudate. Moreover, the primary diffusion eigenvectors (v_1) had consistent polar and azimuthal angles within the disrupted ipsilateral region ($v_{1\text{POST-IPSI}}$), in contrast to the same region prior to the opening ($v_{1\text{PRE-IPSI}}$) as well as the contralateral region ($v_{1\text{POST-CONTRA}}$), where in both latter cases the v_1 experienced a more isotropic and uniform angle distribution as shown by the angle plots in Figure 15. Quantification of the polar and azimuthal angles spanning range was estimated as the difference in the most distant angles (polar and azimuthal) for the three cases ($v_{1\text{POST-IPSI}}$, $v_{1\text{PRE-IPSI}}$, $v_{1\text{POST-CONTRA}}$) revealing a significantly narrower range only in the BBB opening cases. Cumulative results showed a decrease in the polar angle range of the $v_{1\text{POST-IPSI}}$ on the order of 35.58% ($t[3]=3.921$; $P=0.0295$) compared to the pre-sonication scan, $v_{1\text{PRE-IPSI}}$, and 53.86% ($t[3]=4.887$; $P=0.0164$) compared to the post-sonication contralateral side, $v_{1\text{POST-CONTRA}}$. Similarly, the azimuthal angle range of the $v_{1\text{POST-IPSI}}$ decreased by 82.44% ($t[3]=3.699$; $P=0.0343$) compared to $v_{1\text{PRE-IPSI}}$, and 84.55% ($t[3]=7.462$; $P=0.005$) compared $v_{1\text{POST-CONTRA}}$.

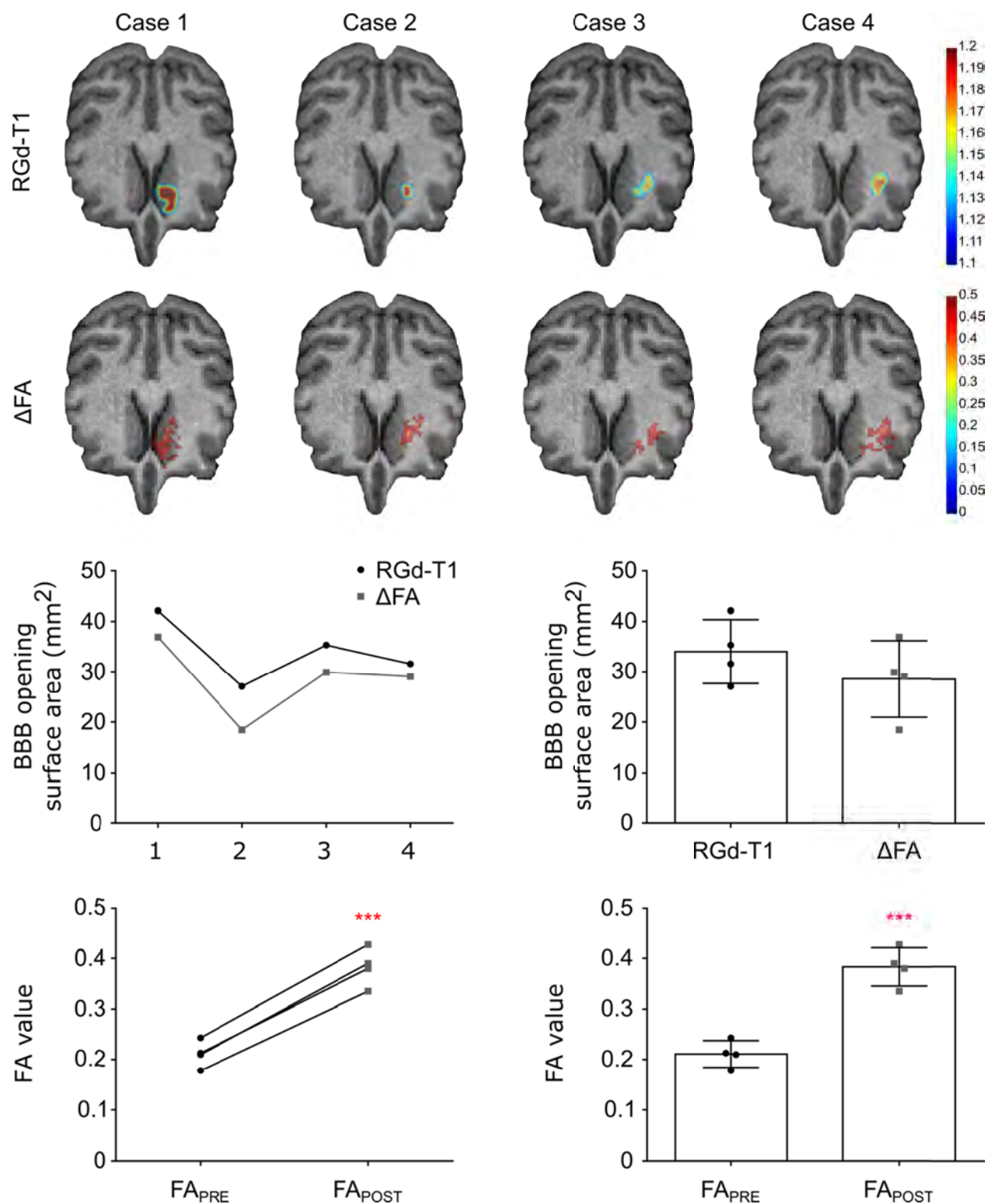


Figure 14: BBB detection with Gadolinium-Enhanced T1-weighted imaging and FA maps. Each case corresponds to a different experiment conducted on the same animal targeting a similar structure (Caudate nucleus). The T1-weighted images' ratio, RGd-T1, is presented against the difference in FA maps, ΔFA. Longitudinal assessment of the opening surface

area shows comparability of the two modalities both qualitatively and quantitatively. Accordingly, the average BBB opening surface area is similar between modalities. The FA value increased in all four cases following the sonication while increased on average by 82% from 0.21 ± 0.02 to 0.38 ± 0.03 ($t[3]=27.73$; $P=0.0001$).

The individual values of the BBB opening surface area, FA_{PRE} , FA_{POST} , ΔFA as well as the polar and azimuthal angle ranges for $V_{IPOST-IPSI}$, $V_{IPRE-IPSI}$, $V_{IPOST-CONTRA}$ are summarized in Table I.

Diffusion weighted images processed with non-linear registration and tensor analysis revealed the sites of BBB leakage that correlated well with the BBB-opened regions detected by Gd-T1-weighted imaging (Figure 14). Moreover, the FA maps showed an increase in the anisotropy in the area of BBB opening indicated by a positive increase in the FA amplitude, also confirmed by vector analysis and the respective angles (Figure 15). Mean diffusivity maps were also computed but no significant change was observed following the sonications. Based on prior findings, this observation could be attributed to the equivalence of averaging similar eigenvalues ($\lambda_1 \approx \lambda_2 \approx \lambda_3$) to averaging eigenvalues whereas the primary is distantly large compared to the remaining two ($\lambda_1 \gg \lambda_2 \approx \lambda_3$) (see mean diffusivity equation, Figure 13c).

The highly anisotropic nature of v_1 within the targeted area (Figure 15) was the underlying cause to the increased FA value. We hypothesize that increased anisotropy stems from the non-uniform stresses exerted by the oscillating microbubbles in the vicinity of cerebral blood vessels^{162,169}. Sonication at pulse lengths on the order of milliseconds can promote primary acoustic radiation forces^{170,171}, microbubble cluster formation^{172–174}, and microbubble coalescence¹⁷⁵, thus producing inhomogeneous stimuli and non-uniform BBB opening⁸⁷. Therapeutic FUS exposure forces microbubbles to move in the direction of ultrasound propagation at velocities on the order

of m/s, which is expected to lead in BBB opening sites primarily at the vessel walls distal to the

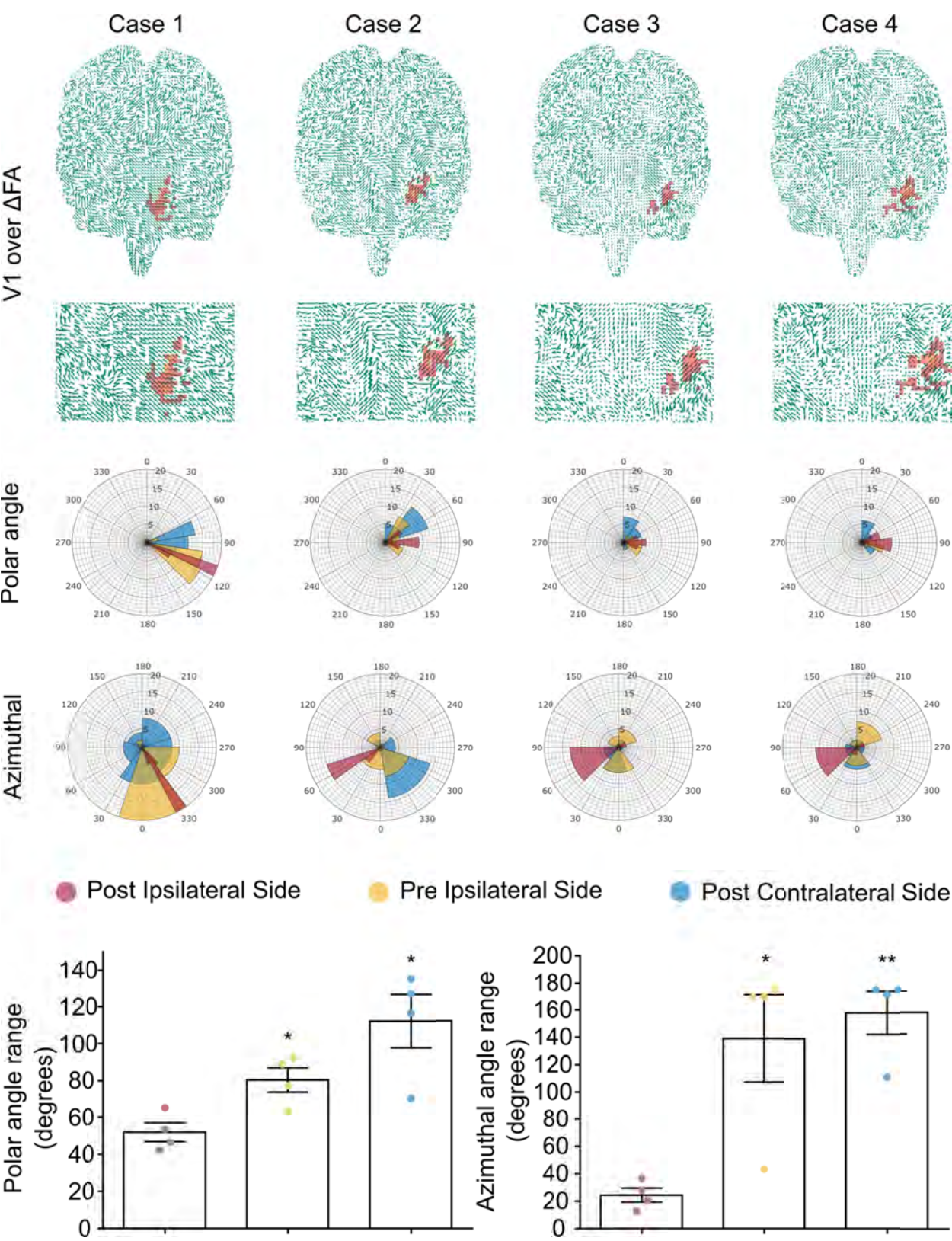


Figure 15: DTI eigenvectors overlaid onto the Δ FA map for the entire axial brain plane and the magnified striatal region. BBB opening initiates an increase in the directionality of the water molecule diffusion compared to the intact barrier shown by the consistent direction of the arrows in the sonicated area compared to the contralateral side. Polar and azimuthal angle distributions in the ipsilateral and contralateral hemispheres are presented showing the narrow range of polar and azimuthal angles of the principal eigenvector only at the site of sonication ($v_{IPOST-IPSI}$). Cumulative results showed a decrease in the polar angle range on the order of 35.58% ($t[3]=3.921$; $P=0.0295$) compared to the ipsilateral side, $v_{IPRE-IPSI}$, and 53.86% ($t[3]=4.887$; $P=0.0164$) compared to the contralateral side, $v_{IPOST-CONTRA}$. Similarly, the azimuthal angle range of the $v_{IPOST-IPSI}$ decreased by 82.44% ($t[3]=3.699$; $P=0.0343$) compared to $v_{IPRE-IPSI}$, and 84.55% ($t[3]=7.462$; $P=0.005$) compared $v_{IPOST-CONTRA}$.

FUS transducer^{176,177}. This hypothesis is supported by the similar directionality observed in both polar and azimuthal angles in all BBB openings (Figure 15). Another potential effect following BBB opening is a change in the CSF circulation pattern^{178,179}. Pressure gradients may temporarily affect the local CSF flow, leading to increased water diffusion anisotropy. Our sequences were able to detect the bulk FA increase, but other sequences such as phase-based amplified MRI^{180,181} may be needed to resolve sub-voxel CSF motion patterns. Another similar study conducted in rodents confirmed the increase in FA values following repeated sonications although using a different timeline. In that study the increased directionality was attributed to increased myelin integrity¹⁶¹.

3.2.5 Limitations and Conclusions

Regardless of the underpinning mechanism, the increase of FA is temporary and is restored upon BBB closing. Future work will investigate the temporal evolution of FA maps following BBB opening. Numerical modeling of interstitial pressure gradients and CSF flow following BBB opening may elucidate the mechanism driving the anisotropic water diffusion. We will compare ms-long pulse sequences against μ s-long pulse sequences, which were shown to produce more homogeneous microbubble activity in vitro¹⁷⁴ and more uniform BBB opening in vivo^{87,182}. We

anticipate that the diffusion anisotropy will be less pronounced following FUS treatment with μ s-long pulses. We also aim to correlate the BBB opening volume derived through DTI with passive cavitation mapping of microbubble activity within the NHP brain^{44,45,183,184}. Finally, the DTI quality can be further improved by adjusting the gradient tables and eliminating potential imaging artifacts due to subject motion¹⁸⁵.

In conclusion, in this aim a non-contrast MR-based imaging approach for BBB opening was described. The FA maps were shown to vary as a result of FUS-mediated BBB opening, and that change co-localizes with the GBCA extravasation area in contrast-enhanced, T1-weighted MRI. Therefore, DTI is concluded to constitute a reliable contrast-free alternative, which may be proven safer by avoiding MRI contrast to permeate into the brain parenchyma. DTI may be used in the clinic for detecting BBB opening following FUS treatment or evaluate BBB integrity in brain-related pathologies.

3.3 Contribution

It has previously been shown by numerical simulations that incidence angles deviating from normal lead to strong wave reflections and extremely high attenuations caused by the primate skull curvature¹⁰². However, the correlation of the incidence angle -corrected by the skull thickness- with the BBB opening volume was quantified and analyzed here for the first time, combining numerical simulations and in vivo experimentation. Regional differences in vascularization and subsequent microbubble concentration defined the probability of inducing a BBB opening.

Sonifications with optimized parameters (normal-to-the-skull-curvature incidence angle, pressure level, thin skull area) in a single NHP yield highly repeatable BBB openings detectable by DTI. For the first time, we proved that Gd-T1-weighted imaging can be substituted by contrast free imaging but more importantly, we established the anisotropic diffusion pattern following the BBB opening.

The overall contribution of this study is the identification of the parametric space of ultrasonic trajectories resulting in predictable BBB opening volumes for varying pressure levels. The expectation of inducing a BBB opening is five times higher in GM regions compared to WM matter hence the higher vascularization density. DTI employed as the BBB opening detection schema reveals the anisotropic nature of diffusion. The findings of these studies have been accounted for in the upcoming clinical trial restricting incidence angles to normal and selecting DTI as the detection sequence¹⁸⁶. The results of the studies described in this chapter have been published in peer reviewed scientific journals¹¹⁹ (Figure 16).

Regarding the research contribution, Professor Vincent P. Ferrera, Ph.D. (Associate Professor, Neuroscience, Psychiatry, Columbia University) provided assistance with the animal subjects along with his scientific input. Matthew Downs, Ph.D. (Postdoctoral Research Scientist, Biomedical Engineering, Columbia University) assisted with the animal preparation and the sonifications while Gesthimani Samiotaki, Ph.D. (Postdoctoral Research Scientist, Biomedical Engineering, Columbia University) assisted with MRI optimization and data processing. Antonios N. Pouliopoulos, Ph.D. (Associate Research Scientist, Biomedical Engineering, Columbia University) worked on the data processing part of the study optimizing the registration

and filtering techniques while Michael Liu, M.S. (Ph.D. student, Radiology, Columbia University) provided great insight and suggestions in the non-linear registration validation and evaluation of the results. Most importantly, the author would like to thank Dr. Sachin Jambawalikar (Assistant Professor of Radiology – Physics, Columbia University) for assisting with the optimization of MRI scanning sequences, data handling, data analysis, mathematical processing, and his overall input in the quantification methods from data acquisition to data analysis.

Chapter 4: Focused ultrasound-facilitated neurotrophic delivery in an early-stage Parkinsonian mouse model.

Establishing in Chapter 3 the normal incidence angle as a predicting factor of the BBB opening volume in the striatum (Caudate nucleus) defined the sonication regime employed herein for transgenic animal models with profound neurodegeneration at the striatal region, among others. The next specific aim and milestone entails the use of the FUS method for neurotrophic factor delivery in the striatum and midbrain of the subacute MPTP (1-methyl-4-phenyl-1,2,3,6-tetrahydropyridine) mouse model, mimicking early stage PD¹⁹.

4.1 Abstract

The BBB prevents most drugs from gaining access to the brain parenchyma, which is a recognized impediment to the treatment of neurodegenerative disorders like Parkinson's disease. FUS, in conjunction with systemically administered microbubbles, opens the BBB locally, reversibly and non-invasively. Herein, we show that neither FUS applied over both the striatum and the ventral midbrain, without neurotrophic factors, nor intravenous administration of neurotrophic factors (either through protein or gene delivery) without FUS, ameliorates the damage to the nigrostriatal dopaminergic pathway in the sub-acute MPTP mouse model of early-stage PD (Figure 17). Conversely, the combination of FUS and intravenous neurotrophic (protein or gene) delivery attenuates the damage to the nigrostriatal dopaminergic pathway, by allowing the entry of these agents into the brain parenchyma. Our findings provide evidence that the application of FUS at the early stages of PD facilitates critical neurotrophic delivery that can curb the rapid progression of neurodegeneration while improving the neuronal function,

seemingly opening new therapeutic avenues for the early treatment of diseases of the central nervous system.

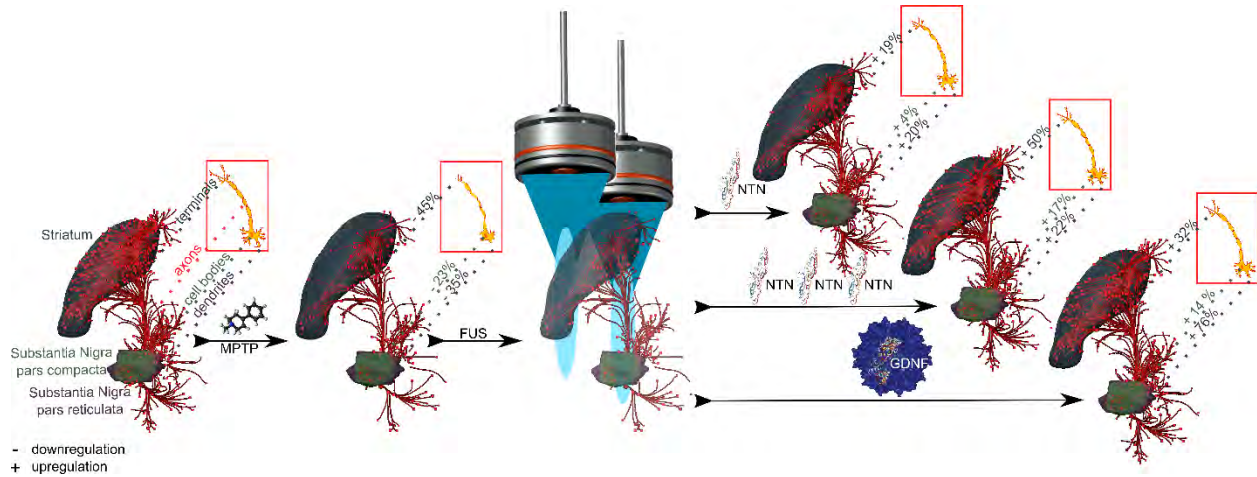


Figure 16: Upregulation of the dopaminergic pathway following focused ultrasound-facilitated drug delivery. The dopaminergic pathway can be downregulated similar to Parkinson’s disease in toxin-based mouse models. Application of focused ultrasound results in increased blood-brain barrier permeability allowing the diffusion of pharmacological agents in the brain. Depending on the number of administrations and the delivery vehicle, the deliverable compounds can have beneficial effects of varying degree.

4.2 Introduction

The BBB poses a hindrance to the treatment of adult-onset neurodegenerative disorders, like PD, preventing most drugs from gaining access to the brain parenchyma. Among the existing drug delivery techniques²⁵ aiming to overcome the BBB, FUS coupled with the administration of microbubbles prevails hence its efficacy profile –non-invasive, targeted, transient.

FUS has been shown to produce a safe disruption of the BBB in various animal species and in experimental models of human diseases. The initiated biological effects are confined to the vessel walls only and contained solely within the targeted region²⁶. Within a certain parametric range, the integrity of the BBB can be restored within hours and remain intact⁹⁴. Single

administration of therapeutic agents alleviating the associated disease symptoms have been proven successful while FUS-mediated gene delivery advantages overcome conventional techniques^{147,187,188}.

The adherence of this chapter on trophic factors in PD stems from the large body of literature showing that neurotrophic factors such as GDNF and NTN can impede the degeneration of the dopaminergic (DA) neurons in the substantia nigra pars compacta, and to restore the function of the injured DA neurons in experimental models of PD^{189–191}. Furthermore, both GDNF and NTN have been tested in humans. Intraputamenal infusion of GDNF resulted in functional improvement in 15 advanced PD patients as reported by two Phase I clinical trials, while the 25% amelioration in motor scores was not achieved in 17 out of the 34 PD patients in a phase II clinical trial. Likewise, intrastriatal delivery of the Adeno-associated type 2 viral vector encoding human NTN (AAV2-NTN) showed preventive effects on MPTP-induced motor disability in non-human primates, but clinical trials failed to show significant disease-modifying effects¹⁹². Despite the negative results of these Phase II studies, which might be due to technical issues^{193–195}, both GDNF and NTN remain quite appealing molecules for the present work given their well-established effects on the DA pathways^{196,197}.

We have previously reported that FUS enhances the delivery of NTN in wild-type mice, non-invasively and locally at the level of PD-relevant brain regions¹¹². Briefly, the area of NTN bioavailability, under the same ultrasound parameters as herein, was $5.07 \pm 0.64 \text{ mm}^2$ in the striatum (designated thereafter caudate-putamen [CPu]) and $2.25 \pm 1.14 \text{ mm}^2$ in the midbrain, showing the presence of NTN across the entire ultrasound-treated brain region compared to the

relatively smaller region reached by direct injection. In this previous work, we also demonstrate that NTN cannot only be delivered successfully to the ventral midbrain through the FUS-induced reversible BBB-opening¹¹², but also that the permeate NTN retains its bioactivity as evidenced by the local activation of the downstream signaling pathway. This finding is particularly significant since the nigrostriatal pathway, which connects the ventral midbrain region with the CPu, is the most severely-affected DA pathway in PD¹⁹.

The response of early stage PD patients to DA stimulation²² raises the question as to whether the targeting of the nigrostriatal pathway by the combined use of ultrasound and neurotrophic factors may be of clinical significance if applied sooner rather than many years after the emergence of PD manifestations. Thus, this study has been specifically designed to address not only the usefulness of FUS in allowing the delivery of BBB-impermeant bioactive molecules, but also whether such combined strategy might be more efficacious in improving the quality of life in patients afflicted by a neurodegenerative disorder, if applied early.

4.3 Materials and Methods

***In vivo* experiments**









All experimental procedures involving animals were approved by the Columbia University Institutional Animal Care and Use Committee. Wild-type C57BL/6 mice (~25 g, ~3 months of age, sex: male, Harlan, Indianapolis, IN, USA) were group-housed under standard conditions (12 hr light/dark cycles, 22°C) and were provided with a standard rodent chow (3 kcal/g; Harlan Laboratories, Indianapolis, IN, USA) and water ad libitum. A total of 70 animals received a daily injection of MPTP (30 mg kg⁻¹ free-base) for five consecutive days; this regimen causes an

apoptotic degeneration of the nigrostriatal pathway in adult mice¹⁹⁸ and by ~21 d after MPTP administration, no further loss of nigral dopaminergic neurons is detected. The groups and the corresponding timeline are summarized in Table II.

Focused ultrasound

A single-element, spherical-segment FUS transducer (center frequency: 1.5 MHz, focal depth: 60 mm, radius: 30 mm; axial full-width half-maximum intensity: 7.5 mm, lateral full-width half-maximum intensity: 1 mm, Imasonic, France), driven by a function generator (Agilent, Palo Alto, CA, USA) through a 50-dB power amplifier (E&I, Rochester, NY, USA) was used to target the SN and the CPu. A central void of the therapeutic transducer held a pulse-echo ultrasound transducer (center frequency: 10 MHz, focal depth: 60 mm, radius 11.2 mm; Olympus NDT, Waltham, MA) used for alignment, with their two foci aligned. The imaging transducer was driven by a pulser-receiver (Olympus, Waltham, MA, USA) connected to a digitizer (Gage Applied Technologies, Inc., Lachine, QC, Canada). A bolus of 0.1 μ L/g of body mass polydisperse manufactured in-house²⁹ microbubbles diluted in saline (8×10^8 #/ mL, mean diameter: 1.4 μ m) was injected intravenously immediately preceding the sonication of each target, i.e. SN or CPu. A 20-min time interval was allowed between SN and CPu targeting to allow the microbubble concentration to be cleared from the circulation¹⁹⁹. Each animal was sonicated for 60 s, with a pulse repetition frequency (PRF) of 10 Hz, with one sonication location at SN and two sonication locations at the CPu in order to safely open the entire area of interest with acoustic parameters that do not cause damage, at peak negative acoustic pressure (PNP) of 0.45 MPa (33, 34) after accounting for 18% and 33% murine skull attenuation for the SN and CPu, respectively.

Table II: Summary of the experimental groups and the procedures undergone.

Groups	MPTP Lesions	Degeneration Interval	Behavioral	BBB Openings	MRI Validation	Injection	Application Interval	Restoration Interval	Behavioral	Staining and Imaging
										
	5 days	21 days	2 days	60 sec/ea	30 min	10 min	14 days	days	2 days	
<i>Phase I</i>										
A n=7	+	+	-	-	+	-	+	14	-	+
B n=7	+	+	-	+	+	-	+	14	-	+
C n=7	+	+	-	+	+	NTN	+	14	-	+
D n=5	+	+	-	-	+++	-	+++	14	-	+
E n=5	+	+	-	+++	+++	-	+++	14	-	+
F n=5	+	+	-	+++	+++	NTN	+++	14	-	+
<i>Phase II</i>										
G n=8	+	+	+	-	+		+	70	+	+
H n=8	+	+	+	-	+	AAV ₁ -GDNF	+	70	+	+
I n=8	+	+	+	+	+		+	70	+	+
J n=10	+	+	+	+	+	AAV ₁ -GDNF	+	70	+	+

Magnetic resonance imaging

MRI was performed on mice receiving sonications. Upon completion of the ultrasound procedures, the BBB opening was confirmed with a 9.4T MRI system (Bruker Medical, Boston, MA). The mice were placed in a birdcage coil (diameter 35 mm), while being anesthetized with 1 – 2% isoflurane and respiration rate was monitored throughout the imaging sessions. MR images were acquired using a contrast-enhanced T1-weighted 2D FLASH sequence (TR/TE 230/3.3ms, flip angle: 70°, number of excitations: 6, field of view: 25.6mm × 25.6mm, resolution 100 μm x 100 μm x 400 μm), 30 minutes following the intraperitoneal bolus injection of 0.3 ml gadodiamide (GD-DTPA) (Omniscan, GE Healthcare, Princeton, NJ). As previously reported, gadodiamide provides spatial information of the BBB opening by temporally enhancing the MR signal relative to the ultrasound parameters³⁷. In addition, T2-weighted MRI was performed one

day after the sonication to detect any potential damage using a 2D RARE sequence (TR/TE 2500/10 ms/ms, echo train: 8, number of excitations: 8, field of view: 25.6mm × 25.6mm, resolution 100 μm x 100 μm x 400 μm). The sequences employed in this study have been previously optimized by our group⁹⁴.

Simulation

The acoustic properties of the mouse head were obtained from microCT images with a resolution of 80 μm in the three directions (R_mCT2, Rigaku, Tokyo, Japan). The acoustic properties of the skull and the brain were obtained from previously published experimental data (35). The numerical simulations were performed using the k-Wave MATLAB (MathWorks Inc., Natick, MA, USA) toolbox²⁰⁰. The toolbox provides the k-space pseudo spectral time domain solution for the coupled first-order acoustic equations for heterogeneous media. The detailed explanation of simulation parameters can be found in our previous report²⁰¹.

Neurotrophic Factors

Recombinant human Neurturin was purchased from Invitrogen (CA, USA) and reconstituted according to the manufacturer's instructions. An intravenous injection of 50μl Neurturin (20 μg/g of body mass) followed immediately after the FUS-induced BBB opening for which 5 μl/mouse microbubbles were diluted in 100μl saline and injected via the tail vein.

The AAV1-CAG-eGFP-GDNF vectors used in this study were purchased from SignaGen Laboratories (Rockville, MD). The titers of the viral vectors were provided by the manufacturer (quantified with real-time PCR) and diluted to 1.2×10^{12} GC/ml in PBS. For each mouse (average

body weight of 25 g), a total of 100 μ l diluted AAV was mixed with approximately 5 μ l/mouse microbubbles and co-injected via the tail vein.

AAV Transduction

The mice were sacrificed and the brains processed similar to the previous description but, the sections were treated with rabbit anti-GFP antibody (dilution 1:5000, Novus Biologicals, Littleton, CO) and goat anti-rabbit conjugated with Alexa Fluor 488 (dilution 1:500, ThermoFisher, Waltham, MA) to confirm AAV transduction. Fluorescence images were taken with a confocal microscope (Nikon Instruments Inc., Melville, NY).

Immunohistochemistry

Mice were subjected to transcardial perfusion upon sacrifice and the brains extracted and sectioned (30 μ m) throughout the entire CPu and SN as previously described¹⁶⁹. Every 6th section of the posterior CPu and SN, and every 6th section of the anterior CPu were processed free-floating for TH-immunohistochemistry. After these sections were sequentially washed in 0.1 M tris-buffered saline (TBS), treated with 10% methanol/3% H₂O₂ solution in TBS, rewashed in TBS, incubated for 60 min in 5% normal goat serum (NGS, Vector, USA), and then incubated for 49 h with an anti-TH antibody (Calbiochem, USA, 1:2000 for SN; 1:1000 for CPu) at 4°C in TBS containing 2% NGS. Then, sections were washed in TBS, followed by incubation for 60 min with a secondary biotin-conjugated anti-rabbit antibody raised in goat (1:400 in TBS), washed again in TBS, incubated for 60 min in an avidin-biotin complex solution (ABC HRP kit (Peroxidase, Goat IgG), Vector Laboratories, USA) in TBS, and then washed in TBS. Finally, immunostaining was visualized by 3,3'-diaminobenzidine (DAB substrate kit, Vector Labs) and all

sections were counter-stained with cresyl violet solution (1 g cresyl violet acetate, Sigma-Aldrich, USA, in 500 mL DI-water with 25 mL acetic acid 10%).

Real-time PCR

Real-time PCR was used to quantify copies of GFP mRNA in various brain regions. Ten days after FUS-facilitated AAV delivery, mice were sacrificed and brain structures (striatum and substantia nigra) were isolated. The primers used in this study were forward (5'-AGCTGAAGGGCATCGACTTC-3') and reverse (5'-CTACGGCTACCTTGTTACGA-3'). The analysis was performed with a RNeasy Plus Mini Kit (Qiagen, Hilden, Germany). The mRNA levels were measured by qPCR using the SYBR Green assay (Applied Biosystems, Carlsbad, CA, USA). Signals from structures of interest were compared to signals from background tissue (cerebellum) and fold changes were obtained.

High-performance Liquid Chromatography (HPLC)

HPLC with electrochemical detection was employed to quantify the levels of dopamine, DOPAC and HVA. Following the same timeline for single NTN administration, mice (3-5 per group) were decapitated, their brains were quickly removed, hemispheres were separated and the corresponding sections (striatum and midbrain) were dissected out freehand on an ice-chilled glass petri dish. Samples were immediately frozen on dry ice and stored at -80°C until analysis. On the day of the assay, the samples were sonicated in 50 vol (wt/vol) of HeGA while on ice. Centrifugation at 10,000 x g at 4°C for 10 minutes was followed by filtering and injection of the supernatant (20µl) onto a C18-reverse-phase HR-80 catecholamine column (ESA, Bedford, MA). The samples passed through a mobile phase of 90% 50 mM sodium phosphate/0.2 mM

EDTA/1.2 mM heptanesulfonic acid (pH = 3.5) solution and 10% methanol with a 1.0 ml/min flow rate. Peaks were detected by an ESA model Coulochem 5100A detector (E1 = -0.04 V, E2 = +0.35 V).

Quantitative Morphology

The total number of TH- and cresyl violet-stained SNpc neurons were counted by Stereology using the optical fractionator as per the published protocols^{202,203}. To quantify the immunoreactivity of TH+ nerve fibers in the SNpr, midbrain tissue sections were white-balanced, and color deconvoluted^{112,204} prior to being converted to grayscale. Then, the SNpr was manually outlined, and the pixels within this region of interest were thresholded. The percentage of the dendrites/axons-covered area on each side, i.e. ipsilateral and contralateral to FUS, was determined and the average ratio of each group was used to compare the results among the different groups. The same quantification algorithm was followed for the TH+ expression in the CPu images without the deconvolution step since the striatum slices were not counterstained.

Stereology

Estimates of the number of TH+ neurons in the SNpc were generated by first delineating the borders of the SNpc with a 5× objective using the anatomical landmarks specified in the literature^{205,206}. The number of SNpc TH+ (DA) neurons was then calculated using the optical fractionator probe (Stereoinvestigator, version 11.02.1, MBF Bioscience, Williston, VT, USA). By applying a random start and random distribution of the counting frames, every 4th section was counted (for a total of ~10 sections per mouse) with an unbiased counting frame size of 100 × 100 μm and a grid size of 200 × 200 μm. Cells were sampled through the entire thickness of

the tissue section using a 1 μm guard zone. Sections were viewed under a 40 \times dry objective. At least 100 cells were counted within 40–60 framing sites for each side and animal, and the coefficient of error was ≤ 0.10 .

Behavioral Study

Amphetamine-elicited behavioral studies were performed for the neurorestoration part of the experiments. Four weeks after MPTP lesioning, mice were randomly assigned to four groups. Each mouse received an intraperitoneal injection of amphetamine (2.5 mg/kg, dissolved in 150 μl saline) 10 min before behavioral testing. The subject was then placed in an open field chamber consisting of a custom-made polycarbonate chamber (dimensions: 27.3 cm x 27.3 cm x 27.3 cm). Directly above the chamber was a video camera, which interfaced with a computer and tracking software (Noldus, Wageningen, Netherlands). Each subject was placed directly in the center of the field, and video tracking was used to record and measure activity. Mice explored the field ad libitum for a session duration of 40 minutes. Upon completion, the subject was removed, urine and feces were counted and removed, and the chamber was cleaned with ethyl alcohol and disinfectants to remove any trace of the former subject. The same behavior testing was repeated for each animal post AAV/FUS treatment at the end of the 12-week survival period.

Statistical Analysis

Intra-group comparisons between the ipsilateral and contralateral sides were analyzed using a two-tailed paired Student's t-test. All values are expressed as means \pm standard deviation. Differences among group means were analyzed using two-way factorial analysis of variance (ANOVA) with AAV and FUS as the independent factors. When ANOVA showed significant

differences, pair-wise comparisons between means, post-hoc analysis by Newman-Keuls multiple comparisons test was performed. In all analyses, the null hypothesis was rejected at the 0.05 level. All statistical analyses were performed using Prism 7 (Graphpad Software, San Diego, CA, USA).

4.4 Results and Discussion

To determine the potential value of using FUS to improve brain penetrance of bioactive molecules, especially those promoting functionality, if not viability, of the compromised neurons in certain regions of the neurodegenerated brain, we elected to use the MPTP mouse model of PD¹⁹. More precisely, not only does this neurotoxin-based model provide, in mice, reliable, extensively-validated lesioning of specifically the nigrostriatal DA pathway, but also causes, in humans, a clinical picture almost indistinguishable from PD²¹, hence strengthening the relevance of the anticipated mouse findings to the human condition. It should also be emphasized that most effective preclinical neuroprotective strategies tested in animal models of PD, while mitigating neurodegeneration, fail to maintain DA function²⁰⁷, hence often ending with a number of SNpc neurons unable to produce DA. Thus, the importance of identifying adjunct strategies that are capable of improving function in spared DA neurons is critical to the success of neuroprotective/neurorestorative strategies. Accordingly, our preclinical experiments were designed to be specifically relevant to this important clinical issue by using, primarily, TH-immunostaining and quantitative morphology in the nigrostriatal DA pathway of mice post-MPTP as a proxy for FUS allowing NTN and GDNF to reach and to operate within the CNS. This strategy was prompted by the fact that many spared DA neurons in the MPTP model have

subnormal expression of TH, the rate-limiting enzyme in DA synthesis, and that neurotrophic factors have the property of stimulating TH expression.

For the present study, the workflow focused on the morphological quantification of cell bodies, dendrites and nerve terminals of the nigrostriatal DA pathway. Our experimental design compared TH-based parameters between hemispheres among MPTP-injected mice that received either no, one or three systemic injections of NTN combined with either one or three unilateral brain FUS exposures or a single gene delivery of AAV-GDNF; throughout this study, the ipsilateral hemisphere refers to the hemisphere receiving the unilateral ultrasound. Previously, we used a similar design in intact mice and found that the application of unilateral brain FUS following a systemic injection of another trophic factor, BDNF, did promote its entry into the brain, only in the ipsilateral hemisphere and in a highly regionally restricted manner⁷⁰. In a similar rationale, the successful delivery of NTN through the FUS-induced BBB opening in wild type mice has been confirmed by tracing the downstream signaling pathway through the detection of increased phosphorylation of the Ret receptor, cytoplasmic kinase Erk 1 and 2 and CREB transcription factor in structures associated with their abundance¹¹². Also, for the purpose of this study, the neurotrophic factors are assumed to be of equivalent efficacy when it comes to neurorestoration and neuroprotection as previously reported^{208,209}.

As we have previously demonstrated²¹⁰, the regimen of MPTP used here in adult mice not only causes a loss of TH-positive cell bodies in the SNpc, but also, and to a greater extent, of TH-positive dendrites in the substantia nigra pars reticulata (SNpr) and nerve terminals in the CPu

(Figure 18). Mice that were subjected to this subacute regimen of MPTP conformed to the

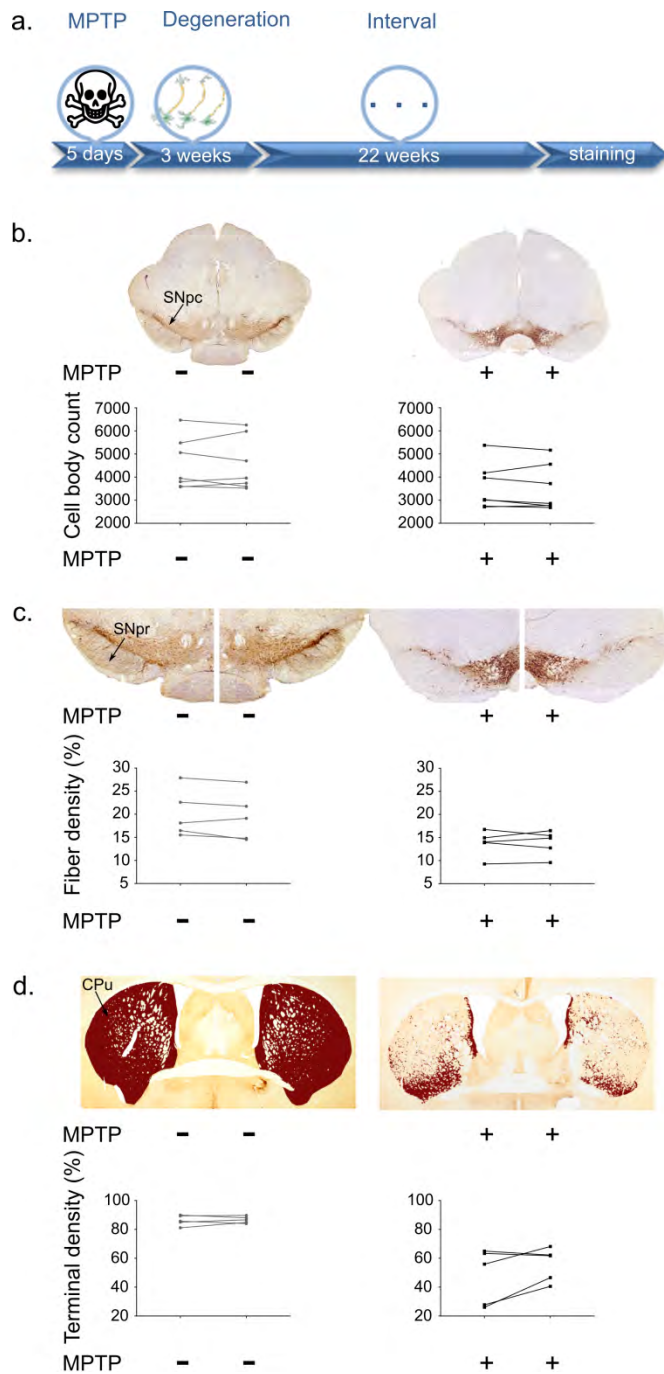


Figure 17: The MPTP effect. a. The timeline shows degeneration following MPTP application and the interval until immunohistochemistry was performed. b. Representative coronal images of the SNc for control and MPTP injected groups. SNc cell body quantification for each brain hemisphere is presented. A ~22% reduction of SNc TH+ cell body number is observed in the MPTP- vs saline-injected mice (two-way ANOVA for $n=7$, $F[1, 12] = 3.191$; $P=0.0993$). c. Higher magnification (4x) images focusing on the SNr shows a loss of fibers of ~33% in MPTP- vs. saline-injected mice (two-way ANOVA for $n=5$, $F[1,$

8] = 5.335; P=0.0497). The area quantification is presented per hemisphere and per brain. d. Representative images of the CPu TH+ terminal density for the saline and MPTP groups showing a ~40% reduction of CPu TH+ immunoreactivity in MPTP- vs saline-injected mice (two-way ANOVA for n=5, F[1, 8] = 25.64; P=0.0010). Area quantification shows the decrease in TH+ immunoreactivity for the MPTP mice per side per brain.

known description of the aforementioned brain lesion. However, based on our past experience²¹⁰, we specifically set the dosage of MPTP per injection to cause a detectable but minimal reduction in TH-positive neurons in the SNpc so that we could predict a 40-50% reduction in TH-immunoreactivity in the CPu. This approach was selected since goal for this work was to closely emulate an early stage of PD¹⁹. Indeed, the ultimate objective of the proposed methodology would be for application in early stage PD patients who may experience a particularly strong quality of life improvement, should the proposed therapeutic strategy effectively boost the expression of DA synthetic enzymes, such as TH, in compromised, but still alive SNpc neurons. As expected, our stereology counts revealed a ~23% reduction of SNpc TH-positive neurons in mice injected with MPTP compared to those injected with saline (two-way ANOVA for n=7, F[1, 12] = 3.191; P=0.0993). To assess the effect of MPTP in the SNpr and CPu, we used a customized TH density quantification algorithm based on thresholding. Images were white-corrected and color-deconvoluted before delineating the SNpr or the CPu as the ROIs. The percentages of pixels over the ROIs that exceeded the set intensity threshold for both MPTP- and saline-injected mice are presented for both hemispheres separately. Based on this method, we found that MPTP-injected mice displayed a ~35% and ~45% reduction of TH-immunoreactivity in the SNpr (two-way ANOVA for n=5, F[1, 8] = 5.335; P=0.0497) and CPu (two-way ANOVA for n=5, F[1, 8] = 25.64; P=0.0010), respectively (Figure 18). Furthermore, neither in the MPTP-treated (pair Student's t-test; SNpc: t[6]=0.821, p=0.442; SNpr: t[4]=0.07, p=0.947; CPu: t[4]=1.832, p=0.14) nor in the saline-administered mice (pair Student's t-test; SNpc: t[6]=0.217, p=0.835; SNpr: t[4]=1.447, p=0.221; CPu: t[4]=0.426, p=0.691) did the DA parameters differ

significantly between the two hemispheres, excluding TH-immunoreactivity asymmetry. The significant loss of cells bodies, dendrites and terminals in the MPTP brains was also noted by the decreased TH immunoreactivity compared to the saline group.

Having established the damage caused in the three selected brain regions, i.e. SNpc, SNpr, and CPu by the MPTP injections, we then investigated the effects of the combination of a unilateral brain FUS application with the systemic administration of NTN on DA parameters in MPTP mice.

Given the lack of right-left DA asymmetry in the MPTP mice reported above and the fact that FUS is applied only on one side of the brain, our results were computed as ratios of ipsilateral over contralateral values to better capture the unilateral nature of the proposed strategies.

Since the cell bodies of the nigrostriatal DA neurons reside in the SNpc, assessment of the effect of FUS/NTN in this specific brain region was first performed in order to understand the potential effect of our methodology on a stable lesion, i.e. fixed number of neurons. Indeed, at the selected time point, it has been demonstrated previously that DA neurons no longer die²¹¹. Since no compelling evidence of DA neurogenesis in the post-lesioned adult brain exists²¹², any change in the number of TH-positive neurons could only be attributed to a larger number of “countable neurons” due to increased TH immunoreactivity. This phenomenon, thus, works as a proxy for NTN action. Two descriptive timelines show the steps followed during the experimental procedure for the single and triple treatment separately, along with the representative TH-immunostained tissue sections (Figure 19). A one-way ANOVA for the five groups of MPTP-

injected mice, i.e. FUS-/NTN-, FUS+/NTN-, FUS+++/NTN-, FUS+/NTN+, and

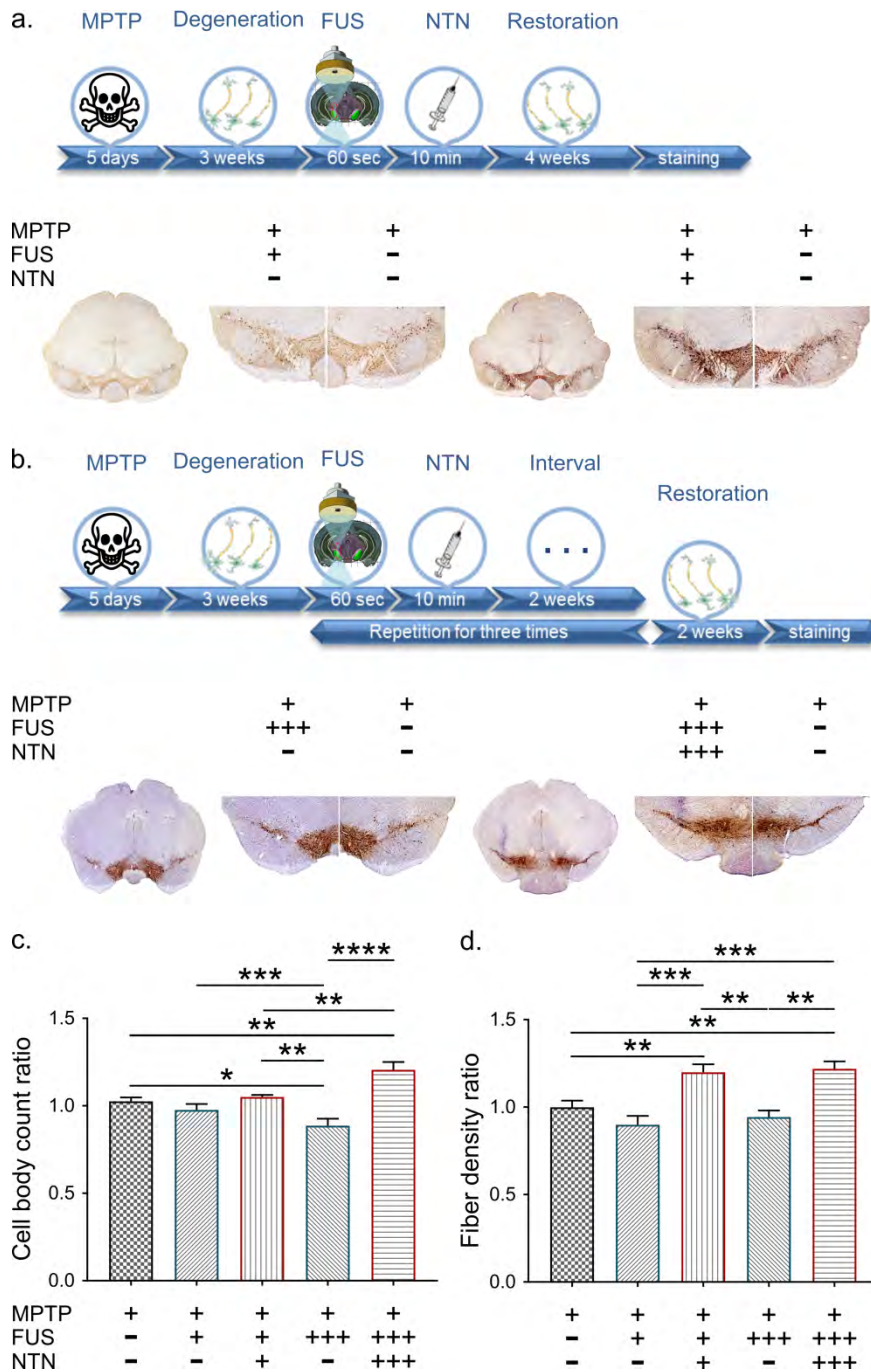


Figure 18: Neurorestoration effect at the level of the SN. a. Single treatment at the SN: The descriptive timeline of the procedure is followed by representative TH immunohistochemistry images. The plus/minus signs indicate whether the corresponding side of the brain received MPTP, FUS and NTN. b. Triple treatment at the level of the SN: The corresponding timeline provides information regarding the additional steps followed for this part of the study. The plus/minus signs indicate whether the brains received MPTP, FUS and NTN and the three plus signs denote the times the treatment was repeated. c. Cell

body counts at the level of the SNc region. Results are shown as the relative ratio by dividing the contralateral side into the ipsilateral side. The statistical significance occurs with one-way ANOVA ($n=5-7$; $F[4, 27] = 8.892$; $P=0.0001$) after correcting the multiple measurements with Newman-Keuls method. d. The area quantification of the fibrotic density at the SNr region. The results are shown as the relative ratio by dividing the contralateral side into the ipsilateral side. The statistical significance occurs with one-way ANOVA ($n=5-7$; $F[4, 22] = 11.31$; $P<0.0001$) after correcting the multiple measurements with Newman-Keuls method.

FUS+++/NTN+++ revealed significant differences in SNpc TH-positive neuron numbers ($n=5-7$; $F[4, 27] = 8.892$; $P=0.0001$). By using Newman-Keuls post-hoc tests, we found that either one or three FUS applications to MPTP mice alone failed to significantly increase TH-positive SNpc neuron numbers compared to no FUS ($P>0.05$). Conversely, administration of three, but not one, NTN administrations, each time preceded by FUS application, resulted in a significant increase ($p<0.01$) on the order of 17%. Thus, these findings indicate that systemic NTN successfully gained access to the CNS following FUS application and initiated the upregulation of TH expression within the spared SNpc DA neurons. Although these results are encouraging, from a functional standpoint, it remains to be investigated whether similar changes occurred where DA neurotransmission actually takes place.

One unique property of SNpc DA neurons is the capacity to release DA from their dendrites, suggesting that DA mediates neurotransmission events not only at the level of the CPu but also at the level of the SNpr. Thus, to address the effect of NTN in the SNpr region, the threshold area covered by TH-positive fibers exceeding the stain-intensity cut-off was extracted and normalized to the entire region covered by fibers. As for the SNpc, a one-way ANOVA revealed significant differences in SNpr TH-positive fiber density among the five groups ($F[4, 22] = 11.31$; $P<0.0001$) as shown in Figure 19. As was the case with the cell bodies, the Newman-Keuls post-hoc test demonstrated that neither one nor three FUS applications alone to MPTP mice produced

any positive changes in SNpr fiber density. In contrast, both single and triple administration of NTN, after the corresponding applications of FUS, resulted in a statistically significant increase of the SNpr TH-positive dendritic network on the order of 20-22% compared to the no FUS group. The higher TH-immunoreactivity observed within the SNpr in response to FUS/NTN treatment supports the notion that dendritic expression of DA markers in spared neurons post-MPTP can be increased.

Furthermore, given that TH is the rate-limiting enzyme in DA synthesis, our results support the fact that the combination of NTN and FUS may help to enhance DA neurotransmission in compromised neurons. Interestingly, if enhanced DA neurotransmission within the SNpr can be associated with comparable changes in the CPu, the proposed therapeutic strategy may have far-reaching implications for the symptomatic treatment of PD. It is also worth noting that since the magnitude of the changes was not significantly different in MPTP-injected mice that received one or three FUS/NTN treatments, it may be argued that, with respect to SNpr, the maximal induction of TH in the DA dendrites is already achieved after a single FUS/NTN exposure. However, from the perspective of a chronic condition like PD, future studies will have to investigate the duration of the dendritic induction of TH produced by one and three FUS/NTN exposures and assess the recurrence of the treatment, as this question may be of major importance in determining the optimal FUS/NTN regimen for PD patients.

Anatomically, SNc DA neurons project primarily to the CPu¹⁹, hence the loss of SNpc DA neurons in PD causes a striatal depletion of DA nerve terminals and DA content. To determine

the efficacy of our technique in promoting nerve terminal function, we estimated CPu fiber

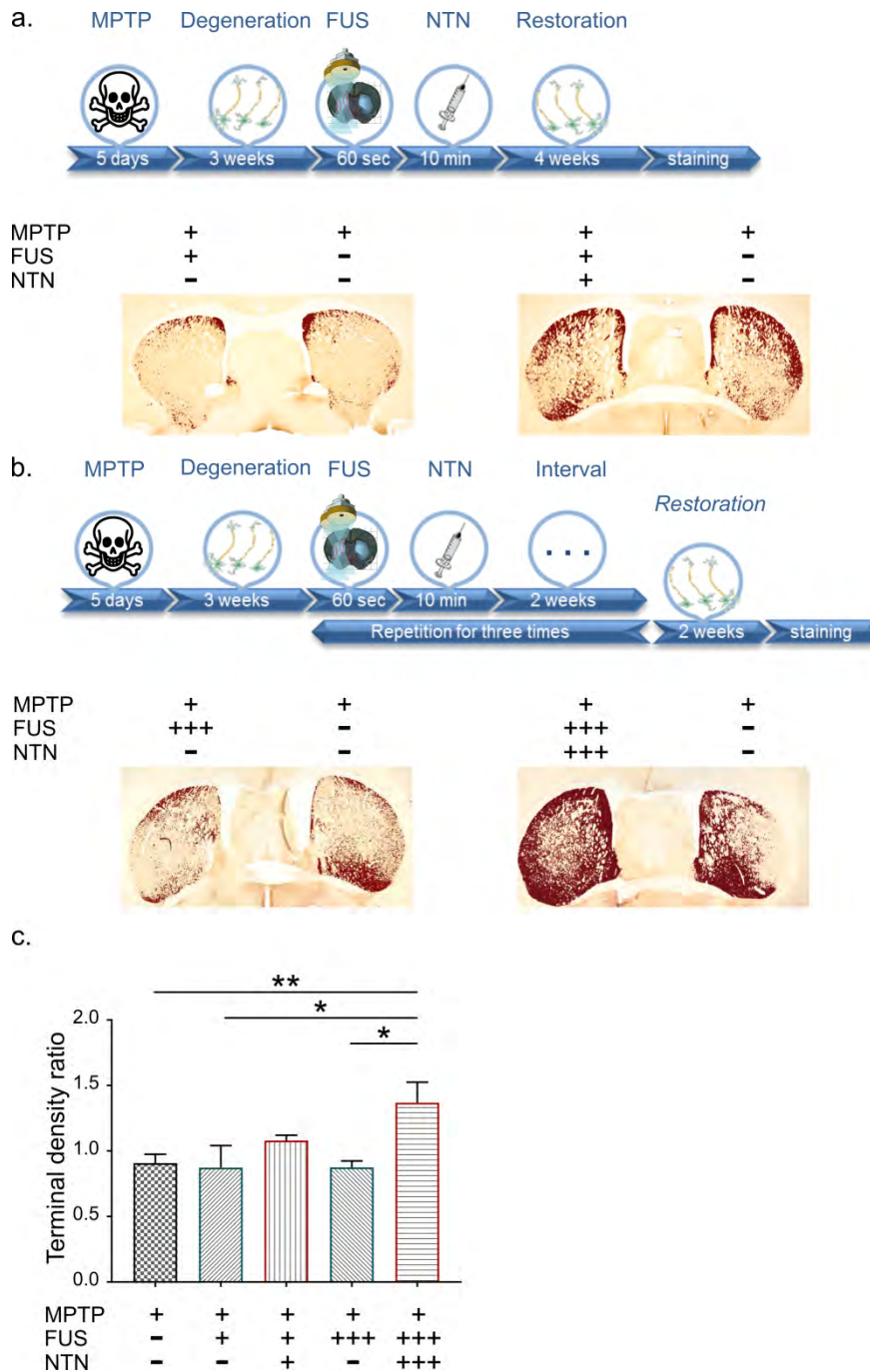


Figure 19: Neurorestoration effect at the Caudate-Putamen (CPu) region. a. The descriptive timeline of the procedure is followed by representative TH immunohistochemistry images. The pixels surpassing a certain threshold are presented in dark red to enhance the differences between the ipsilateral and contralateral side. The plus/minus signs indicate whether the corresponding side of the brain received MPTP, FUS and NTN. **b.** Triple treatment at the CPu: The corresponding timeline provides information regarding the additional steps followed for this part of the study. The

plus/minus signs indicate whether the brains received MPTP, FUS and NTN and the three plus signs denote the number of times the treatment was repeated. c. The area quantification of the terminal density at the CPu region. Results are shown as the relative ratio by dividing the contralateral side into the ipsilateral side. The statistical significance occurs with one-way ANOVA ($n=5-7$; $F[4, 24] = 3.527$; $P=0.0212$) after correcting the multiple measurements with Newman-Keuls method permeate the CPu as effectively as in the SNr, it may be that the stronger regimen of FUS/NTN is required to achieve the desired effect. Furthermore, within the CPu, TH-positive fibers represent less than 10% of the fiber pool hence, most of the NTN molecules in the CPu might interact with neuronal structures other than TH-positive fibers.

density by quantifying its TH immunoreactivity employing the same algorithm as for the SNpr site. Figure 20 shows the respective timelines with the sonicated structure as well as representative images for each group. Again, we performed a one-way ANOVA which revealed significant differences in the CPu TH-positive fiber density among the five groups ($n=5-7$; $F[4, 24] = 3.527$; $P=0.0212$). As expected, from the preceding analysis of the SN regions, FUS alone did not result in an increase of the terminal TH positivity. In striking contrast to the situation observed in the SNpr, only the three FUS/NTN exposures caused an overt increase in TH immunoreactivity in the CPu of the MPTP mice ($p<0.05$) on the order of 50%. Since the single administration of NTN failed to permeate the CPu as effectively as in the SNpr, the stronger regimen of FUS/NTN may be required to achieve the desired effect. Furthermore, within the CPu, TH-positive fibers represent less than 10% of the fiber pool hence, most of the NTN molecules in the CPu might interact with neuronal structures other than TH-positive fibers. To complement these immunohistochemical findings, the levels of DA and its metabolites, homovanillic acid (HVA) and 3,4-dihydroxyphenylacetic acid (DOPAC) were determined by HPLC in both the ventral midbrain and striatum. The results are reported as ratios of ipsilateral over contralateral levels to capture the unilateral effect of our intervention. A significant twofold increase in DA levels was observed in the ventral midbrain ($F_{[3, 13]} = 7.055$; $P=0.0047$) and to a lesser extend in the CPu of hemispheres treated once with ultrasound and NTN compared to the

rest. The levels of the key metabolites followed the same trend, even though these changes in metabolites were not statistically significant. These HPLC findings are in agreement with the TH immunoreactivity proving the insufficiency of the single treatment in restoring the depleted DA to its original levels.

The decrease in TH immunoreactivity observed in MPTP-injected mice treated with ultrasound alone (FUS+/NTN- and FUS+++/-NTN-) in Figures 19 and 20 raised the possibility that FUS might downregulate TH expression. To test this possibility, naïve mice (i.e. not injected with MPTP) were subjected to FUS. For this experiment, five mice sonicated multiple times (MPTP-/FUS+++/-NTN-) and five mice sonicated only once (MPTP-/FUS+/NTN-) were compared against five control mice (MPTP-/FUS-/-NTN-); for the three sonications protocol, two days interval was used between each sonication to allow the BBB to be restored⁹⁴. Remarkably, the number of SNpc TH-positive neurons did not significantly differ among the three groups (one-way ANOVA, $F[2, 12] = 1.755$; $P=0.2145$). Similarly, no significant differences were observed in either the SNpr TH-positive dendrite (one-way ANOVA, $F[2, 12] = 0.1158$; $P=0.8917$) or CPu TH-positive terminal density (one way ANOVA, $F[2, 12] = 0.1193$; $P=0.8886$) across the three groups. Although FUS does not cause any detectable alteration in TH expression in healthy neurons, it remains an open question whether ultrasound could downregulate TH expression in compromised neurons.

To determine whether dopaminergic restorative effects could be produced by the combination of AAV-GDNF and FUS in the early stages of PD, a new cohort of mice was used and the different

treatments (FUS-/AAV-, FUS+/AAV-, FUS-/AAV+, FUS+/AAV+) were compared 84 days after the delivery (Figure 21a).

The viral vector used in this study was AAV1 under the control of the neuron-specific CAG promotor. Different from AAV9, a more aggressive serotype, AAV1 does not cross the BBB spontaneously, and yet maintaining a higher level of bioactivity compared to that of AAV2. Our previous work has shown that greater transduction can be achieved using this serotype compared to AAV2⁷⁶, which has been the sole choice for all clinical PD trials to date²¹³. The CAG promotor was selected to best represent the vector used in prior clinical trials. In this study, we observed some degree of non-specific transductions in untargeted organs, such as the liver and kidney similar to neuron-specific promotor synapsin^{213,214}.

Upon sacrifice, immunohistochemistry revealed stronger TH immunopositivity at the level of the ventral midbrain sections of MPTP mice receiving AAV+/FUS+ combinations, on the sonicated side, than at the level of ventral midbrain sections of mice from all other MPTP groups (Figure 21b). Quantitatively, TH-positive neuron numbers did not significantly differ (paired Student's t-test; $t[7] \leq 0.45$, $p \geq 0.67$) in mice that received neither or one form of treatment (i.e. AAV or FUS) as shown in Figure 21c. However, while marginal, MPTP mice that received systemic AAV-GDNF injection and unilateral sonication showed, on average, a greater number of SN TH-positive neuron numbers on the sonicated side (paired Student's t-test; $t[11] = 2.93$, $p = 0.015$). Even more striking is the observation that MPTP mice from the AAV+/FUS+ group showed, on the sonicated side, quite a stronger SN pars reticulata optical density of TH immunostaining (Figure 21d and 21e) (paired Student's t-test; $t[4] = 7.01$, $p = 0.006$), suggesting

that the combination of AAV-GDNF and FUS has a strong beneficial effect on dopaminergic

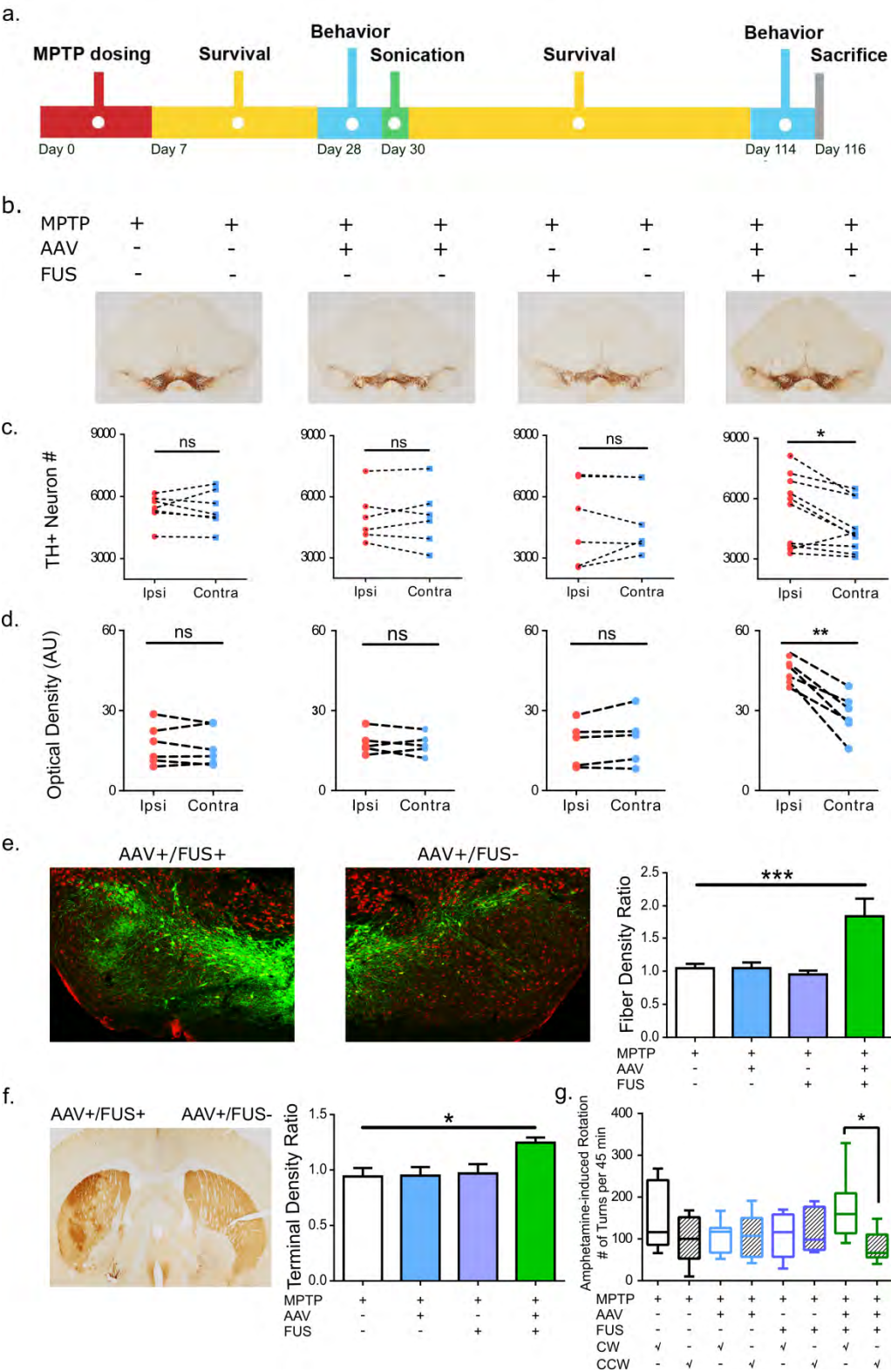


Figure 20: FUS-facilitated AAV-GDNF delivery induced neuronal upregulation in MPTP mice. a. Experimental timeline where MPTP was given first followed by sonication and a 12-week survival period. Behavioral studies were performed 1 week prior to sonication and repeated at the end of the survival period. b. TH staining of the SN region in mice receiving a combination of AAV/FUS treatments (n=6-10). c. TH+ neurons were counted and intra-group comparisons were made. Significantly higher number of TH+ neurons were found on the AAV+/FUS+ side of the brain compared to the contralateral side. d. TH+ dendrite density was calculated and intra-group comparisons were performed. Significantly higher dendrite density was observed on the AAV+/FUS+ side of the brain. e. Immunofluorescent TH staining revealed much more dopaminergic projections on the AAV+/FUS+ side of the brain. Dendritic densities of the SN region were compared across groups and significantly higher dendritic fiber network (n=4-5; $F[3, 13] = 7.514$; $P=0.0036$) was identified comparing AAV+/FUS+ to the MPTP group. f. TH staining of the striatum illustrates the ameliorated dopaminergic projections on the AAV+/FUS+ hemisphere. Quantitative analysis of the optical density ratio demonstrated significant difference (n=4-5; $F[3, 17] = 4.733$; $P=0.014$) between the AAV+/FUS+ to the MPTP group. g. Amphetamine-elicited behavioral studies revealed more frequent clockwise (toward the remaining lesion side) rotation, signifying more prominent dopaminergic function on the hemisphere receiving AAV+/FUS+ treatment.

dendrites. Across group comparison revealed a significant increase (n=4-5; $F[3, 13] = 7.514$; $P=0.0036$) on the order of 76% in the dendritic fiber network of the ipsilateral-over-contralateral side compared to the MPTP group (Figure 21e). A very similar situation was observed for the ratio of the striatal TH-positive terminal density which was significantly higher (n=4-5; $F[3, 17] = 4.733$; $P=0.014$) on the order to 32% for the AAV+/FUS+ group compared to the MPTP-injected mice (Figure 21f).

To provide a functional correlate to the above results, we took advantage of the fact that amphetamine, by stimulating the release of dopamine from the residual neurons, induces a rotational behavior in rodents if there is a right/left unbalance²¹⁵. Using a camera-based behavioral testing apparatus, mice were allowed to explore the field freely and the number of clockwise (CW; i.e. away from the sonicated hemisphere) and counter-clockwise rotations (CCW; toward the sonicated hemisphere) were recorded after amphetamine injection. After MPTP injection but prior to any AAV and/or FUS treatment, no significant rotational behavioral

was noted in any of the mice indicating that the MPTP lesion produced symmetrical damage. Twelve weeks after the AAV and/or FUS treatment, only the MPTP mice from the AAV+/FUS+ group showed significant rotations that were consistently CW (paired Student's t-test; $t[8] = 2.61$, $p = 0.035$), supporting the notion that the sonicated side was associated with higher amphetamine-induced dopaminergic neurostimulation (Figure 21h).

The AAV+/FUS+- treated mice had significantly higher optical densities for both the dendritic field in the SN pars reticulata and the nerve terminal network in the CPu, on the sonicated side as well as a marginal increase in SN TH-positive neurons on the sonicated side. Since no compelling evidence exists, supporting that novel dopaminergic neurons can be produced in mature brains²⁰⁷, the most parsimonious explanation for the AAV/FUS-related changes in neuronal counts is that the combined treatment stimulates the expression of TH, causing merely more dopaminergic neurons to become identifiable and counted. Although this explanation can also apply to the dendritic field changes, we cannot exclude that the nerve terminal changes are, at least, due to axonal sprouting. While more work is required to elucidate the underpinning process driving the aforementioned changes, we already know that they are functionally relevant since, following amphetamine injection, the MPTP mice post-treated with AAV/FUS display a robust rotational behavior consistent with the idea that the sonicated side that received AAV-GDNF recovered a strong dopaminergic neurotransmission²¹⁵.

The therapeutic alternatives explored in this study showed a gradual increase in beneficial outcome. Direct protein delivery was proven efficient in upregulating neuronal function but its translation to the clinical practice entails multiple applications that significantly improve

neuronal integrity along the entire pathway. Gene therapy comes as an alternative to multiple applications allowing for constant release of the neurotrophic factor with only one ultrasound session. The successful delivery was followed not only by upregulation of the dopaminergic pathway including a small increase in neuronal cells but also by a detectable behavioral effect enhanced by the administration of amphetamine.

4.5 Limitations and Conclusions

One limitation of this study is that FUS could induce acute inflammation in the sonicated region⁵³. This is likely caused by the exudates (such as albumin) through the opened BBB leading to microglia upregulation. However, as shown in our previously reported studies, this does not lead to long-term inflammation nor behavior deficits⁷⁶. The amount of administered viral vectors should also be carefully examined to minimize systemic toxicity and immune response. Studies in larger animal models (i.e. non-human primates) need to be carried out before results presented here can be translated to the clinic.

Other limitations in this study include the limited number of mice used primarily due to the high cost of NTN acquisition. As a consequence, additional quantitative measures to directly measure DA synthesis such as analytical techniques could not be fully explored but will be included in future studies. Moreover, different dosages, upregulation duration as well as the time-interval between consecutive treatments also could not be studied. Multiple treatments may have an even more profound restorative effect, if applied at the steady state of the preceding treatment. The two major obstacles involved in NTN delivery to the brain with efficient dosage lie in, first, permeating the BBB and, second, ensuring sufficient bioavailability across the entire structure of

interest. In the study preceding this one¹⁹², it was shown that both objectives could be achieved with FUS-induced BBB drug delivery in wild-type mice.

In conclusion, for the first time, our findings show that by targeting the SN and CPu at the early stages of PD, the nigrostriatal pathway is upregulated, thus reinforcing the strong premise of FUS methodology for allowing otherwise BBB-impermeant bioactive molecules to reach the brain parenchyma and treat the compromised neurons. Administration of neurotrophic factors achieved significant increase in the DA phenotypic marker TH that was localized at the level of the downregulated nigrostriatal pathway. Gene therapy and the triple treatment improved neuronal function at both the dendritic and terminal area while the single treatment only upregulated the former.

This study employed direct delivery of neurotrophic proteins as the pharmacological strategy, therefore substituting gene delivery and the associated risks. On the other hand, gene delivery was proven safe and beneficial to the treated brains accounting as a viable alternative to the difficulties associated with multiple treatments. The AAV-GDNF delivery offered the opportunity of investigating physiological changes due to the continuous production of the neurotrophic factor and the longer survival times constituting the second part of this study. Based on these initial findings, FUS-mediated neurotrophic protein delivery may prove pivotal in the effective reversibility of neurodegeneration at the early stages of the disease where motor control symptoms are most prominent. The study also concluded that repeated protein delivery, similar to gene therapy, improves neuronal function along the entire pathway, further demonstrating the

clinical relevance of the methodology and the immediate impact on to current clinical PD treatment.

4.6 Contribution

Previous studies have confirmed the safe and reversible BBB disruption in the striatum and midbrain of wild type mice allowing the penetration of neurotrophic factors that subsequently triggered downstream effects^{76,112}. In this chapter, we showed for the first time that single and multiple administrations of NTN upregulate respectively the depleted nigrostriatal pathway in the MPTP mouse model. Direct protein delivery is followed by viral vectors GDNF delivery that improves neuronal function similar to multiple NTN administrations.

The overall contribution of this study was the characterization, in terms of the increase in the tyrosine hydroxylase (TH) phenotypic marker and the associated physiological changes, of possible therapeutic alternatives in upregulating the dopaminergic activity in the Parkinsonian mouse brain. MPTP was confirmed to suppress TH immunoreactivity in the CPu and midbrain under a sub-acute regime. Direct protein delivery upregulated the depleted DA neurons in the SN region while only repeated direct protein delivery managed to stimulate the DA terminals in the CPu. Gene delivery was found to upregulate the depleted DA neurons in both the SN and CPu comparably to repeated delivery. The results of the studies described in this chapter have been published in peer reviewed scientific journals^{66,216}.

Regarding the research contribution, Shutao Wang, Ph.D. (Postdoctoral Research Scientist, Biomedical Engineering, Columbia University) worked on the gene delivery part by sonicating

and analyzing the data while shared the TH staining protocol, supervised the procedure and mentored all parts of the study. Gesthimani Samiotaki, Ph.D. (Postdoctoral Research Scientist, Department of Biomedical Engineering, Columbia University) worked on the part of single administration of NTN in terms of conducting sonications, performing immunohistochemistry and analyzing the data. Tao Sun, B.A. (Ph.D. student, Biomedical Engineering, Columbia University) helped analyzing and assessing the sonication cavitation profile and Yang Han, M.S. (Ph.D. student, Biomedical Engineering, Columbia University) assisted with image analysis and 3D reconstructions. The simulations were developed and analyzed by Hermes A. S. Kamimura, Ph.D. (Associate Research Scientist, Biomedical Engineering, Columbia University). Oluyemi Olumolade, B.A. (Research Associate, Biomedical Engineering, Columbia University), Camilo Acosta, B.A. (Research Associate, Biomedical Engineering, Columbia University) and Tara Kugelman, B.A. (Ph.D. student, Biomedical Engineering, Columbia University) assisted with the selection of anti-bodies for this study, animal surgery, staining, stereology counting and image acquisition. The author would like to deeply thank Vernice Jackson, PhD (Associate Research Scientist) for preparing the MPTP mouse model, sharing staining protocols, performing and training the research associates for cervical dislocations and all their invaluable scientific input. Finally Serge Przedborski, MD, PhD, (Assistant Professor, Neurology, Neuroscience, Pathology and Cell Biology, Columbia University) for his contribution in the study design, data interpretation and his general mentorship, input and suggestions for the study, as well as providing us with resources (animal facilities, etc) from his laboratory.

Chapter 5: Focused ultrasound-induced blood-brain barrier opening initiates pathological changes in two different Alzheimer's mouse models.

In chapter 4, we explored the beneficial outcomes of neurotrophic delivery in transgenic animals. An open question that emerged from the application of FUS-induced BBB opening as a drug-delivery strategy was the percent of ultrasound contribution to the overall beneficial effect. The immunomodulatory effect of FUS-induced BBB opening will be explored in this chapter under the prism of pathological amelioration in two Alzheimer's mouse models. Once establishing the effect of ultrasound application in the isolated tau pathology, we will then explore the sonication outcomes in brains suffering from the simultaneous presence of amyloid and tau that resembles greatly the human AD pathology.

5.1 Unilateral focused ultrasound-induced blood-brain barrier opening reduces phosphorylated tau from the rTg4510 tauopathy mouse model.

5.1.1 Abstract

The neuropathological hallmarks of Alzheimer's disease include amyloid plaques and neurofibrillary tangles. Tau pathology correlates well with impaired neuronal activity and dementia. Focused ultrasound coupled with systemic administration of microbubbles has previously been shown to open the blood-brain barrier and induce an immune response, which, in an amyloid AD mouse model, resulted in the reduction of the amyloid brain load. In this study, we investigated the effect of focused ultrasound at the early stages of tau pathology (pre-tangle) in the rTg4510 mouse model. Reduction of phosphorylated tau from the hippocampal

formation processes, and particularly the pyramidal CA1 neurons, was noted in the ultrasound-treated brains without an associated increase in the phosphorylated tau-affected cell somas, typically associated with disease progression. Attenuation of the pathology was found to correlate well with the ultrasound-initiated immune response without compromising neuronal integrity. Unilateral ultrasound application resulted in a bilateral effect indicating a broader reduction of the phosphorylated tau. Findings presented herein reinforce the premise of ultrasound in reducing tau pathology and thus curbing the progression of Alzheimer's disease.

5.1.2 Introduction

As previously described, Alzheimer's disease' defining features include changes in the brain histology and behavior microscopically described by the combinatorial presence of amyloid plaques and neurofibrillary tangles¹³. From clinical standpoint, the cornerstone in prevention and management of Alzheimer's disease is the deceleration of the progression through non-pharmacological approaches -behavioral techniques and adjusted nutrition- and pharmacological agents targeting cognition enhancement and systemic complications management¹⁰. Clinically, several phase III trials have been performed in patients with mild-to-moderate Alzheimer's disease but failed to show significant improvement in their primary outcomes^{217,218}. It was only until four years ago that the phase 1b clinical trial administering aducanumab in A β PET-positive patients (prodromal or mild AD) reported on reduced levels of A β in a dose- and time-dependent regime, yet the trial was not valued for the clinical endpoints given the observational nature of the data and the missing corrections in the statistics²¹⁹. Finally, the emerging technology of FUS was recently evaluated in terms of its clinical safety and feasibility in five early-to-moderate

Alzheimer's patients, succeeding in inducing a transient BBB opening⁵ without adverse effects¹¹⁶.

FUS has been evaluated in experiments involving the safe BBB disruption of various animal species including rodents, lagomorphs and primates^{26,27,51,119} and in different disease-mimicking models^{61,62,64,67}. FUS-induced BBB opening was initially introduced as a surrogate to drug delivery techniques that fell short in efficaciously surpassing the hindrances posed by the BBB hence their invasive and/or non-targeted nature²⁵. Specifically in Alzheimer's disease, antibodies against A β ^{61,220} have been mediated into the brain parenchyma by FUS, which resulted in the amyloid plaque load reduction. More importantly, these studies showed that amyloid could be cleared even in the absence of the antibody indicating the immense potential of FUS-facilitated BBB opening as an immunomodulatory stimulant. Transcriptomic analysis of the FUS-induced bioeffects outlined the profile of the triggered acute inflammation. Aside from forming an environment that could favor neuro- and angiogenesis, FUS-induced BBB opening was proven to contribute to the clearance of pathological proteins²²¹ accounting microglia activation as part of the response^{61,62}.

The role of microglia in neurodegenerative diseases remains a challenging topic. Although microglia respond immediately to acute injury, morphologically activated microglia for an extended period of time fail to synthesize inflammatory mediators that could negatively impact neuronal integrity⁸⁰. Prolonged activation of microglia is present in chronic neurodegenerative disorders, yet efforts to inhibit inflammatory mediators secreted by microglia failed to ameliorate the degeneration⁸⁰. In Alzheimer's disease, microglia acquire an "activated" phenotype yet fail to

reduce amyloidosis⁸¹, while the link between microgliosis and tau pathology remains to be established^{79,82}. Stimulus-dependent conformational changes and dystrophic microglia have been associated with tau pathology, while re-programming of the microglia to healthier phenotypes has recently emerged as a therapeutic strategy^{83,84}.

Whether FUS-induced BBB opening using a safely tolerated paradigm^{61,62} could drive an immune response characterized by the activation of microglia⁵³, and/or infiltration of peripheral immune cells^{51,53,222} such as macrophages and monocytes to help ameliorate such pathologies, remains unclear but these mechanisms could explain the positive effects observed. Recently, a decrease in phosphorylated tau from the entorhinal cortex in a human-tau mutant transgenic mouse strain (line pR5) has been reported following antibody delivery by repeated FUS-mediated BBB opening over the entire brain⁶⁴. However, the interaction of FUS with tau pathology has not been studied from the immunotherapeutic angle.

We have now examined whether early-stage tau pathology can be attenuated by ultrasound to (i) investigate the efficacy of unilateral FUS, as an adjuvant treatment, for the reduction of phosphorylated human tau in the hippocampus of the rTg4510 mouse model of AD and (ii) identify the response of the FUS-initiated immune reaction to the pathology.

5.1.3 Materials and Methods

***In vivo* experiments**

For this study 13 male mice of the rTg4510 line (overexpressing human tau pathology) were included, 10 at the age of 3.5 months and 3 at the age of 4.5 months. The same age animals were

randomly assigned to the sham and sonicated groups (five mice per group) while the older mice were utilized in the optimization and validation of the algorithms. Animals were group-housed under standard conditions (12 hr light/dark cycles, 22°C), were provided with a standard rodent chow (3 kcal/g; Harlan Laboratories, Indianapolis, IN, USA) and water ad libitum. All procedures involving animals were approved by the Columbia University Institutional Animal Care and Use Committee.

All mice involved in the study (sham and sonicated) were anesthetized with a mixture of oxygen and 1-2% isoflurane (SurgiVet, Smiths Medical PM, Inc., WI), placed prone with the head immobilized by a stereotaxic apparatus (David Kopf Instruments, Tujunga, CA) and depilated to expose the suture anatomy and minimize acoustic impedance mismatch. Identification of the parietal and interparietal bone intersection enabled proper positioning of the transducer following a grid-guided targeting procedure²⁷. Targeting the hippocampal formation involved positioning of the transducer 3 mm anteriorly to the lambdoid suture, and 1.5 mm laterally towards the left hemisphere to cover the dorsal part, while 2 mm anteriorly and 3.2 mm laterally for the ventral part. A bolus of 0.1 $\mu\text{L/g}$ of body mass polydisperse manufactured in-house^{29,199} microbubbles diluted in saline (8×10^8 #/ mL, mean diameter: 1.4 μm) was injected intravenously, in all mice, immediately preceding the sonication.

Five mice (3.5 months old) were sonicated for 60 s, with a pulse length of 6.7 ms and a repetition frequency of 10 Hz at PNP of 0.45 MPa after accounting for 18% murine skull attenuation. Acoustic emissions were monitored in real time⁴³ to assess the degree of cavitation. The remaining five mice at 3.5 months of age and the 4.5 months old animals were subjected to the

procedure without triggering the transducer (sham groups). All animals underwent magnetic resonance imaging for BBB opening confirmation and safety assessment. The same procedure was repeated once per week for four consecutive weeks while the animals survived for one day after the last treatment prior to sacrifice.

Focused ultrasound

A single-element, spherical-segment FUS transducer (center frequency: 1.5 MHz, focal depth: 60mm, radius: 30mm; axial full-width half-maximum intensity: 7.5 mm, lateral full-width half-maximum intensity: 1 mm, Imasonic, France), driven by a function generator (Agilent, Palo Alto, CA, USA) through a 50-dB power amplifier (E&I, Rochester, NY, USA) was used to target the hippocampus. A needle hydrophone (HGL-0400, Onda Corp., Sunnyvale, CA) was used for the transducer calibration, which measured the acoustic beam profile in a tank filled with degassed water. A central void of the therapeutic transducer held a pulse-echo ultrasound transducer (center frequency: 10 MHz, focal depth: 60mm, radius 11.2 mm; Olympus NDT, Waltham, MA) used for alignment, with their two foci aligned. The imaging transducer was driven by a pulser-receiver (Olympus, Waltham, MA, USA) connected to a digitizer (Gage Applied Technologies, Inc., Lachine, QC, Canada). A cone filled with degassed, distilled water was mounted onto the transducer assembly. The transducers were attached to a computer-controlled 3D positioning system (Velmex Inc., Lachine, QC, Canada).

Magnetic resonance imaging

Following the ultrasound procedure, all animals underwent scanning with the 9.4T MRI system (Bruker Medical, Boston, MA). The mice were placed in a birdcage coil (diameter 35 mm),

while being anesthetized with 1 – 2% isoflurane and respiration rate was monitored throughout the imaging sessions. MR images were acquired using a contrast-enhanced T1-weighted 2D FLASH sequence (TR/TE 230/3.3 ms/ms, flip angle: 70°, number of excitations: 6, field of view: 25.6 mm × 25.6 mm, resolution 100 µm x 100 µm x 400 µm), 30 minutes following the intraperitoneal bolus injection of 0.3 ml gadodiamide (GD-DTPA) (Omniscan, GE Healthcare, Princeton, NJ). As previously reported, gadodiamide provides spatial information of the BBB opening by temporally enhancing the MR signal relative to the ultrasound parameters³⁷. In addition, T2-weighted MRI was performed one day after the sonication to detect any potential damage using a 2D RARE sequence (TR/TE 2500/10 ms/ms, echo train: 8, number of excitations: 8, field of view: 25.6 mm × 25.6 mm, resolution 100 µm x 100 µm x 400 µm). The sequences employed in this study have been previously optimized by our group⁹⁴.

Immunohistochemistry

All animals were transcardially perfused (30 mL PBS followed by 60 mL 4% paraformaldehyde) one day after the last treatment. The brains were extracted, immersed in PFA fixative for 24 h and then in 30% Sucrose for at least 2 days prior to freezing. After brains were frozen on dry-ice, cryostat-cut coronal hippocampal sections (35 µm) were collected in anti-freezing solution. Then, 2-3 free-floating sections of the dorsal hippocampus with a 6-sections gap were processed for immunohistochemistry. The sections were sequentially washed in 0.1M PBS, treated with 5% donkey serum in 0.3% PBST for thirty minutes with the addition of mouse seroblock for the last ten minutes followed by overnight incubation at 4°C with the primary antibodies: i. mouse anti-human-phospho-tau (AT8, 1:500, Sigma) and rabbit anti-CD68 (1:500, abcam), ii. mouse anti-human-phospho-tau (AT8, 1:500, Sigma) and rabbit anti-Iba1 (1:500, abcam), iii. mouse anti-β-

tubulin III (1:500, Sigma) and rabbit anti-NeuN (1:500, abcam) antibodies. Then, sections were washed in PBS and incubated for 60 min in 0.3% PBST with 5% donkey serum containing the respective donkey-raised secondary antibodies, Texas Red-, Alexa488- and Alexa405-conjugated (1:1000). After the incubation, the sections were washed again in PBS and mounted on slides. The slides were merged into 0.3% sudan black for five minutes, rinsed with 70% ethanol, washed three times with 0.02% Tween20 in PBS and treated with Hoechst 33342 (5 μ m/ml) for ten minutes, when cell visualization was necessary. Finally, the slides were washed with PBS and cover slipped with Fluoromount solution.

Confocal microscopy

The large field confocal images of the hippocampus were captured on a 20 \times objective of a Nikon confocal microscope (Nikon Instruments Inc., Melville, NY, USA) with the same exposure parameters for the lasers. Tile (mosaic) and a Z-stack (2 μ m step, 7 series) were necessary were acquired and processed with ImageJ to produce the resulting maximum intensity image. For colocalization assessment, three single-tile and non-overlapping images covering the CA1 region were captured on a 60 \times objective of the same microscope. The acquired Z-stack (1 μ m step, 13 series) was analyzed with ImageJ to construct the orthogonal views¹² and the corresponding video included in the Supplementary Material. Custom algorithms in MATLAB (R2017a, MathWorks, Inc., Natick, MA, USA) further analyzed all images.

Quantification Algorithms

MR Volumetry

The enhancement in the horizontal plane of MR images was quantified by volumetric analysis encompassing the hippocampal formation³⁷. Two same-size ellipsoidal ROIs were constructed, covering the targeted the contralateral sides. The sum of the pixels in the ipsilateral ROI surpassing the mean value of the contralateral ROI yielded the area of the BBB opening while performing the same analysis in 17 consecutive slices, matching the dimensions of the focal beam, resulted in the BBB opening volume reported herein³⁷.

Confocal image analysis

The hippocampal formation was isolated from the surrounding brain tissue utilizing the merged-channel images (composite), thus constructing a hippocampal mask. For individual biomarker analysis, the masked composite maximum intensity images were split into the constituent channels. Color-based segmentation by k-means clustering was applied in every channel to determine the sum of pixels belonging to the highest-intensities cluster that was then normalized by the sum of all pixels composing the hippocampal mask (Figure 23a).

Additionally, a structural algorithm was developed to quantify the number of cells and the length of the processes affected by phosphorylated tau (Figure 23b). As previously described, the hippocampal mask was constructed and applied onto the red channel followed by color-based segmentation. The Hough transform was employed to detect circular objects and identify pathological cell centers. Residual noise was eliminated by singular value decomposition. Morphological operators enabling the connection of neighboring pixels and skeletonization, revealed the backbone of the processes along with branches and endpoints. The algorithm utilized the cell center coordinates as the initial point to search for the presence of a skeleton in a

defined neighborhood. Every path was followed through all potential branches until reaching an endpoint. The distance of that endpoint to the cell center was measured and the longest 5% of the paths leading to the same cell were measured and averaged. Since the hypothesis of this study was that focused-ultrasound induced BBB opening reduces phosphorylated tau especially from the CA1 processes, false positives (erroneously finding a long path other than the true path) were preferred as errors avoiding favorable bias.

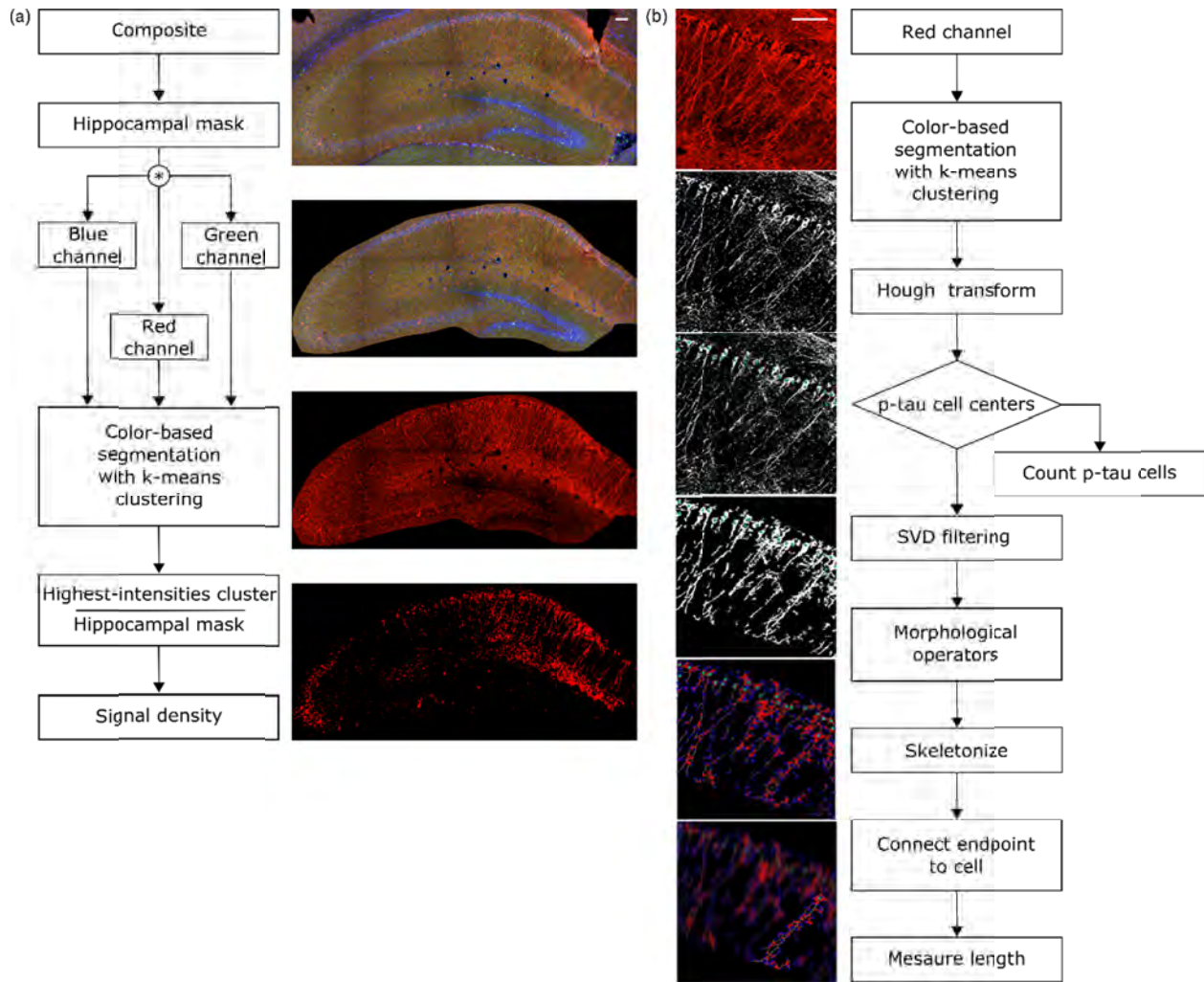


Figure 21: Quantification algorithms. (a) The structural algorithm performed color-based segmentation with k-means clustering on the red channel filtering out weaker intensities. The Hough transform detected the cells as bright circular objects on a dark background, providing their total count and the corresponding coordinates. Singular value decomposition (SVD) was used to filter the image followed by morphological operators that skeletonized and revealed the spine of the process. The coordinates of each cell were then

used to initiate a stemming process search until an endpoint was reached. The distance of the endpoint to the cell center was measured. (b) The intensity algorithm utilized the composite image as input to generate a hippocampal mask, omitting the irrelevant neighboring structures. The mask was applied to all three channels separately followed by color-based segmentation via k means clustering. For every channel the density is reported as the ratio of the pixels belonging to the cluster with the highest value over the pixels constituting the entire hippocampal mask. Scale bar, 100 μ m.

To report the difference in pyramidal processes length between groups, a Monte Carlo simulation was performed. The simulation constructs the probability density function (PDF) for the processes length of each hemisphere (sham contra, sham ipsi, sonic contra and sonic ipsi) followed by random sampling from each PDF and pairwise subtraction of the random samples²²³. The subtraction is demonstrated as the cumulative density distribution revealing the percent of length difference.

Both the intensity- and structural- algorithms as well as the Monte Carlo simulation were evaluated in terms of accuracy by comparing the pathology of rTg4510 mice at different ages. As the disease progresses, the cells affected by the pathology should significantly increase as phosphorylated tau spreads from the processes that become shorter^{9,224}. Pathological deterioration is also reflected by increased activity of immune cells (microglia and/or macrophages) evident by elevated CD68-positivity²²⁵. Increased cell population and CD68-positivity accompanied by decreased length of the processes affected by phosphorylated tau was indeed detected in the older mice with the associated changes in intensity⁶³.

To estimate the statistical dependence between p-tau and microglia, and report on their colocalization probability, standard methods were employed; i. the Pearson's correlation coefficient (PCC) and ii. Manders' overlap coefficients; M1 and M2, where the threshold was set to the estimated background mean value²²⁶.

The equations describing the coefficients were implemented in MATLAB. Following the isolation of the CA1 sector from the surrounding tissue, the dependency coefficients were calculated using the raw intensities as inputs. Pixels outside the region of interest were assigned the arithmetic representation for Not-a-Number (NaN) that does not affect the calculation of the coefficients.

Statistical analysis

All values are expressed as means \pm standard error of the mean (SEM). Differences between the means of the sham and treated groups as well as the ipsilateral and contralateral to the sonication sides were analyzed using 2-way repeated measures ANOVA. Statistical analysis was performed on the mean value obtained per animal; however, all samples (2-3 slices per mouse brain) are presented in the bar plots included in the study. Longitudinal analysis of the BBB opening volume and differences in the means distributed over the hippocampal subfields were analyzed with multiple Student's t tests. The P values in both analyses were adjusted based on the Holm Sidak post hoc correction. All statistical analyses were performed using Prism 8 (Graphpad Software, San Diego, CA, USA) and the null hypothesis was rejected at the 0.05 level. Throughout the manuscript the "F" value in respect to the associated degrees of freedom is provided with the P value adjusted to the corrected multiple t-tests. The significance levels correspond to : * $P \leq 0.05$, ** $P \leq 0.01$, *** $P \leq 0.0005$, **** $P < 0.0001$.

5.1.4 Results and Discussion

Confirmation of the BBB opening and volume assessment was performed prior to the immunohistochemical analysis to evaluate potential differences in the opening volume. Representative coronal planes of the BBB opening at Bregma -2.70 ± 0.56 are shown in Figure 24 for each group per week of sonication. Quantification of the opening volume (transgenic; wild-type, week 1: $54.8 \pm 0.9 \text{ mm}^3$; $52.83 \pm 3.9 \text{ mm}^3$, week 2: $52.46 \pm 2.9 \text{ mm}^3$; $54.98 \pm 2.6 \text{ mm}^3$, week 3: $54.22 \pm 3.3 \text{ mm}^3$; $55.48 \pm 1.6 \text{ mm}^3$, week 4: $52.5 \pm 2.5 \text{ mm}^3$; $54.49 \pm 4.3 \text{ mm}^3$) did not reveal any significant differences in the opening size across weeks suggesting that repeated ultrasound application did not compromise the integrity of the barrier at least at this age (3.5-4.5 months old). Moreover, the comparable BBB opening volumes of transgenic to wild-type animals indicated a similar response of the BBB to the ultrasound without evidence of edematous incidences as indicated by the T2-weighted images.

FUS applied within the safety regime has been proven beneficial^{62,76,220} while vascular incidences have been reported in sonication protocols involving overlapping regions and repeated applications⁵³. Despite operating in a safe ultrasound parametric space evaluated in previous studies^{76,112}, we were interested in determining any potential effects of the technique on the neuronal integrity. Therefore, two slices per transgenic brain were counterstained for neuronal cells with the anti-NeuN (neuron-specific nuclear protein) and anti- β -tubulin III antibodies (neuron-specific microtubule element) along with brain slices from a wild-type mouse to assess the sensitivity of the biomarkers. Neuronal compromise was qualitatively evident when comparing the transgenic to the wild-type brains by the dentate gyrus' shrinking due to the

neuronal depletion in the rTg4510 mouse model at this age²²⁴ (Figure 25). Additionally, the neuronal processes in the

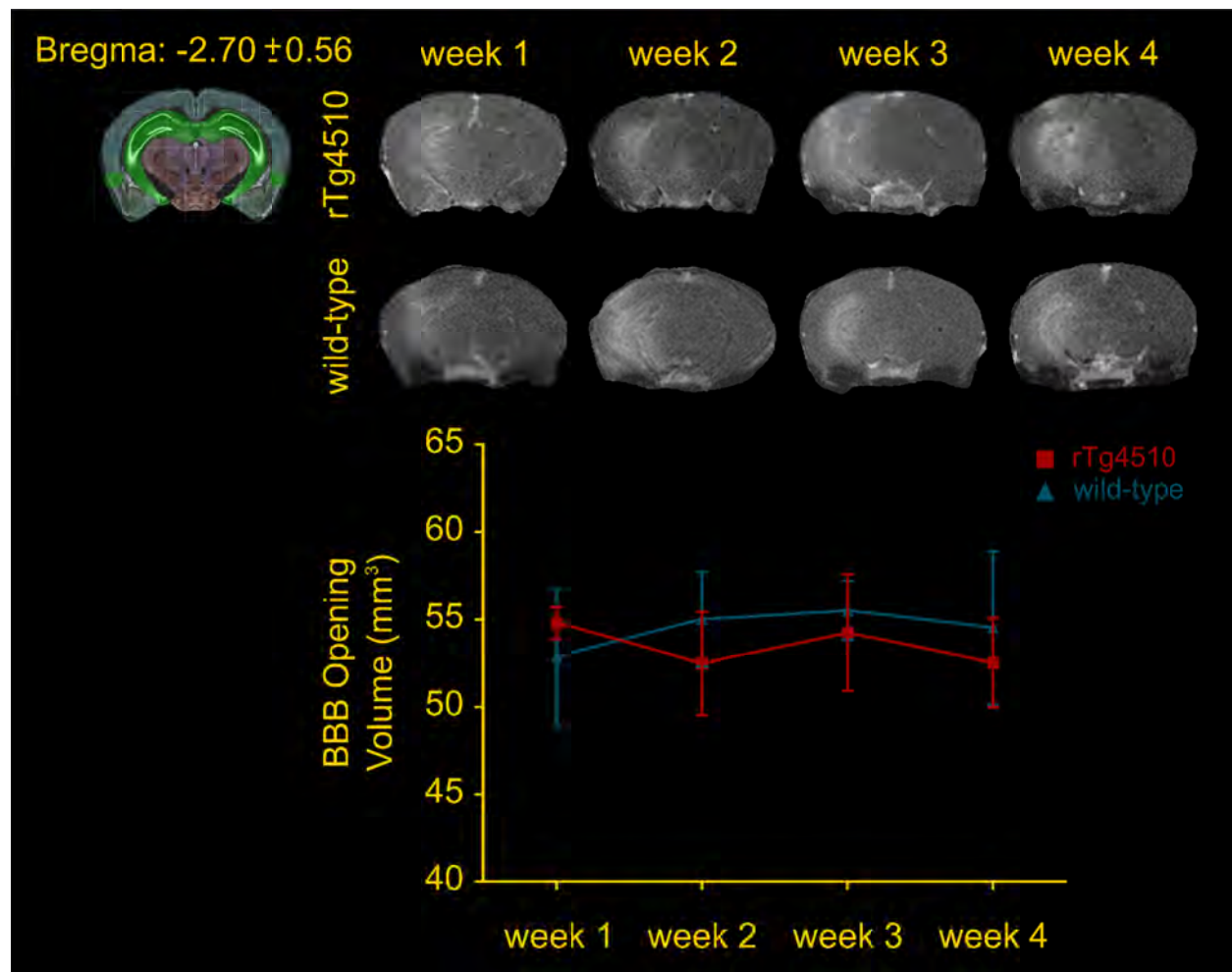


Figure 22: Volumetric analysis of the blood-brain barrier opening from the contrast-enhanced T1-weighted MR coronal images. The volumes of the transgenic animals were at the order of $54.8 \pm 2.02 \text{ mm}^3$, $52.46 \pm 6.59 \text{ mm}^3$, $54.22 \pm 7.44 \text{ mm}^3$ and $52.5 \pm 5.64 \text{ mm}^3$, while $52.83 \pm 8.81 \text{ mm}^3$, $54.98 \pm 5.97 \text{ mm}^3$, $55.48 \pm 3.75 \text{ mm}^3$ and $54.49 \pm 9.76 \text{ mm}^3$ of the wild-type mice for the four consecutive weeks. Longitudinal analysis did not show any significant difference across weeks. Additionally, the opening volumes did not differ between transgenic and wild-type animals within the same week interval.

wild-type hemispheres and particularly the CA1 sector were positive to the anti- β -tubulin III antibody along their in-plane length. On the contrary, the processes in the transgenic animals appeared more fragmented. Despite the differences observed between transgenic and wild-type brains though, no significant differences emerged from the application of ultrasound.

Quantification of the two channels separately based on their intensity normalized by their background (Figure 23a) showed that neither neuronal cells nor processes differed between the sonicated and sham brains (Figure 25). The neuronal cell density was $39.18 \pm 1.41\%$ and $36.46 \pm 1.25\%$, for the sham contralateral and ipsilateral side while $37.87 \pm 1.3\%$ and $39.18 \pm 1.29\%$ for the corresponding sides of the sonicated brains. Respectively, the neuronal processes density was $39.31 \pm 0.63\%$ and $39.43 \pm 0.97\%$ for the sham contralateral and ipsilateral side while $38.25 \pm 0.67\%$ and $39.56 \pm 1.04\%$ for the corresponding sides of the sonicated brains. These observations suggest that the ultrasound parameters applied in this study did not negatively impact the neuronal integrity at least to the sensitivity level of our detection.

Establishing the neuronal integrity, we were then interested to investigate the response of phosphorylated tau protein to the application of ultrasound and the BBB opening. Frozen floating tissue was processed for immunohistochemistry by incubation with antibodies against phosphorylated tau and immune cell reactivity using AT8 (a monoclonal antibody recognizing AD-related phosphorylation at Ser202/Thr205 on human tau protein) and CD68 (monoclonal antibody binding to the corresponding lysosomal receptor of macrophages) respectively. Confocal microscopy enabled visualization of the p-tau spatial profile as well as correlation with the immune response. The distribution of phosphorylated tau changes with disease stage with p-tau being present in the processes at early stages, but more pronounced in the somatodendritic compartment as the disease worsens⁹. Quantification of p-tau signal-intensity showed a significant reduction in the hemisphere treated with ultrasound (Figure 26b-c). In particular, we observed a reduction in the p-tau signal to the order of 57.35% ($F[1,8] = 34.32; P=0.0004$) when

comparing the contralateral hemispheres of the sham and the sonicated brains, and 72.65%

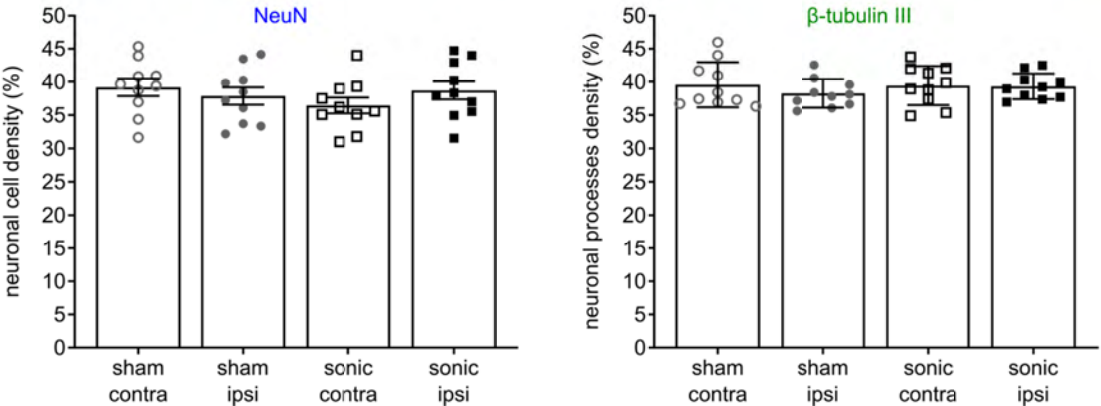
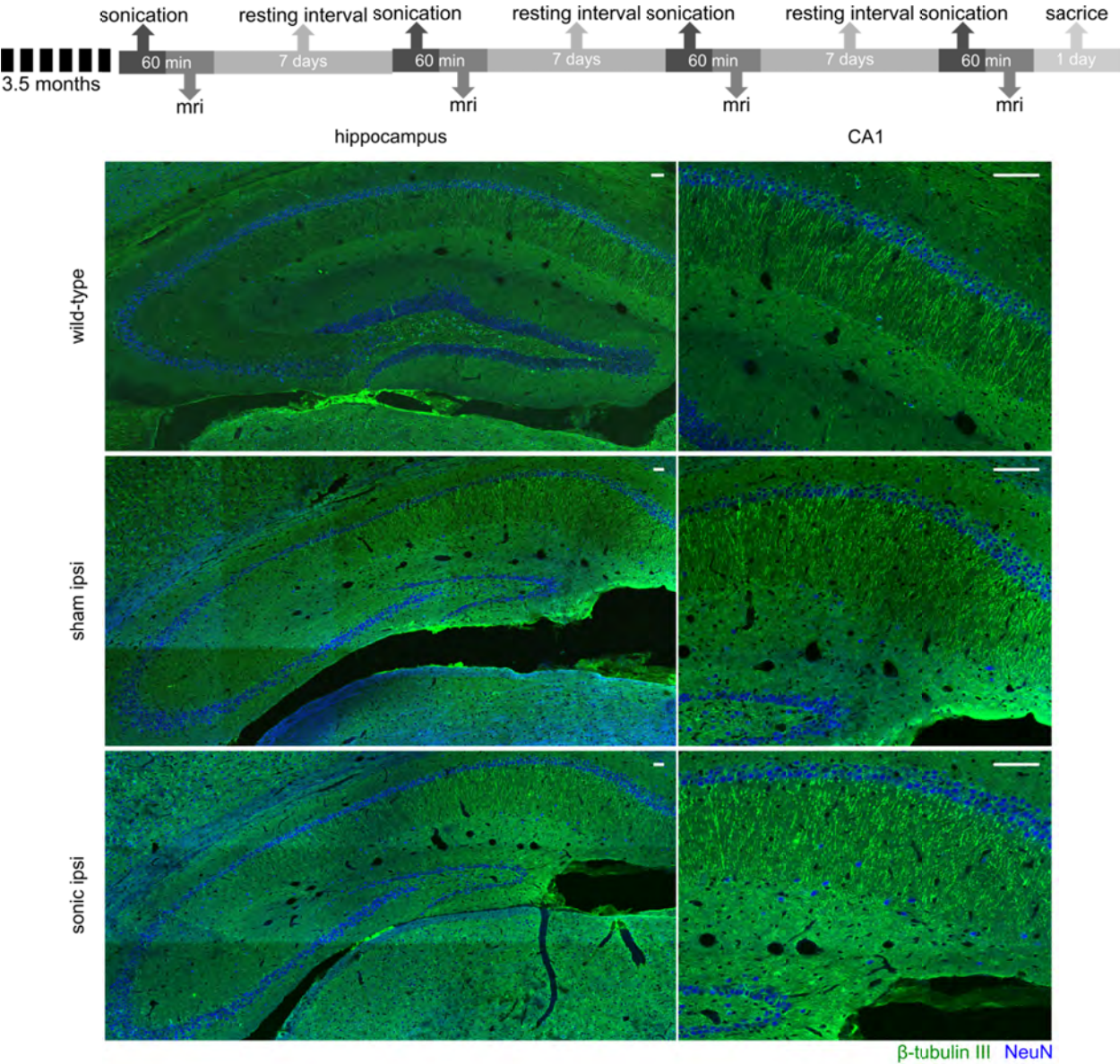


Figure 23: The timeline of the experimental procedure is shown at the top. Briefly, five mice of the rTg4510 line at 3.5 months of age were recruited for four sonications, once per week and were sacrificed a day after the last treatment. MRI was performed after each sonication to confirm targeting accuracy and successful opening. Two slices per transgenic brain were counterstained for neuronal cells with the anti-NeuN and anti- β -tubulin III antibodies along with brain slices from a wild-type mouse to assess neuronal integrity. Neuronal compromise could be qualitatively observed in transgenic animals compared to healthy mice by the decrease in the NeuN signal and the non-uniform signal emitted by the neuronal processes. However, no significant differences emerged from the application of ultrasound as shown by the quantitative measures. The mean (\pm standard deviation) neuronal cell density was $39.18 \pm 4.25\%$ and $36.46 \pm 3.77\%$, for the sham contralateral and ipsilateral side while $37.87 \pm 4.14\%$ and $39.18 \pm 4.09\%$ for the corresponding sides of the sonicated brains. Respectively, the mean value (\pm standard deviation) for the neuronal processes density was $39.31 \pm 1.91\%$ and $39.43 \pm 2.93\%$ for the sham contralateral and ipsilateral side while $38.25 \pm 2.13\%$ and $39.56 \pm 3.3\%$ for the corresponding sides of the sonicated brains. Scale bar, 100 μ m.

($F[1,8] = 34.32; P < 0.0001$) when comparing the ipsilateral hemispheres (Figure 26c). However, the total p-tau cell numbers detected by the algorithm did not differ among the groups or the hemispheres as shown in Figure 26d.

BBB opening induced by FUS has been shown to trigger an immune response determined by the energy deposited and the selected ultrasound parameters⁵¹. Under the current sonication regime, microglia activation was expected as the brain-residing myeloid cells reach for the sites of BBB leakage^{51,62}. Microglia are inherently activated by the pathology²²⁵, however, the binding ligand that induces the conformational changes governs their performance in the brain^{83,84}. Additionally, brain trafficking of peripheral immune cells has been associated with mitigation of neurological diseases attributed to their strong phagocytic capacitance²²⁷. However, peripheral immune cells are restrained from entering the brain, yet FUS has been shown to facilitate their infiltration by transiently disrupting the BBB^{51,53,222}. In this study, significant activation of immune cells on the order of 54.41% ($F[1,8] = 46.4; P < 0.0001$) and 41.6% ($F[1,8] =$

46.4; $P=0.0064$) was observed in the hemispheres treated with ultrasound and its contralateral

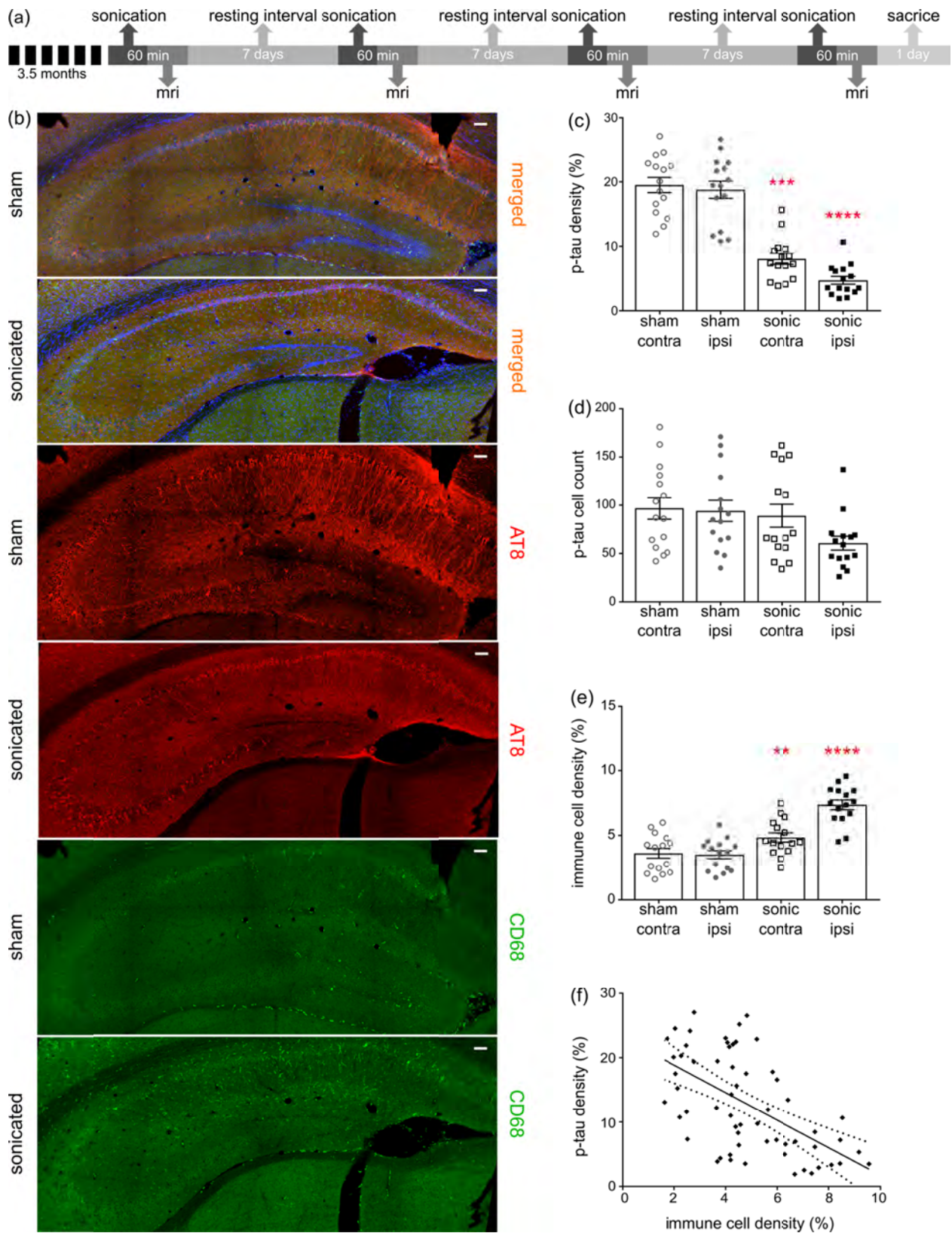


Figure 24: The timeline of the experimental procedure. For this immunohistochemical analysis brain slices from the transgenic animals were counterstained for phosphorylated tau with the AT8 antibody and immune cell activation with the CD68 antibody while imaged by confocal microscopy. (b) Representative composite images of the sham and sonicated ipsilateral hemispheres are shown with the red channel corresponding to the signal emitted from phosphorylated tau, the green channel reflecting the immune response and the blue channel representing the cell-dye Hoechst 33342. (c) Bar scatter plot representation of the samples showing a significant reduction in the p-tau signal when comparing the hemispheres of the sham and the sonicated brain. In particular, we observed a reduction in the p-tau signal on the order of 57.35% ($F[1,8] = 34.32; P=0.0004$) when comparing the contralateral hemispheres of the sham and the sonicated brains, while 72.65% ($F[1,8] = 34.32; P<0.0001$) when comparing the ipsilateral hemispheres. (d) On the other hand, the total cell numbers detected by the algorithm did not differ among the groups or the hemispheres (e) Immune cell activation was confirmed by the signal obtained from the CD68 marker. Immune system upregulation was expected due to pathology but a 54.41% increase ($F[1,8] = 46.4; P<0.0001$) was observed in the hemisphere treated with ultrasound while a 41.6% ($F[1,8] = 46.4; P=0.0064$) increase in its contralateral side compared to the control brains. (f) Regression analysis between the p-tau signal and the immune cell activation yielded a significant deviation of the slope from the zero value suggesting a correlation between the two parameters ($r^2=0.3285$; $\beta=-2.136$; $P<0.0001$). Scale bar, 100 μ m.

side compared to the untreated brains (Figure 26e). Moreover, regression analysis between immune cells and p-tau signal revealed a negative correlation showing increased immune response in the brains with reduced phosphorylated tau presence (Figure 26f). Despite the relatively low correlation coefficient ($r^2=0.3285$), the slope of the regression significantly deviated from zero ($\beta=-2.136$; $P<0.0001$) indicating that the two variables vary together in the opposite direction.

Upon observation of the reduction in phosphorylated tau signal emitted from the sonicated hippocampus, further investigation of its spatial distribution along the pyramidal neuron was necessary. Given the CA1 being the hippocampal sector most affected by the pathology at this age in the rTg4510 model²²⁴ further quantification of the processes length affected by p-tau followed. In Figure 27a, it is qualitatively shown by the red channel that p-tau affects the neuronal processes along their in-plane length (longer p-tau processes) while application of

ultrasound decreases the neuronal processes depletion (shorter p-tau processes). Quantification of the p-tau processes length was performed by a custom algorithm that beginning from the cell soma tracked the pathological marker along the axon and returned its length (Figure 23b). In Figure 27b the cumulative density function (CDF) demonstrates the p-tau processes length across the four groups (sham contra, sham ipsi, sonic contra and sonic ipsi). The 95th percentile, denoted by the upper red line, crosses the CDF of the sonicated ipsilateral side at 300 μm (dotted red line), while at 700 μm (dotted red line) for the untreated brain. This finding suggests that the probability of finding a p-tau neuronal process equal or smaller than 300 μm in the sonicated brain and 700 μm in the unsonicated brain is 0.95. Despite establishing the high probability of finding shorter p-tau processes in the sonicated brain, to report on the differences in the p-tau processes length between the groups, a Monte Carlo simulation was designed²²³. The probability density function of the p-tau processes was constructed for the four groups. Samples from the distributions were randomly drawn, subtracted from each other pairwise and the cumulative density function of the resulting differences in length is reported herein^{228,229}. The CDF of the length difference in p-tau processes between the sham and sonicated hemispheres is shown in Figure 27c. The probability of the p-tau processes having the same length is 0.32 (zero crossing) suggesting that 68% of the p-tau processes in the untreated brains are longer than the sonicated ones. Another observation that could be extracted from this figure is that the probability of a p-tau process in the untreated brain being up to 600 μm longer than the sonicated brain is 0.94. Similar observations can be respectively drawn for the remaining groups. The accuracy of this method in the current application was evaluated by performing the equivalent analysis in the different rTg4510 age groups which followed the expected pathological outcomes.

Having established the reduction in p-tau signal in the CA1 sector as well as the increased activity of the immune cells triggered by the application of ultrasound, we were interested in investigating the colocalization probability of the brain-resident macrophages with the phosphorylated tau protein. Existing evidence suggests that the immune response triggered by the FUS-induced BBB opening results in the increased microglia activity^{61,62}. Therefore, we performed an additional immunohistochemical analysis utilizing the anti-Iba1-antibody (calcium-binding polyclonal antibody) and the anti-phospho-tau antibody described previously.

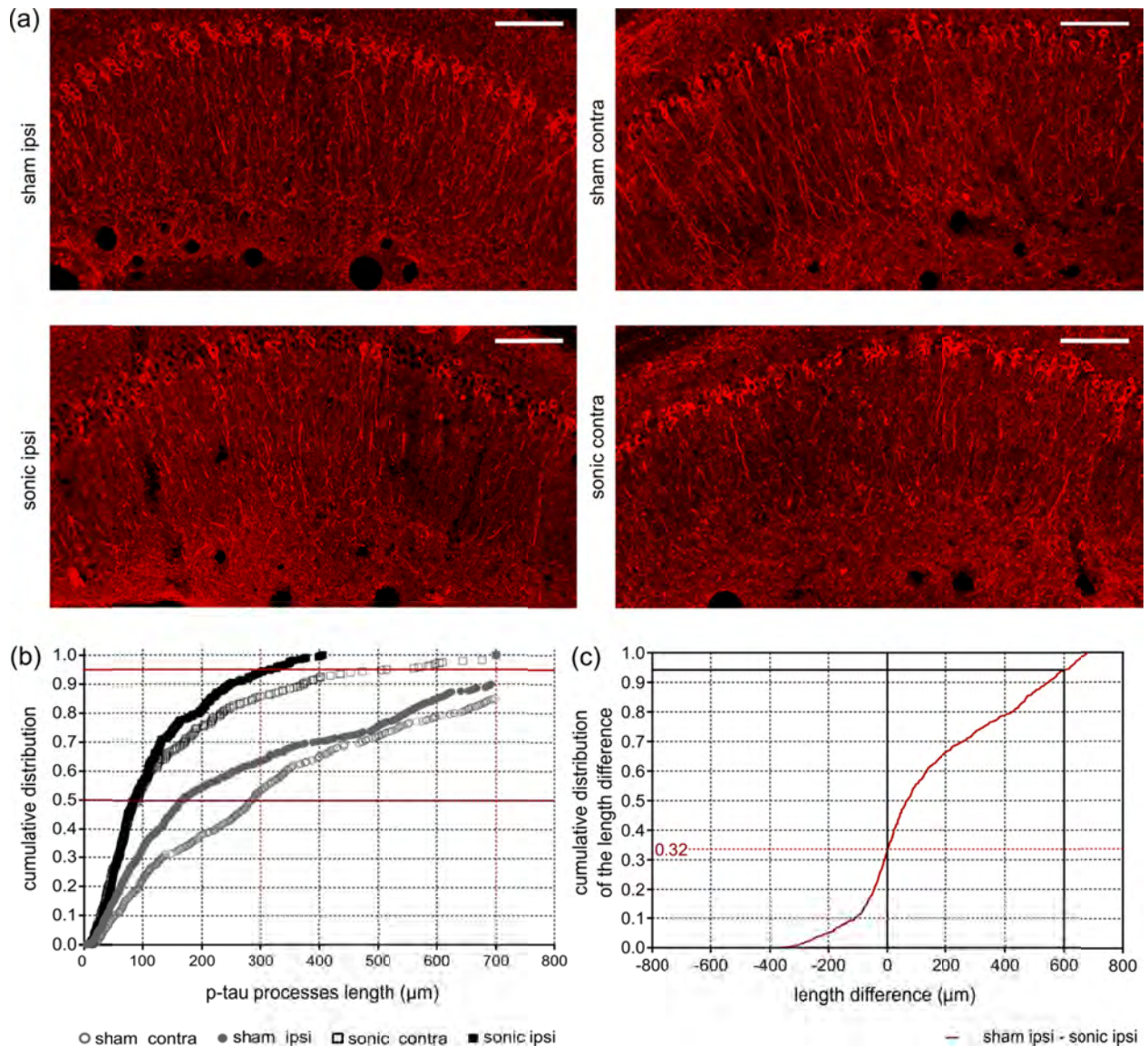


Figure 25: (a) Phosphorylated tau signal emitted from the affected pyramidal neurons of the ipsilateral and contralateral side in the CA1 sector of the sham and sonicated brains. (b) Comparison of the cumulative density function (CDF) of the p-tau processes length as obtained from each group (sham contra, sham ipsi, sonic contra and sonic ipsi). This graph describes the probability (y-axis) of finding p-tau processes of a certain or smaller length (x-axis). The 95th percentile (upper red line) crosses the CDF of the sonicated ipsilateral side at 300 μ m (dotted red line), while at 700 μ m (dotted red line) for the untreated brain. This finding suggests that the probability of finding a p-tau neuronal process equal or smaller than 300 μ m in the sonicated brain and 700 μ m in the unsonicated brain is 0.95. (c) The cumulative density function of the difference in p-tau processes length between the sham and sonicated hemisphere (ipsi sham-ipsi sonic). The zero crossing denote the probability of p-tau processes having the same length between the two hemispheres. From this CDF it can be observed that 68% of the neurons on the sham ipsilateral side are longer than those on the sonicated ipsilateral side. Scale bar, 100 μ m.

Since channel overlap in one plane does not suffice to justify biomarker colocalization, we investigated the orthogonal views¹² of all microglia cells captured within the images and representative magnified examples (60x objective magnified by a factor of three) are shown in Figures 28a-d. Qualitative evaluation of the channel overlap revealed that microglia verge on the p-tau processes and follow morphologically their structure in the sham brains without, though, engulfing them, as shown in Figures 6a,c. However, following the application of ultrasound, fragments of p-tau can be found within the microglia in both hemispheres of the sonicated brains (Figure 28b,d) as suggested by the channel overlap in all three planes). Quantitatively, Figures 28e-h include representative composite images from the CA1 region of each group with the corresponding monochromatic channels, where the green corresponds to the Iba1 biomarker and the red to the p-tau pathology. Each scatterplot shows the distribution of the pixels in the green-red coordinate system providing information on the covariance of the markers. The scatterplot colormap indicates the pixel density. Figures 28e and 28g demonstrate the spatial distribution of the microglia and p-tau pathology in the sham brain with a PCC of 0.0345 for the ipsilateral side and 0.0495 for the contralateral side. The slope of the linear regression line between the two channels is 0.0273 for the ipsilateral and 0.0386 for the contralateral sham hemisphere. These

findings suggest a positive covariance of the two channels while the small value of the slope suggests that for high red channel intensities the green channel values remain small. In Figures 6f and 6h, representative examples of the sonicated brain are shown with a PCC of 0.068 for the ipsilateral and 0.0583 for the contralateral hemisphere with the corresponding slopes on the order of 0.207 and 0.122 respectively. The increase in the slope could be attributed to the reduced signal intensity in the red channel accompanied by the increase in green channel intensity while the PCC values were found comparable between groups. As particularly shown in the Figures 28f and 28h scatterplots, the majority of the pixels spreads towards the higher values of the green channel while maintaining a relatively low value in the red channel. This finding suggests a decrease in the signal emitted from phosphorylated tau accompanied by an increase in the immune response as previously shown in Figure 26e. Cumulative results from all animals show comparable PCC values (Figure 28i) accompanied by a significant increase in the scatterplot slope on the order of 43% ($F[1.6]=6.214; P=0.047$) for the ipsilateral hemispheres along with a 26.7% increase, albeit not significant, for the contralateral hemispheres after the application of ultrasound (Figure 28j). Furthermore, the percent of red-to-green channel contribution, measured here by Manders' M1 overlap coefficient, significantly increased by 43% ($F[1.6]=162.5; P<0.0001$) for the ipsilateral hemisphere following FUS while the M2 coefficient decreased significantly ($F[1.6]=258.9; P<0.0001$) by 36.0% suggesting greater overlap between the green and the red channel. Similar findings were observed on the contralateral hemispheres with a 42.6% increase in the M1 coefficient and a 31.7 decrease in the M2 coefficient. The changes in the Manders' coefficients are summarized in Figures 28k and 28l.

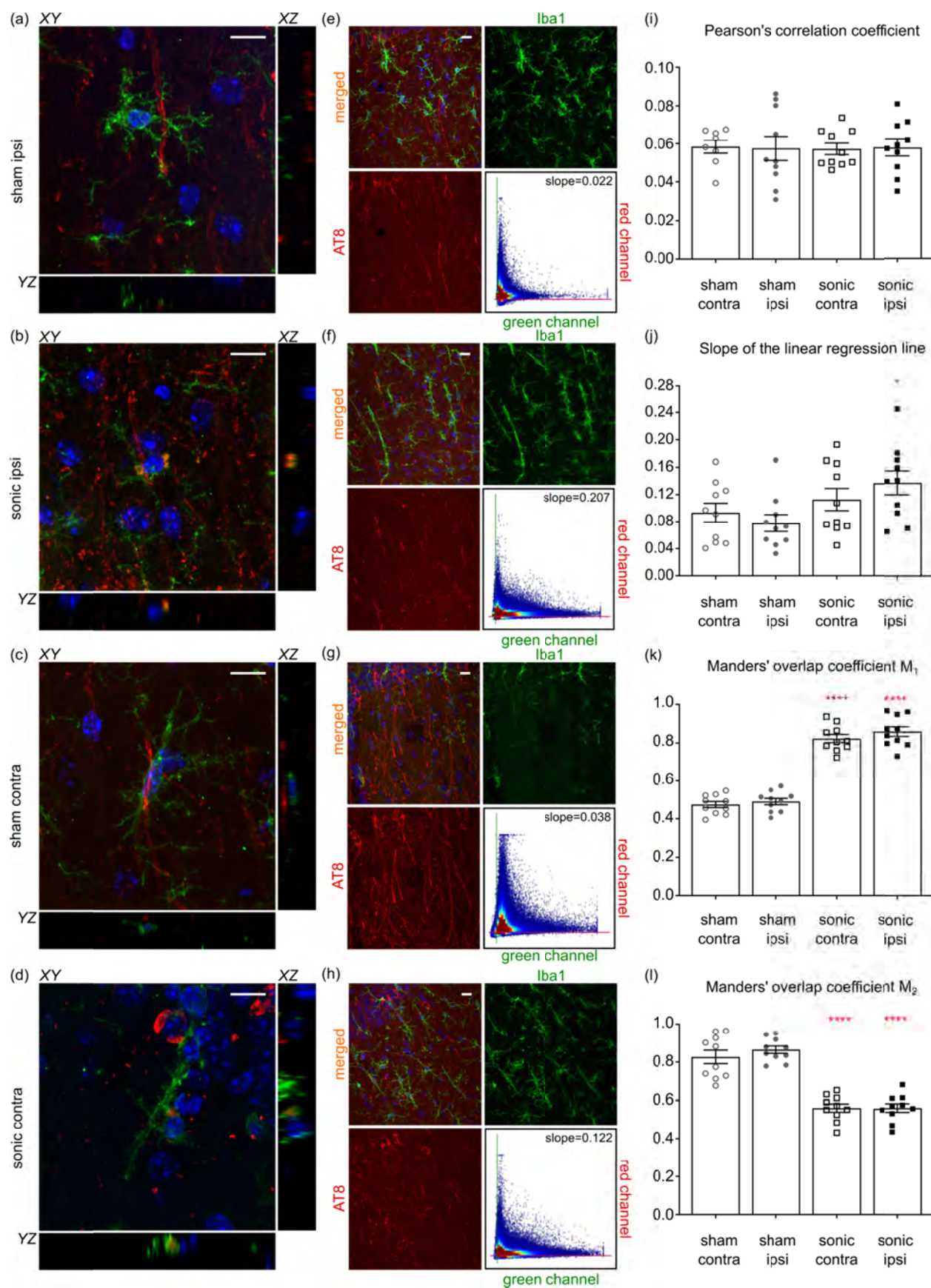


Figure 26: Microglia colocalization with phosphorylated tau protein. For this immunohistochemical analysis, two brain slices from the transgenic animals were counterstained for phosphorylated tau and microglia presence with the AT8 (red) and the Iba1 (green) antibody. Three Z-stack series were captured on a 60x objective covering the CA1 region. (a-d) Qualitative evaluation of the biomarker colocalization. The three planes, XY (main), XZ and YZ (orthogonal) are presented for a microglia cell. The images are magnified versions of the 60x objective and the corresponding video included in the Supplementary Material. (a, c) The microglia are shown to verge on the phosphorylated tau but not engulf it as indicated by the lack of the channel overlap in all three planes. (b, d) The microglia seem to engulf fragments of phosphorylated tau after the application of ultrasound in both hemispheres of the sonicated brains. The overlap of the two channels is consistent in all three planes. (e-h) The four panels follow the same structure: a composite image showing the merged and monochromatic images of the isolated CA1 sector and the scatterplot of the two channels. The scatterplot colormap indicates the pixels density. (e) The neuronal processes are largely affected by phosphorylated tau while the presence of microglia is evident in the ipsilateral sham hemisphere. The scatterplot has a slope (the slope obtained by performing linear regression between the two channels) of 0.022 suggesting that more pathological tau is present (higher red channel values) than microglia (smaller green channel values) while Pearson's correlation coefficient (PCC) is 0.0345 suggesting minor statistical dependence between the biomarkers. (f) The sonicated hemisphere experienced a reduction in phosphorylated tau and an increase in microglia presence indicated by the higher value of the fitted slope equal to 0.207, while the PCC increased for this case to 0.068. (g) Similar findings to the ipsilateral hemisphere can be extracted from the contralateral sides where the slope is 0.038 and the PCC of 0.058 in the sham brain while (h) the slope reached 0.122 and the PCC 0.068 in the sonicated brain. (i-l) Cumulative results on the dependency metrics. Comparable PCC values suggest that ultrasound did not affect the covariance of the two biomarkers. However, a significant increase in the slope of the linear regression line by 43% can be observed between the ipsilateral hemispheres ($F[1.6]=6.214; P=0.047$). Furthermore, the percent of red-to-green channel contribution, measured here by Manders' M1 overlap coefficient, increased significantly by 43% ($F[1.6]=162.5; P<0.0001$) while the M2 coefficient decreased significantly by 36% ($F[1.6]=258.9; P<0.0001$) suggesting greater overlap of the green with the red channel in the ipsilateral hemisphere. Similarly, M1 overlap coefficient increased by 42.6% and M2 coefficient decreased by 31.7% in the contralateral hemispheres. Scale bar, 10 μ m.

Overall we show that the complementary hallmark of the pathology, phosphorylated human tau protein, could be mitigated by the ultrasound-triggered upregulation of the immune system. In addition to the overall reduction in p-tau from the hippocampal formation, the spatial distribution

of the pathological marker, primarily in the CA1 region, changed after the application of ultrasound (Figures 26-28). Monte Carlo simulations confirmed the reduction in phosphorylated

tau from the pyramidal processes as their length decreased significantly with the application of ultrasound (Figure 27). Ultimately, ultrasound was considered to have attenuated the pathological progression that is associated with a significant increase of p-tau in neuronal cells.

Finally, the structural quantification showed that the contralateral neuronal processes were only 150 μm longer than the ipsilateral in the sonicated brain at the 95th percentile (Figure 27b). The significant presence of immune cells and their colocalization with p-tau protein in the contralateral-

to-ultrasound hemisphere could be driven by the migration of the resident microglia from the sonicated hemisphere to the contralateral side through the integrating tract⁷⁸ and/or the infiltration of peripheral cells^{51,53,222}.

5.1.5 Limitations and Conclusions

This study demonstrates the initial findings in bilateral reduction of phosphorylated tau in response to unilateral sonication due to the upregulation of the immune response in the rTg4510 mouse model without accompanied compromise of the neuronal integrity, findings that are in agreement with recent observations from alternative tau models⁶⁴. The p-tau reduction from the hippocampus could relate to deceleration of p-tau spreading or p-tau clearance from the brain. However, to assess the brain load in pathological proteins analytical techniques are needed. Moreover, whether the decrease in p-tau is functionally translatable in terms of memory improvement remains unknown due to the lack of behavioral outcomes.

The link between microgliosis and tau pathology is still debated in the existent literature^{79,82}. Stimulus-dependent conformational changes and dystrophy have been associated with tau pathology while re-programming of the microglia to healthier phenotypes has recently emerged as a therapeutic strategy^{83,84}. The beneficial effects of microglia on A β pathology have been supported by studies showing clearance of the plaques after FUS-induced BBB opening^{61,62} and this seems to be the same for tau pathology as well⁶⁴. Moreover, infiltration of peripheral macrophages has been emerged as a potential candidate for the amelioration of Alzheimer's disease^{227,230}. However, the primary challenge in those studies remains the limited brain infiltration due to the barrier, an obstacle that FUS has been shown to overcome²²². Distinction between microglia and peripheral immune cells including macrophages and monocytes was not attempted in the present study given that the employed antibodies (CD68 and Iba1) are not adequate markers of unique microglia signature^{225,231}. Therefore, the immune response observed in Figure 26 could be attributed to their synergistic action. The increase in immune cell activation was also accompanied by a reduction in the phosphorylated tau protein in the brains examined (Figure 26e-f). These findings were confirmed by the significant increase in the fitted slope (Figure 28e-i) suggesting a decrease in phosphorylated tau (red channel intensity) and an increase in microgliosis (green channel intensity). In addition, similar observations could be drawn from analyzing Manders' overlap coefficients, since they describe the fraction of one channel in compartments of the second channel²³². Along these lines, significantly increased M1 and decreased M2 indicate that the majority of the phosphorylated tau protein could be found in compartments associated with microglia following the application of ultrasound (Figure 28k,l). Although this finding could also be explained by the reduction in p-tau accompanied by the upregulated immune response (Figure 26e), single-cell, three-dimensional qualitative evaluation

of the channel overlap strengthens the argument that microglia could engulf the pathological tau (Figure 28a-d) following sonication. Whether FUS-induced BBB opening drives a “healthy” activation of microglia or infiltrating immune cells⁸² help reduce p-tau, remains unclear but these mechanisms could explain the positive effect established herein.

5.2 Focused ultrasound-induced blood-brain barrier opening initiates pathological changes in the 3xTg-Alzheimer’s mouse model.

5.2.1 Abstract

Focused ultrasound (FUS) has been proven to reduce amyloid plaques and hyperphosphorylated tau protein from the hippocampal formation and the entorhinal cortex in different mouse models of Alzheimer’s disease (AD). Given the beneficial effects of FUS on isolated AD pathologies, we investigated its functional and morphological outcomes on brains bearing both pathologies simultaneously. Eleven transgenic mice of the 3xTg-AD line (14 months old) and eleven age-matched wild-type animals received bilateral sonications covering the hippocampus once per week for four consecutive weeks. Following the last treatment, sonicated animals and control littermates underwent behavioral testing in the Morris water maze (MWM). All mice received a 5-day training familiarizing with reaching the escape-platform within 60 seconds. Following the training, the platform was removed and the amount of time spent in each MWM quadrant was quantified. The following week all animals were sacrificed and their brains processed for immunohistochemistry and biochemical analysis. Animals that received FUS spent significantly more time in the quadrant where the platform was located while this functional improvement correlated well with a 58.31% decrease in the neuronal length affected by tau confirmed by a 27.2% reduction in tau levels shown by immunoblotting. Amyloid plaque population, volume

and overall load were also decreased yet not significantly. For the first time, bilateral sonication significantly ameliorated the pathology and improved the spatial memory of transgenic animals with complex AD phenotype.

5.2.2 Introduction

Alzheimer's disease is a chronic and progressive neurodegenerative disorder resulting in a demented elderly population²³³. The AD defining features include the accumulation of amyloid- β plaques and intraneuronal neurofibrillary tangles, associated with gradual cognitive decline¹³. As of February 12, 2019, 28 out of 132 clinical trials administering pharmacological agents reached phase III stage, 11 investigating symptomatic agents-3 cognitive enhancers and 8 alleviating behavioral symptoms-and 17 disease modifying drugs-6 biological therapies and 11 small molecules. From the disease modifying therapeutic strategies, 10 are primarily, if not exclusively, targeting amyloid- β , one tau pathology and the rest are neuroprotective, anti-inflammatory or metabolic approaches²³⁴.

Ultrasound-facilitated BBB opening has been evaluated in a battery of clinical trials recruiting initially Glioblastoma multiforme (GBM) patients²³⁵. The completion of the trial revealed an increase in the median progression-free survival in the 19 enrolled patients, who received repeated treatments prior to systemic administration of carboplatin²³⁵. These beneficial outcomes paved the way for the expansion of clinical research utilizing ultrasound leading, eventually, to the first clinical trial revealing a safe and reversible BBB opening in 5 AD patients using MR-guided ExAblate system developed by Insightec (Insightec Inc., Tirat Carmel, Israel)¹¹⁶. Although a secondary outcome measure, researchers evaluated the amyloid load in the patients'

brains prior to and following the sonication without detectable changes. Providing the initial feasibility of the study, a phase IIa clinical trial was designed and is currently enrolling AD patients who will be repeatedly sonicated for three times in total (NCT03739905). Another clinical trial (NCT03671889) employing a similar MR-guided system is actively selecting AD patients to be embedded in a study with safety and efficacy as the primary outcome measures. Recently, our in-house developed clinical system for neuronavigation-guided FUS-induced BBB opening outside the magnetic bore was approved to treat 6 AD patients including assessment of pathological alteration following the procedure (NCT04118764)¹⁸⁶.

The ultimate aim of the clinical research in sonicating AD patients without delivering a pharmacological agent lies in the replication of the promising pre-clinical data that indicate pathological amelioration accompanied by functional improvement^{62,236}. Briefly, it was proven over the past decade that amyloid plaques can be reduced following repeated ultrasound targeted in one region or swept across the brain^{62,236}. One prominent mechanism for the amyloid clearance from the brain is the FUS-triggered immune response, since microglia have been found to engulf the amyloid plaques following sonication^{61,62}. Moreover, a time course study investigating the effect and persistence of a single sonication in amyloid plaques, concluded that the plaques shrank in more than half their initial volume, the days following sonication and the effect persisted for two weeks²³⁷. Therefore, repeated biweekly sonications were evaluated and indicated a plaque population reduction on the order of 27% accompanied by a 40% decrease in surface area²³⁷.

Preclinical findings targeting amelioration of tau pathology by FUS-induced BBB opening have been recently emerged. The studies conducted so far, though employing different transgenic animal models overexpressing mutant human tau, converge on their primary findings that phosphorylated tau can be eliminated from the brain following repeated sonications^{63–65,220}. Immune response to the sonication and autophagy have been proposed as potential mechanisms of tau clearance^{63,65}.

Despite the promising preclinical evidence, a common limitation in these studies is the expression of a single pathology in the animal models employed. Animals would overexpress proteins linked to familial AD (FAD), mutant amyloid precursor protein (APP), or APP and presenilin (PS) resulting in the formation of amyloid plaques²³⁸. Alternatively, rodents would overexpress a mutation (P301L or K369I) in the microtubule-associated protein tau (MAPT) resulting in destabilization of the microtubule network and tauopathies^{63–65,220}. However, these models fall short in resembling AD that is defined by the presence and interplay of both amyloid plaques and neurofibrillary tangle pathology. Therefore, the beneficial outcomes and the proposed mechanisms of these studies need to be evaluated in animal models with concurrent pathology.

We examine herein whether Alzheimer's pathology can be attenuated by ultrasound to (i) investigate the efficacy of repeated bilateral FUS for the reduction of human total tau and amyloid plaques from the 3xTg-AD mice that display both plaque and tangle pathology in the hippocampus and (ii) establish the functional imprint of the pathological amelioration attributed to the sonication module by Morris water maze (MWM)^{239–242}.

5.2.3 Materials and Methods

In vivo experiments

For this study, 22 female mice of the 3xTg-AD line were employed, at the age of 14 months. This widely used strain contains three mutations associated with familial Alzheimer's disease (APP Swedish, MAPT P301L, and PSEN1 M146V) and expresses a progressive development of both plaques and tangles²⁴³. Age- and gender-matched non-transgenic animals were included in the study as well, while all animals were randomly assigned to the sham and sonicated groups (eleven mice per group). Animals were group-housed under standard conditions (12 hr light/dark cycles, 22°C), were provided with a standard rodent chow (3 kcal/g; Harlan Laboratories, Indianapolis, IN, USA) and water ad libitum. All procedures involving animals were approved by the Columbia University Institutional Animal Care and Use Committee.

The animals involved herein (sham and sonicated) were anesthetized with a mixture of oxygen and 1-2% isoflurane (SurgiVet, Smiths Medical PM, Inc., WI), placed prone with the head immobilized by a stereotaxic apparatus (David Kopf Instruments, Tujunga, CA) and depilated to expose the suture anatomy and minimize acoustic impedance mismatch. Identification of the parietal and interparietal bone intersection enabled proper positioning of the transducer following a grid-guided targeting procedure²⁷. Targeting the hippocampal formation involved positioning of the transducer 3 mm anteriorly to the lambdoid suture, and 1.5 mm laterally to cover the dorsal part, while 2 mm anteriorly and 3.2 mm laterally for the ventral part. Both hemispheres were targeted in this study in alternating order in consecutive sessions.

The mice included in the sonication groups (transgenic and non-transgenic) received ultrasound in a cavitation-controlled regime (Ji, R. et al. *in preparation*) with a pulse length of 10 ms and a repetition frequency of 5 Hz at PNP of 0.40 MPa after accounting for 18% murine skull attenuation. Acoustic emissions were monitored in real time to assess the degree of cavitation and animals were injected with microbubbles until the cumulative cavitation dose reached a pre-set level associated with a single BBB opening on the order of $31.3 \pm 16 \text{ mm}^3$ (Ji, R. et al. *in preparation*). Thus, to accommodate for a constant cavitation level, the microbubble administration during the sonication ranged between 4-6 intravenous injections of polydisperse in-house manufactured^{29,199} microbubbles diluted in saline (0.1 $\mu\text{l/g}$, mean diameter: 1.4 μm), while the duration of a single sonication varied from 8 to 360 sec. Reinjections were administered when the cavitation levels dropped below 1 dB, relative to the baseline cavitation levels when no microbubbles were present. The sham groups were subjected to the same procedure without triggering the transducer, received the average microbubble injections, as established by the sonicated groups and remained under anesthesia the average sonication duration. All animals underwent magnetic resonance imaging for BBB opening confirmation and safety assessment. This procedure was repeated once per week for four consecutive weeks. Following the last sonication, all animals were transferred to the behavioral facility to acclimate for five days prior to behavioral testing. Behavioral testing using the MWM followed and lasted for five consecutive days. After the last day of behavioral testing, which was approximately three weeks after the last sonication, the mice were sacrificed at the age of 15-16 months.

Focused ultrasound

Similar to the previous section (section 5.1.3), the sonications were carried out by a single-element, spherical-segment FUS transducer operating at 1.5 MHz, driven by a function generator (Agilent, Palo Alto, CA, USA) through a 50-dB power amplifier (E&I, Rochester, NY, USA). The central void of the therapeutic transducer held a pulse-echo ultrasound transducer (center frequency: 10 MHz, focal depth: 60mm, radius 11.2 mm; Olympus NDT, Waltham, MA) used for alignment, with their two foci coaxially aligned. The imaging transducer was driven by a pulser-receiver (Olympus, Waltham, MA, USA) connected to a digitizer (Gage Applied Technologies, Inc., Lachine, QC, Canada). A cone filled with degassed, distilled water was mounted onto the transducer assembly. The transducers were attached to a computer-controlled 3D positioning system (Velmex Inc., Lachine, QC, Canada).

Magnetic resonance imaging

As per section 5.1.3, all animals underwent magnetic resonance scanning with the 9.4T MRI system (Bruker Medical, Boston, MA) following the sonication procedure. The mice were placed in a birdcage coil (diameter 35 mm), while being anesthetized with 1 – 2% isoflurane and respiration rate was monitored throughout the imaging sessions. MR images were acquired using a contrast-enhanced T1-weighted 2D FLASH sequence, 30 minutes following the intraperitoneal bolus injection of 0.3 ml gadodiamide (GD-DTPA) (Omniscan, GE Healthcare, Princeton, NJ) while T2-weighted MRI was performed one day after the sonication to detect any potential damage using a 2D RARE sequence⁹⁴.

Morris Water Maze (MWM)

In order to test spatial learning and short term memory, MWM was conducted, following the procedure previously described²⁴¹. The test was carried out during the light cycle and in a circular pool of 120 cm in diameter, filled 45 cm with tap water. The water was opaque by the addition of nontoxic white paint (Crayola) and kept at room temperature throughout. The pool contained spatial cues placed along the wall, which were kept constant through all testing days (Figure 27A). The trials were recorded and analyzed using WaterMaze video tracking software (Actimetrics).

The training was a five consecutive day acquisition period, made up of four trials per day. Each animal was assigned a specific target quadrant, consistent through all trials and days, which contained an escape platform. The platform was consistently kept 3 cm below the surface of the water, hidden from the animals during the test. The dropping-quadrant for each animal was alternated in a semi-random order and it would be either opposite or adjacent to the target quadrants; the assigned target quadrant was never selected as the dropping-quadrant (Figure 27A).

Each trial began when the animal was gently lowered into the water, facing the pool's wall. Each animal was allowed to find the platform within 60 sec. If the animal did not reach the platform within the given timeframe, it was then guided and gently placed on the platform. The animal was allowed to remain on the platform for 15 sec before being removed. After each trial the animal was placed in a cage lined with absorbent material and allowed to rest for 60 sec under a heat lamp. On the fifth day a probe trial was carried out, which occurred 3 hours after the last training trial. The hidden platform was removed from the target quadrant during the probe trial

and the animal was lowered into the quadrant opposite to the target quadrant. It was given 60 sec of exploration time before being removed. This probe trial tests the acquisition of spatial learning and short term memory^{239–241,244}. The behavioral measures that were recorded and analyzed were the latency to reach the platform, the distance traveled during the training trials and the time spent in every quadrant during the probe trial (Figure 27).

Immunofluorescence

Five animals per group (5/11) were transcardially perfused (30 mL PBS followed by 60 mL 4% paraformaldehyde) following the completion of behavioral testing. Similar to section 5.1.3, the brains were extracted, preserved in PFA for 24 h and then in 30% Sucrose for at least 2 days prior to freezing. After brains were frozen on dry ice, cryostat-cut coronal hippocampal sections (35 μ m) were collected in anti-freezing solution. Then, at least 3 free-floating sections of the intermediate and caudal hippocampus with a 6-sections gap were processed for immunohistochemistry. Prior to staining brain sections were pre-treated with 70% Formic Acid for 3 minutes to expose the A β 42 epitope. The sections were sequentially washed in 0.1M PBS, treated with 5% donkey serum in 0.3% PBST for thirty minutes with the addition of mouse seroblock (BUF041, Bio-Rad Laboratories) for the last ten minutes followed by overnight incubation at 4°C with the primary antibodies: i. mouse anti-human-tau (HT7, 1:500, (HT7, 1:500, MN1000, Invitrogen) and rabbit anti-human-A β 42 (1:500, AB5078P, EMD Millipore) antibodies. Then, sections were washed in PBS and incubated for 60 min in 0.3% PBST with 5% donkey serum containing the respective donkey-raised secondary antibodies, Texas Red- (1:1000, SAB3701155, Sigma-Aldrich) and Alexa488-conjugated (1:1000, SAB4600036, Sigma-Aldrich). After the incubation, the sections were washed again in PBS and mounted on

slides. The slides were washed three times with 0.02% Tween20 in PBS and treated with Hoechst 33342 (5 μ m/ml, H21492, Thermo Fisher) for ten minutes. Finally, the slides were washed with PBS and cover slipped with Fluoromount-G (00-4958-02, Thermo Fisher) solution.

The large field confocal images of the hippocampus were captured on a 20 \times objective of a Nikon confocal microscope (Nikon Instruments Inc., Melville, NY, USA) with the same exposure parameters for the lasers. Tile (mosaic) and a Z-stack (2 μ m step, 7 series) were necessary were acquired and processed to produce the resulting maximum intensity image.

Immunoassays

Six animals per group (6/11) were sacrificed by cervical dislocation with their brains extracted and the hippocampus dissected on ice within a minute prior to storage at -80°C. Frozen hippocampi were weighted and homogenized without thawing in T-PER buffer (78510, Thermo Fisher) containing a protease and phosphatase inhibitor cocktail (78442, Thermo Fisher). The homogenate was then split into two parts and stored at -80°C until used for immunoblots and enzyme-linked immunosorbent assays (ELISA).

The first part of the homogenates was centrifuged at 3,000 g for 10 min at 4°C and the supernatant was recovered. Proteins were run on 4-12% Bolt Bis-Tris precast gels (NW04120BOX, Invitrogen) using 1 \times MES SDS running buffer (B000202, Invitrogen) and under reducing conditions (B0009, Invitrogen). Proteins were then transferred to nitrocellulose membranes (iBlot2, IB23001, Invitrogen) using iBlot™ 2 Gel transfer system (IB21001, Invitrogen). Blots were blocked for 60 min using 5% non-fat dry milk (Omniblok, Americanbio

Inc) in Tris-buffered saline with Tween-20 (TBST, 0.1M Tris, 0.15M NaCL and 0.1% Tween-20). Blots were then incubated overnight at 4°C in 5% milk TBS-T with HT7 primary antibody (1:2000, MN1000, Invitrogen) and loading control GAPDH (1:20000, G8795, Sigma-Aldrich). The next day blots were washed with TBST and then incubated for 1 h at room temperature in 5% milk TBST with HRP conjugated secondary antibody (1:100000, 115-035-003, Jackson ImmunoResearch Laboratories Inc.). Membranes were developed with enhanced chemiluminescent solution (SuperSignal™ West Pico Plus ECL, 34580, Thermo Scientific) and imaged using FluorChem imaging system (Alpha Innotech Corp). Protein band intensities were then quantified using ImageJ software (NIH, Bethesda, United States). The average intensity of the human total tau (HT7) band over the average intensity of the control band (GAPDH) of the immunoblot were quantified and the results are presented as the HT7/GAPDH ratio.

The second part of the homogenates was ultracentrifuged at 100,000 g for 1 h at 4°C. Supernatant was then recovered and used to measure soluble A β -42 levels using ELISA. The measurements were carried out using the specific Human A β -42 kit (KHB3441, Invitrogen) following the manufacturer's included protocol.

Quantification Algorithms

MR Volumetry

The enhancement in the horizontal plane of the MR images was quantified by volumetric analysis encompassing the hippocampal formations in both hemispheres³⁷. 3D images were normalized with the average reference-intensity obtained from the volume of an out-of-focus structure enhancing the contrast of the Gadolinium-diffuse area. Active contours were

employed²⁴⁵ to isolate the hyperintense area corresponding to the BBB openings on every slice throughout the entire brain by matching the number of slices to the size of the geometric beam according to the acquired resolution. The sum of the pixels enclosed within the contours yielded the area of the BBB opening while performing the analysis over 17 consecutive slices, resulted in the BBB opening volume reported herein³⁷.

Confocal image analysis

The hippocampal formation was isolated from the surrounding brain tissue utilizing the merged-channel images (composite), thus constructing a hippocampal mask. For individual biomarker analysis, the masked composite maximum intensity images were split into the constituent channels. Throughout the rest of this study, the red and green channels represent signal emitted from human total tau and A β 42, respectively.

The structural algorithm previously developed and described in section 5.1.3 was employed herein to quantify the number of cells and the length of the processes affected by tau⁶³. As previously described, the hippocampal mask was constructed and applied onto the red channel followed by k-means segmentation to isolate the highest intensities. The Hough transform enabled the detection of circular objects and the identification of the pathological cell centers. Morphological operators connected the neighboring pixels and skeletonization, revealed the backbone of the processes, the branches and the endpoints. Utilizing the cell center coordinates as the initial point, the algorithm followed the skeleton within a defined neighborhood until reaching all endpoints. The distance of every endpoint to the cell center was measured and the longest 5% of the paths leading to the same cell were measured and averaged.

Estimation of the amyloid plaque volume and population resulting from image quantification was implemented by utilizing the green channel. The entire image was normalized by the average signal emitted from an out-of-focus region, thus enhancing the contrast of the plaques with the surrounding tissue, followed by binarization with a fixed threshold throughout the analysis. The boundaries of the plaques were automatically detected²⁴⁶, the area enclosed within each boundary measured and the volume inferred by the resolution and the in-plane radius of each plaque in MATLAB. The algorithm aside from the plaque volume yielded the location and the population per image.

Statistical analysis

All values are expressed as means \pm standard error of the mean (SEM). Longitudinal analysis of the BBB opening volume was analyzed with multiple Student's t tests. Differences between the means of the sham and treated groups were analyzed using Student's t tests while 2-way repeated measures ANOVA was employed for the MWM analysis. Statistical analysis was performed on the mean value obtained per animal and the P values in the analyses were adjusted based on the Holm Sidak post hoc correction when necessary. All statistical analyses were performed using Prism 8 (Graphpad Software, San Diego, CA, USA) and the null hypothesis was rejected at the 0.05 level. Throughout the manuscript the "F" value in respect to the associated degrees of freedom is provided with the P value adjusted to the corrected multiple t-tests. The significance levels correspond to : * $P \leq 0.05$, ** $P \leq 0.01$, *** $P \leq 0.0005$, **** $P < 0.0001$.

5.2.4 Results and Discussion

In this study, 44 animals (transgenic and non-transgenic) were included in total to assess pathological differences and functional outcomes attributed to the effect of pathological alteration and ultrasound application.

The foremost important aspect of the study was the repeatability of the BBB opening and the bilateral targeting accuracy in this transgenic mouse model. Magnetic resonance imaging revealed consistency in the BBB opening among samples as well as longitudinally across weeks (Figure 28), similar to our previous study⁶³ (section 5.1.4). Quantification of the BBB opening volume in the transgenic animals was measured on the order of $57.5 \pm 8.3 \text{ mm}^3$, $51.4 \pm 12.5 \text{ mm}^3$, $51.00 \pm 9.3 \text{ mm}^3$ and $46.3 \pm 14.2 \text{ mm}^3$ for the four weeks respectively. Statistical analysis confirmed the lack of significant differences in the opening size across weeks, similar to our previous study²⁴⁷, deeming repeated ultrasound suitable for this transgenic mouse model at this age given the technique did not compromise the barrier or initiated any edematous incidences as indicated by the T2-weighted imaging.

Consistency of the BBB opening location and magnitude was necessary to accurately assess behavioral changes associated with the learning rate and short-term spatial memory with contained variance. MWM has been established to detect cognitive changes related to learning and memory given the confinement of the amyloid aggregation and tangle accumulation in the hippocampus, cortex and amygdala, in this specific strain²⁴³. MWM examines the functionality

of the long- and short-term memory that should be significantly impaired at this age (15-16 mo),

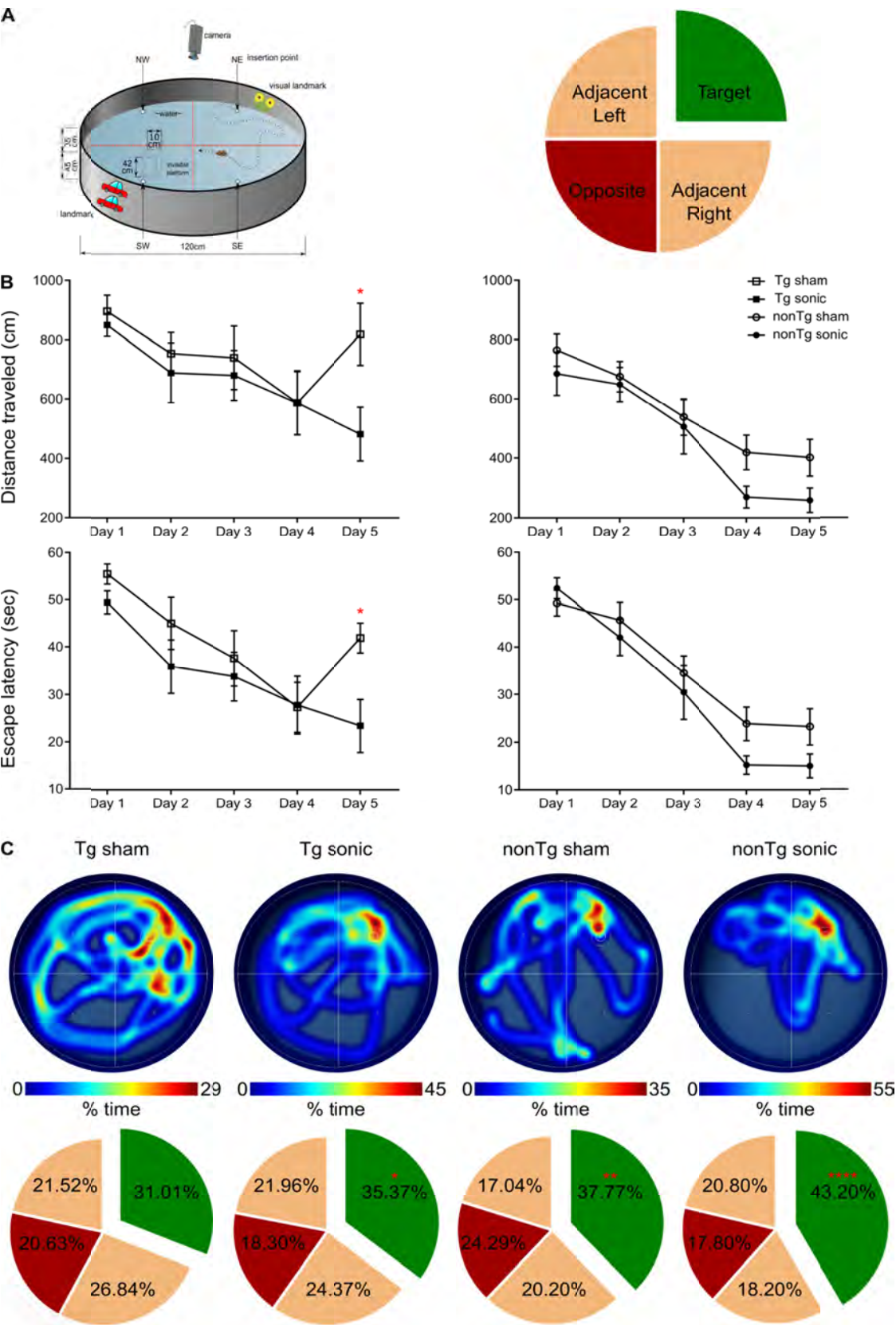


Figure 27: Repeated sonications improve spatial memory in transgenic and non-transgenic mice: A. The schematic of the Morris Water Maze setup that was used to behaviorally examine the animals in respect to their spatial memory functionality. The circular maze is considered to consist of four quadrants, the target, the opposite and the adjacent. B. Learning curves of the escape latency and the distance traveled to find the hidden platform are presented herein and plotted against the days of training. Both the distance traveled ($F[4,144] = 15.57$; $P < 0.0001$) and the escape latency ($F[3,36] = 7.542$; $P = 0.0005$) significantly deteriorated for the sham transgenic animals the last day of the training while all other groups continued to improve. C. Representative individual heatmaps of the time spent in every quadrant followed by the cumulative results on the probe trial. The sham transgenic animals did not show preference over any quadrant while the sonicated transgenic animals spent significantly more time in the target quadrant ($F[1.637, 16.37] = 4.051$; $P = 0.044$). Respectively the non-transgenic mice spent more time in the target quadrant with the sonicated group at a much higher percentage (sham non-transgenic: $F[1.965, 17.68] = 6.375$; $P = 0.0085$, sonicated non-transgenic $F[1.776, 15.99] = 16.48$; $P = 0.0002$).

since the impairment is evident from 6 months of age^{239,240}. To investigate the effect of ultrasound in the cognitive changes detected, non-transgenic mice underwent the same task and three metrics were employed: the escape latency from the maze, the distance traveled from the dropping point to the escape platform and the time spent in each quadrant following the platform removal (probe trial). Mice received four training trials per day for five consecutive days in the spatial version of the MWM shown in the schematic of Figure 27A. For the distance traveled an effect was observed for both days ($F[4,144] = 15.57$; $P < 0.0001$) and groups ($F[3,36] = 7.542$; $P = 0.0005$) suggesting a differentiation in the learning pace (Figure 27B). The sonicated transgenic group reached the escape platform traveling similar distance to the non-transgenic groups (sham and sonicated) while the sham transgenic group traveled significantly more distance until reaching the platform. Equivalent results were obtained for the escape latency with an effect for days ($F[4,144] = 35.71$; $P < 0.0001$) but not for groups, indicative of learning improvement for all groups over the training days with similar learning rates (Figure 27B). Despite the comparable learning pace, the sham transgenic group significantly deteriorated on the fifth day needing more time to escape the maze, while the sonicated transgenic group

remained consistently fast at escaping, similar to the sham non-transgenic and sonicated non-transgenic groups. Two hours after the training trial, a 60 sec probe trial was conducted during which the animals were allowed to spend time in the maze without a hidden platform and the time spent in the target, opposite and adjacent quadrants was measured²⁴⁴. Representative heatmaps from each group show the percent of time spent in the maze followed by the cumulative results (Figure 27C). The sonicated transgenic mice spent significantly more time in the target quadrant compared to the opposite (target:35.37%, opposite:18.30%, adjacent left:21.96%, adjacent right:24.37%; $F[1.637, 16.37] = 4.051$; $P = 0.044$), in contrast to the sham transgenic animals that spent comparable amount of time in every quadrant (target:31.01%, opposite:20.63%, adjacent left:21.52%, adjacent right:26.84%). The percent of time the sham non-transgenic animals spent in the target quadrant was found significantly higher than the opposite (target:37.77%, opposite:24.29%, adjacent left:17.04%, adjacent right:20.20%; $F[1.965, 17.68] = 6.375$; $P = 0.0085$), while the sonicated non-transgenic group spent significantly more time in the target quadrant compared to all other quadrants (target:43.20%, opposite:17.80%, adjacent left:20.80%, adjacent right: 18.20%; $F[1.776, 15.99] = 16.48$; $P = 0.0002$). These data indicate that sonications rescued spatial memory deficits in the transgenic animals while improved the short-term memory performance in non-transgenic mice as well.

Given the beneficial effect of ultrasound on spatial memory established by the improved performance of the sonicated non-transgenic group it is unclear whether the improved functionality observed in the sonicated transgenic mice could be attributed to the ultrasound effect alone or combined with any pathological amelioration.

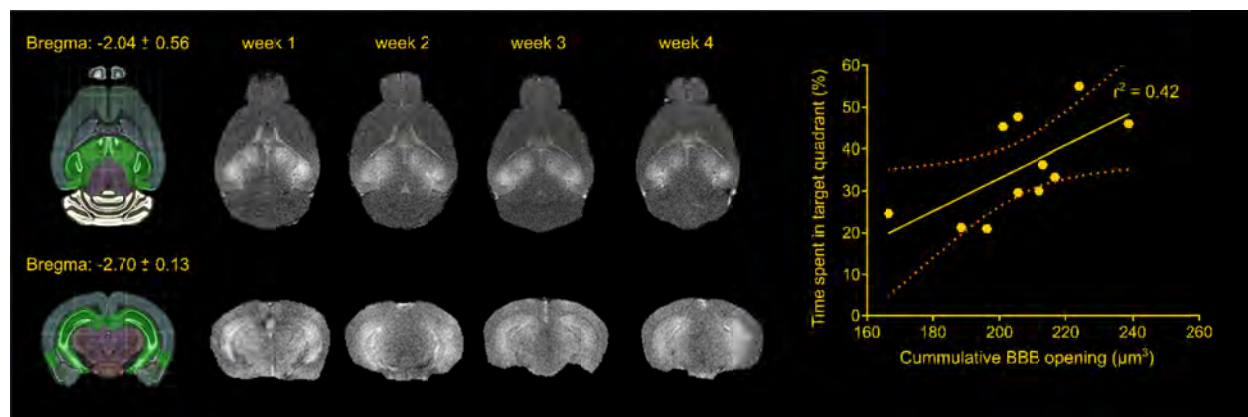


Figure 28: Repeatability of FUS-induced BBB opening and association with behavioral outcomes in the transgenic animals. The BBB opening volume was measured on the order of $57.5 \pm 8.3 \text{ mm}^3$, $51.4 \pm 12.5 \text{ mm}^3$, $51.00 \pm 9.3 \text{ mm}^3$ and $46.3 \pm 14.2 \text{ mm}^3$ for the four weeks respectively. Statistical analysis revealed comparable opening sizes across weeks. Regression analysis between the cumulative BBB opening volume and the time spent in the target quadrant showed a linear relationship ($r^2 = 0.42$) with a significant deviation of the slope from the zero value (slope=0.3941; $F[1.9] = 6.43$; $P = 0.0319$). Brain schematics were constructed using Brain Explorer 2 provided by Allen Brain Atlas.

Interestingly, regression analysis between the cumulative BBB opening volume integrated over the four sonications and the time spent in the target quadrant suggests a linear relationship between the variables ($r^2 = 0.42$) with a significant deviation of the slope from the zero value (slope=0.3941; $F[1.9] = 6.43$; $P = 0.0319$). Thus, cumulative BBB opening could potentially predict the behavioral outcome in terms of short-term spatial memory, a finding that needs to be further explored.

Following the behavioral testing, animals were sacrificed and their brains either processed for immunohistochemistry or homogenized for analytical assays. $A\beta$ immunoreactivity was qualitatively found less pronounced in the transgenic mice that received sonications (Figure 29A) as evidenced by the presence of the $A\beta_{42}$ specific antibody. Plaque quantification revealed a decrease in the volume on the order of 28.4% ($t[7]=1.277$; $P=0.24$) and the population on the

order of 41.14% ($t[7]=1.968$; $P=0.08$) in brains that repeatedly received ultrasound, though

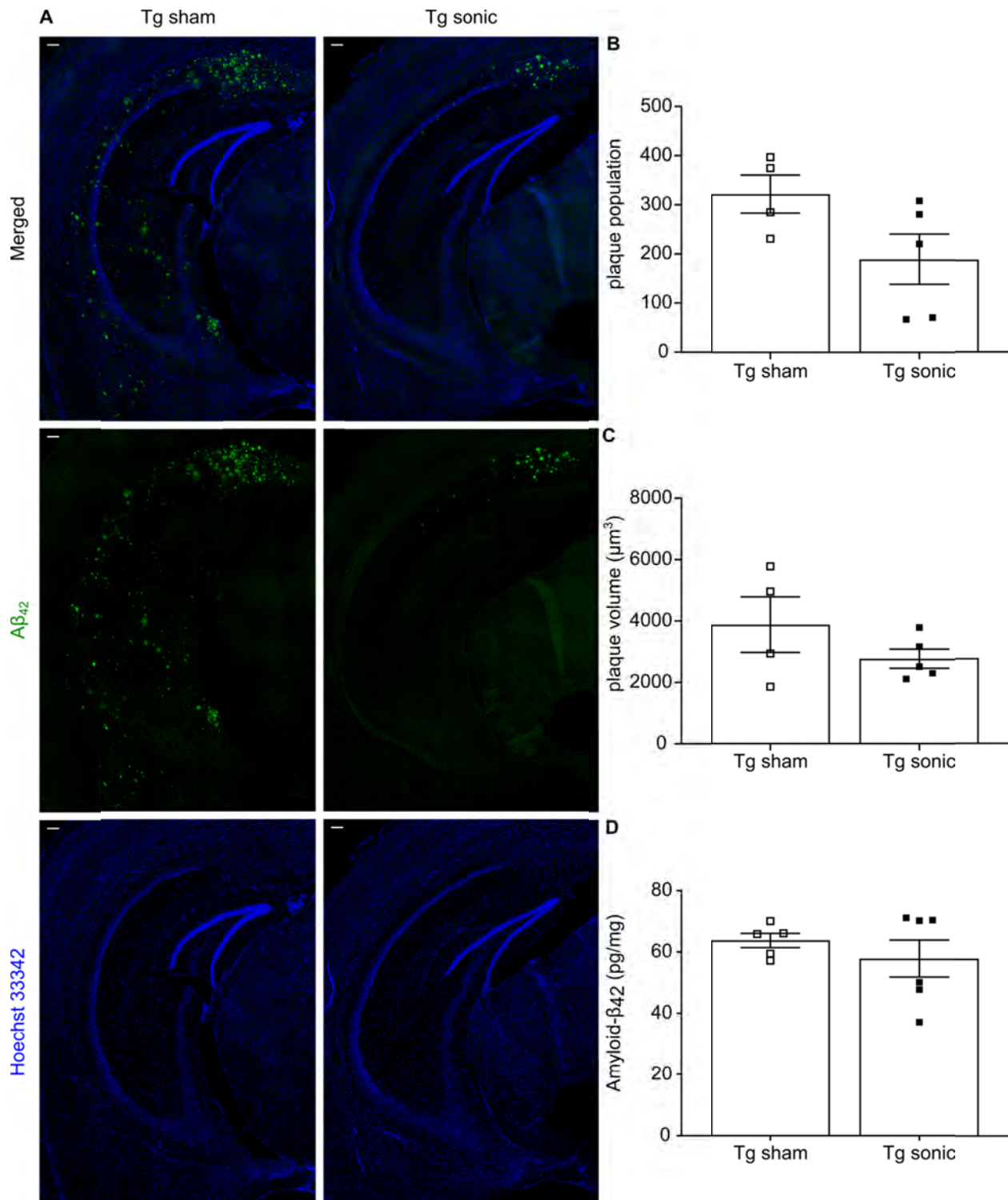


Figure 29: Amyloid plaque quantification. A. A β immunoreactivity was examined using the A β_{42} specific antibody used in both immunohistochemistry and ELISA while Hoechst 33342 was employed for anatomical navigation. **B.** Plaque quantification revealed a

decrease in the population and volume on the order of 41.14% ($t[7]=1.968$; $P=0.08$) and 28.4% ($t[7]=1.277$; $P=0.24$), respectively, in the sonicated brains. Along the same lines, A β 42 quantification with sandwich ELISA confirmed the decreasing trend following sonications by 9.33%, yet lacking significance ($t[9]=0.851$; $P=0.41$). Scale bar: 100 μ m.

neither measure reached significance. Similarly, A β 42 quantification with sandwich ELISA confirmed the decreasing trend following sonications by 9.33%, yet lacking significance ($t[9]=0.851$; $P=0.41$).

Despite the behavioral improvement and its correlation to the volume of BBB opening, the amyloid load in the sonicated brains was not significantly reduced in the presence of tau pathology. To determine whether the beneficial effects of ultrasound in brains with isolated tau pathology observed in previous studies^{63,64} could be observed when amyloid concurrently develops in the hippocampus, we performed immunohistochemical analysis and immunoblotting. Evident from the confocal images is the reduction of human total tau (HT7) protein from the neuronal processes similar to our previous study⁶³. Quantification of the processes' length using the structural algorithm developed herein revealed a significant reduction of the neuronal length affected by tau on the order of 58.31% ($t[6] = 2.802$; $P = 0.0311$). Tau reduction from the hippocampus was confirmed by immunoblot analysis. Taking the ratio of the HT7 over the GAPDH average intensity-band showed a significant reduction in the brains treated with ultrasound compared to the sham group on the order of 27.33% ($t[9] = 3.771$; $P = 0.004$).

Overall, we show that both hallmarks of the AD pathology, human amyloid- β 42 and tau protein, could be mitigated by repeated ultrasound applications. In addition to the significant reduction in tau from the hippocampal formation, the spatial distribution of the pathological marker altered following the application of ultrasound. Neuronal processes were less affected by tau that was

significantly reduced from the brain evidenced by immunoblotting. Concurrent with the beneficial outcomes in tau distribution, the amyloid plaque population, volume and overall load were also decreased, yet the effect was less pronounced and therefore not significant. Ultimately, ultrasound is considered to have attenuated the pathological progression that resulted in functional improvement and especially in the enhancement of short-term spatial memory. However, it is still unclear whether the pathological amelioration or its synergy to the downstream effects following sonication are solely responsible for the behavioral outcomes. Significant improvement in the memory of non-transgenic animals after repeated sonications leaves room for further investigation of the effect ultrasound has on memory cells. Behavioral measures following ultrasound have been previously shown in alert and healthy non-human primates whose reaction time improved by 23 ms and touch error reduced by 0.76 mm while being sonicated⁶⁰. It is the first time tau reduction has been reported and confirmed by both immunoblotting and immunohistochemical image analysis in brains that suffer from amyloid and tau pathology concurrently.

5.2.5 Limitations and Conclusions

This study investigates whether the initial findings of tau reduction in the rTg4510 mouse model that only expresses tau pathology could be replicated in the 3xTg-AD mouse model; in which amyloid- β and tau pathology concurrently affect the hippocampus. Pathological amelioration was confirmed by immunohistochemical analysis as well as immunoassays providing evidence for the elimination of tau from the brain and reduction of amyloid resulting in functional improvement.

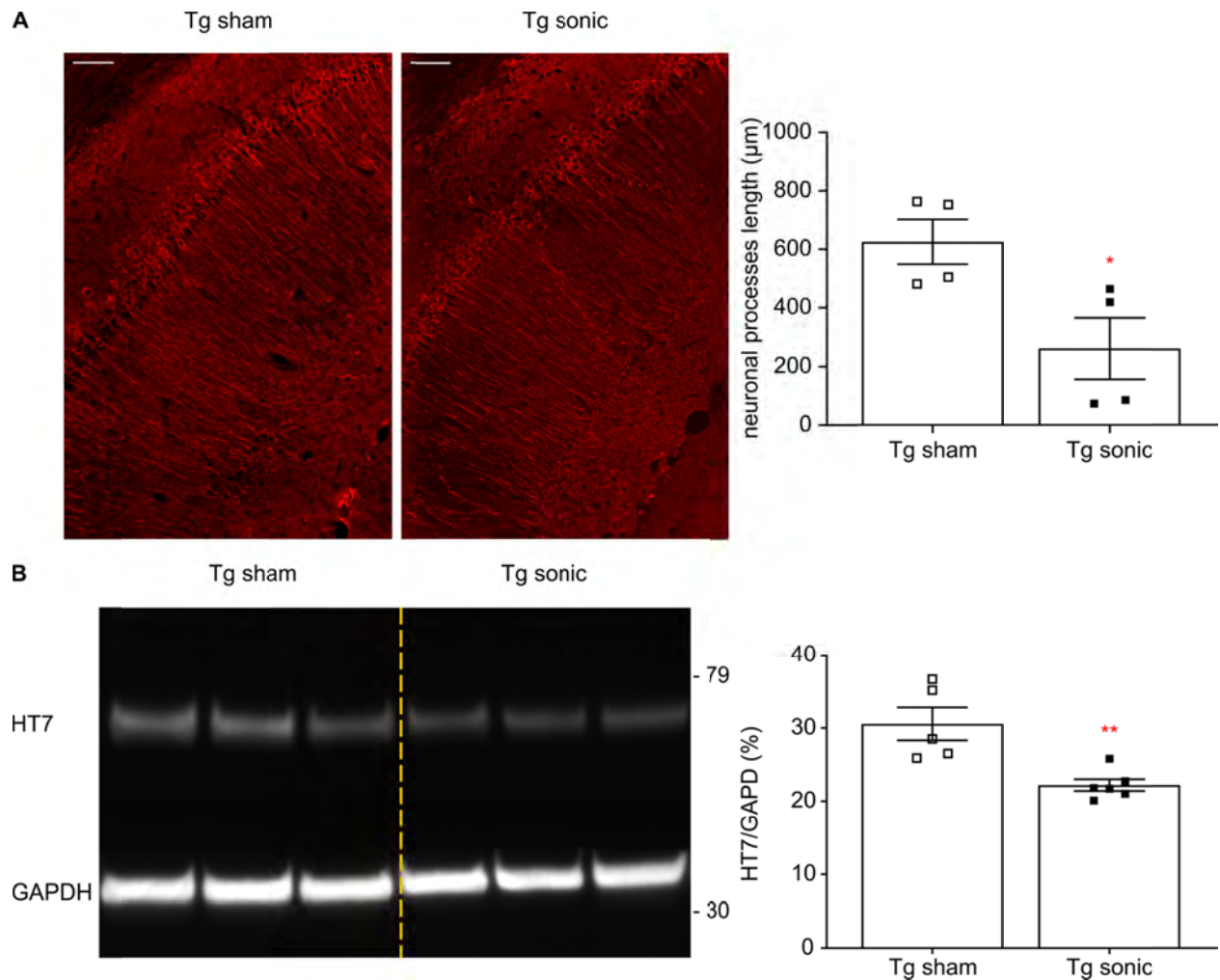


Figure 30: Human total tau quantification. A. Immunohistochemical analysis of the hHT7 antibody detecting human total tau protein revealed a decrease of the neuronal processes affected by tau on the order of 58.31% ($t[6] = 2.802$; $P = 0.0311$). **B.** Tau removal from the hippocampus shown by immunoblot analysis. Taking the ratio of the HT7 over the GAPDH average intensity-band showed a significant reduction in the brains treated with ultrasound compared to the sham group on the order of 27.33% ($t[9] = 3.771$; $P = 0.004$). Scale bar: 100μm.

Despite these promising results, the underlying mechanism triggering such an outcome is still unclear. In chapter 5.1 it was concluded that microglia engulf tau and therefore the ultrasound-triggered immune response should be investigated as a potential mechanism for the tau elimination and amyloid volume and population reduction. However, the timeline of these experiments was longer to accommodate time for the behavioral testing and the immune

response was expected to have returned to normal^{51,53,221} by the time of sacrifice (2-3 weeks post the last sonication). Design of a following set of experiments with a different timeline could shed light on this hypothesis. Moreover, recent findings in the K3 mouse model overexpressing tau pathology that was repeatedly sonicated over the entire brain, pointed towards autophagy as a potential clearance mechanism ruling out ubiquitination of tau²⁴⁸. This path should be further explored for the 3xTg-AD mouse model as well.

5.3 Contribution

A few studies have explored the immunomodulatory effects of FUS-induced BBB opening alone in wild-type^{51,53,221} and transgenic mouse models^{62,64}, characterized by extracellular proteinaceous inclusions.

In the first part of this study, we showed that repeated applications of FUS-induced BBB opening in a transgenic mouse model of Alzheimer's disease overexpressing tau pathology reduced phosphorylated tau from the hippocampus without compromising neuronal integrity. The pathological amelioration was found to be correlated with the induced immune response since microglia were observed to colocalize with phosphorylated tau.

In the second part of this study, we showed that repeated applications of FUS-induced BBB opening in the 3xTg-AD mouse model of Alzheimer's disease, that overexpresses amyloid- β and tau pathology concurrently, simultaneously reduced tau protein and decreased the amyloid- β load. The changes in the pathological protein profiling, along with the concurrent downstream effects following ultrasound, translated functionally into the improvement of spatial memory.

The results of the studies described in this chapter have been published in peer reviewed scientific journals⁶³.

Regarding the research contribution, Maria Murillo, B.A. (Research Associate, Biomedical Engineering, Columbia University) and Tara Kugelman, B.A. (Ph.D. student, Biomedical Engineering, Columbia University) worked on the mouse surgeries, behavioral testing, immunohistochemistry, immunoassays and imaging. Robin Ji developed the cavitation-controlled sonication scheme and assisted in the sonications and MR scanning. Shutao Wang, Ph.D. (Postdoctoral Research Scientist, Biomedical Engineering, Columbia University) helped in the project design, Yusuke Niimi, M.D. (Postdoctoral Research Scientist, Biomedical Engineering, Columbia University) assisted with imaging and Yeh-Hsing Lao, Ph.D. (Postdoctoral Research Scientist, Department of Biomedical Engineering, Columbia University) worked on the immunoassays and their analysis as well as provided us with resources from their lab space. Nancy Kwon, M.A. (Research Associate, Biomedical Engineering, Columbia University) helped acquiring the initial breeding pairs of the 3xTg-AD mice and initiated the colony. Finally, Dr. Scott Small, M.D. (Assistant Professor, Neurology and Pathology, Columbia University) and Dr. Karen Duff (Assistant Professor, Pathology & Cell Biology, Integrative Neuroscience, Columbia University) for their guidance, assistance and directions throughout the entire study.

Chapter 6: Conclusion and Future Work

This dissertation entails the quantitative analysis of the focused ultrasound-induced blood-brain barrier opening with applications in neurodegenerative disorders. In summary, the technique was optimized in terms of targeting and BBB opening volume prediction that could be detected with magnetic resonance imaging in the absence of contrast agents. Along with the method improvement, drug delivery was attempted in rodents resulting in dopaminergic upregulation in Parkinsonian brains. Multiple administrations were shown to have similar outcome measures with single gene delivery. Finally, repeated sonications of two different Alzheimer's mouse models revealed the beneficial immunomodulatory effects of FUS-induced BBB opening that reduced tau pathology in both models accompanied by functional improvement in the latter.

Initially, the relationship between incidence angle and BBB opening volume was studied. The volume of opening normalized with the skull thickness was found to monotonically increase with both close-to-normal incidence angles and peak negative FUS pressure. Anatomically, 80.35% of the opening was found on gray matter regions compared to only 19.41% belonging to the white matter. The opening was found to be shifted axially towards the transducer by 2.36 ± 1.74 mm and laterally by 1.18 ± 1.05 mm. Following these results, the BBB opening volume could be predicted knowing the ultrasound trajectory and the associated skull thickness aside from the applied pressure. Moreover diffusion weighted imaging was developed to detect BBB opening sites revealing a preferred unidirectional flow pattern following the sonication. Fractional anisotropy increased by 82.6% while polar and azimuthal angles decreased by 35.6% and 82.4%, respectively. In conclusion, DTI was deemed a viable alternative to contrast-enhanced MR imaging in brain-related pathologies.

For the next part of this dissertation, we show that FUS-facilitated delivery of neurotrophic factors (either through protein or gene administration) over both the striatum and the ventral midbrain, ameliorates the damage to the nigrostriatal dopaminergic pathway in the sub-acute MPTP mouse model. Briefly, single NTN delivery resulted in the significant upregulation of the nigrostriatal pathway by 20% in the midbrain only, while multiple administrations significantly improved the dopaminergic activity by 22% in the midbrain and 50% in the striatum. Similar findings were shown for the AAV-GDNF delivery that increased TH immunoreactivity in the midbrain by 76% and in the striatum by 32%. Providing evidence on the noninvasive neurotrophic delivery in brains halting the pathological progression could open new therapeutic strategies for the early treatment of neurodegenerative diseases and phenotypic reversal.

For the final part of this dissertation, the immunomodulatory effects of FUS-induced BBB opening were investigated in two animal models of Alzheimer's disease. Amyloid plaques and neurofibrillary tangles constitute the neuropathological hallmarks of the disease while tau pathology is associated with impaired neuronal activity and dementia. Repeated unilateral sonications in brains overexpressing tau pathology reduced the neuronal length affected by tau by 400 μm while maintaining neuronal integrity. Moreover, the 54.41% increase in the presence of immune cells and their engulfment with phosphorylated tau protein following sonications rightfully place them among the suggested mechanisms of pathological clearance. The series of events resulting in the interplay of intracellular tau with extracellular microglia have not been fully identified, yet it has been proposed that low molecular weight tau aggregates can be internalized and externalized transneuronally and/or transcellularly leading eventually to

tauopathy. It is therefore speculated that during this spreading phase, the tau misfolds could be captured by the immune cells¹².

Following such beneficial outcomes, it was pressing to investigate whether such results could be replicated in brains expressing full AD pathology. Therefore, 3xTg-AD mice, concurrently suffering from amyloid plaques and tau pathology, were employed to receive repeated bilateral sonications. Functional improvement was established in the Morris water maze followed by a 58.31% decrease in the neuronal length affected by tau using immunohistochemistry and a 27.2% reduction in tau levels shown by immunoblotting. Amyloid plaque population, volume and overall load were also decreased yet not significantly. Bilateral sonications are shown here for the first time to eliminate tau from the brain and improve the spatial memory of transgenic animals with complex AD phenotype. Given these observation, it is concluded that the synergistic action of tau reduction and the downstream effects of FUS-induced BBB opening triggered the spatial memory enhancement while the insignificant changes of the amyloid plaques are considered to have a diminished contribution. Translation of these findings to the clinic will have to address the compromised vascularity of AD patients' brains. It is currently unknown how a disease-compromised BBB would interact with the microbubbles and the applied acoustic energy, given the vascular changes these patients encounter. However, the first completed phase I clinical trial recruiting AD patients did not report any vulnerability of these brains to the preferred sonication regime¹¹⁶.

Overall, in this dissertation, we established an optimized targeting and detection protocol, pre-clinical implementation of which confirmed its ameliorative effects as a drug-delivery adjuvant

or an immune response stimulant. The trajectory optimization resulting in improved sonication consistency and the equivalent immune response triggered by FUS-induced BBB opening in rodents and non-human primates (Pouliopoulos A. et al. *submitted*) as well as the improved human-disease approximation in animal models suggests a great potential in translating such observations in human subjects.

Ongoing and future work

The promising results of this thesis strongly indicate the potential of this method in the treatment of CNS diseases, especially in a clinical setting. The non-human primate studies along with the encouraging results in the Alzheimer's studies served as the basis on which FDA approved the clinical trials using a neuronavigation-guided system to sonicate 6 AD patients. Despite the trial investigating the safety and feasibility profile of the module, amelioration of the pathology along the same line observed in rodent will be attempted in the future. During the planning session preceding the sonication, it is expected to identify the optimal sonication trajectory including a normal incidence angle and 3D evaluation of the trajectory will be performed. DTI is among the sequences that will be acquired, leading ultimately to the full substitution of Gd-enhanced imaging for such purposes. Increased DTI sensitivity will be accomplished with enhanced gradient strength and increased number of gradient directions that significantly increases the SNR and lowers the detection limit.

Thus, DTI has been proven a valuable tool enabling the detection of the BBB opening in a contrast-free regime. Upon establishment of a diffusion direction from the blood-brain barrier opening with ultrasound, it is intriguing to investigate the local changes in metabolites. Recent

advances in magnetic resonance spectroscopy (MRS) have shown great potential in consistently detecting GABA levels among other molecules in mouse brains by the application of a MEGA-PRESS sequence²⁴⁹. Therefore, investigation of the changes in GABA and other metabolites in mouse brains before and after the initiation of a BBB opening is proposed.

The promising outcome measures of the studies focusing on drug delivery initiated a battery of experiments investigating the efficacy and feasibility of alternative administration routes of neurotrophic factors and antibodies in Parkinsonian animals suffering not only from the toxicity of MPTP but also from α -synuclein inclusions.

As discussed in Chapter 5.2.4 behavioral improvement was not only observed in the transgenic group but in the non-transgenic group that received multiple sonications as well. This finding inspired a new study exploring the downstream effects of ultrasound on memory focusing on the activity of place and grid cells in response to the BBB opening. Moreover, recent findings indicating changes in functional connectivity as detected by fMRI studies should be embedded in the battery of sequences capable to detect pathological changes in the brain. It is also interesting to investigate whether such outcomes can be measured in the absence of BBB opening. Preliminary findings on microglia activation following different sonication regimes reveal a pronounced activation following sonication without microbubble administration as well as sonication at parameters beyond BBB detection at least with MRI's sensitivity limit. In the last figure we show representative examples of the ipsilateral and contralateral sides of groups A-D that received sonications. Briefly, group A encountered a large BBB opening volume beyond the safety window, group B encountered a BBB opening volume using parameters described in

the previous chapters, group C received sonication with microbubbles at PNP on the order of 150

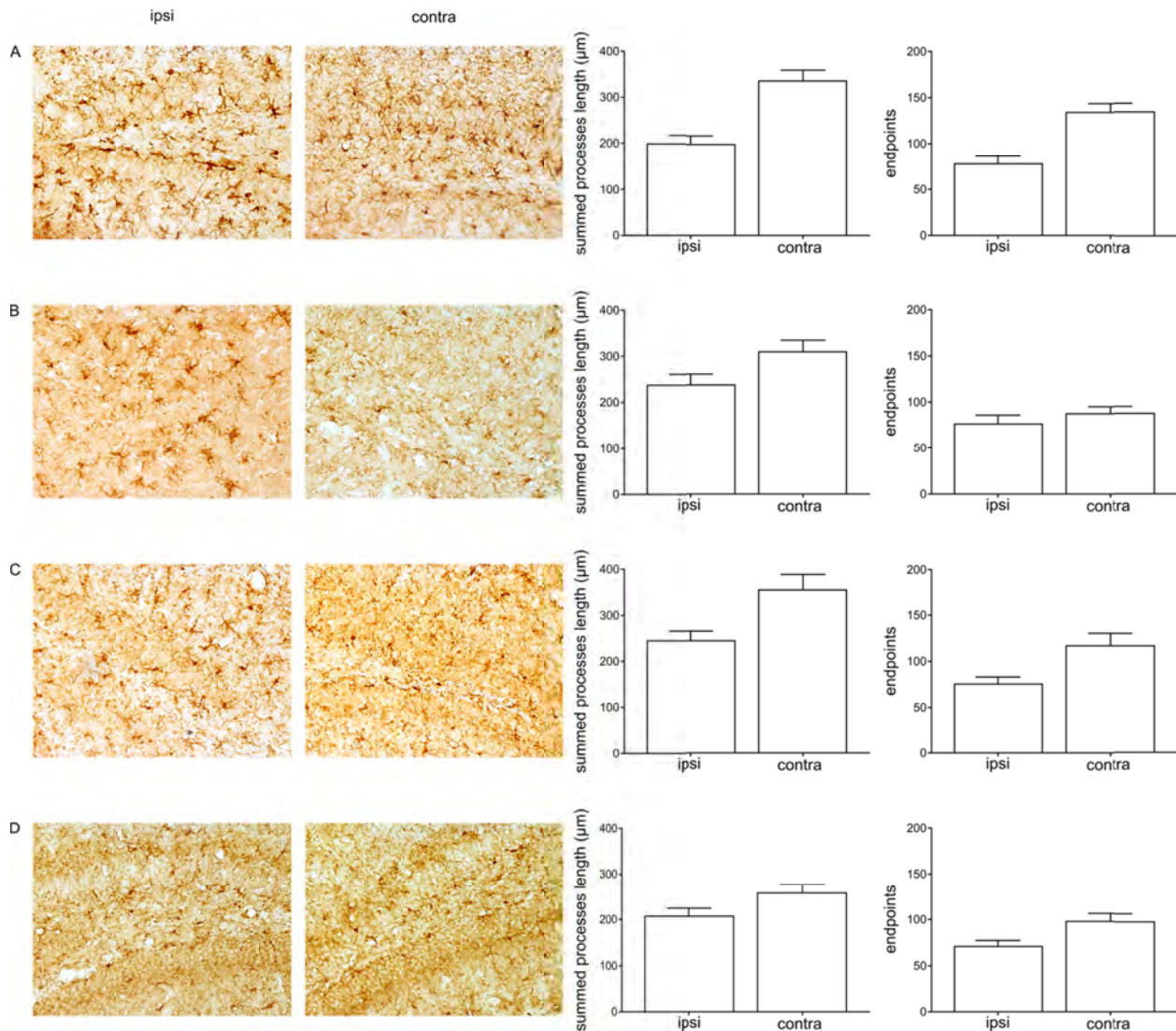


Figure 31: Microglia activation in different sonication regimes. All animals were sacrificed 24 h after the sonication, transcardially perfused and the brains extracted, sectioned and stained with the anti-Iba1 antibody. A. Brains were sonicated at high pressure resulting in large BBB opening volume and pronounced microglia activation shown immunohistochemically. Quantification of the microglia processes' length and the number of endpoint showed a decrease indicative of activation. B. Sonication within the "safety window" results in microglia activation shown qualitatively and quantitatively. C. Animals were sonicated at 150 kPa without a detectable BBB opening. However, the activation of microglia follows the same trend as in the BBB detectable groups, A and B. D. Sonication in the absence of microbubbles at 1 MPa resulted in the activation of microglia without the occurrence of BBB opening.

kPa resulting in undetectable BBB opening and group D received ultrasound in the absence of microbubbles at 1 MPa. Despite the lack of BBB opening in groups C and D, shrinkage of the processes' length and decrease in the number of microglia's endpoints suggest pronounced activation in the hemisphere that received ultrasound similar to groups A and B. These findings are being replicated and expanded to understand the transcriptomic footprint of the acoustic energy at different levels²⁵⁰.

Overall, the take home message of this work is that FUS, methodologically scrutinized and significantly improved herein, could induce BBB openings in different neurodegenerative models and initiate beneficial outcomes either by facilitating delivery of pharmacological agents or by triggering immune downstream effects.

\

References

1. Ransohoff, R. M. & Engelhardt, B. The anatomical and cellular basis of immune surveillance in the central nervous system. *Nat Rev Immunol* **12**, 623–635 (2012).
2. Saunders, N. R., Liddelow, S. A. & Dziegielewska, K. M. Barrier mechanisms in the developing brain. *Front Pharmacol* **3**, 46 (2012).
3. Abbott, N. J. Blood-brain barrier structure and function and the challenges for CNS drug delivery. *J Inherit Metab Dis* **36**, 437–449 (2013).
4. Saunders, N. R., Ek, C. J., Habgood, M. D. & Dziegielewska, K. M. Barriers in the brain: a renaissance? *Trends Neurosci* **31**, 279–286 (2008).
5. Abbott, N. J. Dynamics of CNS Barriers: Evolution, Differentiation, and Modulation. *Cell. Mol. Neurobiol.* **25**, 5–23 (2005).
6. Hawkins, B. T. & Davis, T. P. The blood-brain barrier/neurovascular unit in health and disease. *Pharmacol Rev* **57**, 173–185 (2005).
7. Abbott, N. J., Ronnback, L. & Hansson, E. Astrocyte-endothelial interactions at the blood-brain barrier. *Nat Rev Neurosci* **7**, 41–53 (2006).
8. Przedborski, S., Vila, M. & Jackson-Lewis, V. Series Introduction: Neurodegeneration: What is it and where are we? *J. Clin. Invest.* **111**, 3–10 (2003).
9. Ittner, L. M. & Gotz, J. Amyloid-beta and tau--a toxic pas de deux in Alzheimer's disease. *Nat Rev Neurosci* **12**, 65–72 (2011).
10. Masters, C. L. *et al.* Alzheimer's disease. *Nat Rev Dis Prim.* **1**, 15056 (2015).
11. Selkoe, D. J. & Hardy, J. The amyloid hypothesis of Alzheimer's disease at 25 years. *EMBO Mol Med* **8**, 595–608 (2016).
12. Wu, J. W. *et al.* Small misfolded Tau species are internalized via bulk endocytosis and anterogradely and retrogradely transported in neurons. *J Biol Chem* **288**, 1856–1870 (2013).
13. Bloom, G. S. Amyloid-beta and tau: the trigger and bullet in Alzheimer disease pathogenesis. *JAMA Neurol* **71**, 505–508 (2014).
14. Fu, H. *et al.* Tau Pathology Induces Excitatory Neuron Loss, Grid Cell Dysfunction, and Spatial Memory Deficits Reminiscent of Early Alzheimer's Disease. *Neuron* **93**, 533–541 e5 (2017).
15. Jack Jr., C. R. *et al.* Tracking pathophysiological processes in Alzheimer's disease: an updated hypothetical model of dynamic biomarkers. *Lancet Neurol* **12**, 207–216 (2013).
16. Wang, Y. & Mandelkow, E. Tau in physiology and pathology. *Nat Rev Neurosci* **17**, 5–21 (2016).
17. Holtzman, D. M. *et al.* Tau: From research to clinical development. *Alzheimers Dement* **12**, 1033–1039 (2016).
18. Hegarty, S. V, O'Keefe, G. W. & Sullivan, A. M. Neurotrophic factors: from neurodevelopmental regulators to novel therapies for Parkinson's disease. *Neural Regen Res* **9**, 1708–1711 (2014).
19. Dauer, W. & Przedborski, S. Parkinson's disease: mechanisms and models. *Neuron* **39**, 889–909 (2003).
20. Kalia, L. V & Lang, A. E. Parkinson's disease. *Lancet* **386**, 896–912 (2015).
21. Langston, J. W., Ballard, P., Tetrud, J. W. & Irwin, I. Chronic Parkinsonism in humans due to a product of meperidine-analog synthesis. *Science (80-.)*. **219**, 979–980 (1983).
22. Ishihara, L. S., Cheesbrough, A., Brayne, C. & Schrag, A. Estimated life expectancy of

- Parkinson's patients compared with the UK population. *J Neurol Neurosurg Psychiatry* **78**, 1304–1309 (2007).
23. Pardridge, W. M. BLOOD-BRAIN BARRIER DRUG TARGETING: THE FUTURE OF BRAIN DRUG DEVELOPMENT. *Mol. Interv.* **3**, 90–105 (2003).
 24. Spencer, B. J. & Verma, I. M. Targeted delivery of proteins across the blood-brain barrier. *Proc. Natl. Acad. Sci. U. S. A.* **104**, 7594–9 (2007).
 25. Stockwell, J., Abdi, N., Lu, X., Maheshwari, O. & Taghibiglou, C. Novel Central Nervous System Drug Delivery Systems. *Chem. Biol. Drug Des.* **83**, 507–520 (2014).
 26. Hynynen, K., McDannold, N., Vykhodtseva, N. & Jolesz, F. A. Noninvasive MR imaging-guided focal opening of the blood-brain barrier in rabbits. *Radiology* **220**, 640–646 (2001).
 27. Choi, J. J., Pernot, M., Small, S. A. & Konofagou, E. E. Noninvasive, transcranial and localized opening of the blood-brain barrier using focused ultrasound in mice. *Ultrasound Med. Biol.* **33**, 95–104 (2007).
 28. Ferrara, K., Pollard, R. & Borden, M. Ultrasound Microbubble Contrast Agents: Fundamentals and Application to Gene and Drug Delivery. *Annu. Rev. Biomed. Eng.* **9**, 415–447 (2006).
 29. Feshitan, J. A., Chen, C. C., Kwan, J. J. & Borden, M. A. Microbubble size isolation by differential centrifugation. *J. Colloid Interface Sci.* **329**, 316–324 (2009).
 30. Borden, M. A. *et al.* Influence of lipid shell physicochemical properties on ultrasound-induced microbubble destruction. *IEEE Trans. Ultrason. Ferroelectr. Freq. Control* **52**, 1992–2002 (2005).
 31. Wu, S. Y., Chen, C. C., Tung, Y. S., Olumolade, O. O. & Konofagou, E. E. Effects of the microbubble shell physicochemical properties on ultrasound-mediated drug delivery to the brain. *J Control Release* **212**, 30–40 (2015).
 32. Qin, S. & Ferrara, K. W. Acoustic response of compliant microvessels containing ultrasound contrast agents. *Phys. Med. Biol.* **51**, 5065–5088 (2006).
 33. Tung, Y. S., Choi, J. J., Baseri, B. & Konofagou, E. E. Identifying the inertial cavitation threshold and skull effects in a vessel phantom using focused ultrasound and microbubbles. *Ultrasound Med. Biol.* **36**, 840–852 (2010).
 34. Song, K. H., Harvey, B. K. & Borden, M. A. State-of-the-art of microbubble-assisted blood-brain barrier disruption. *Theranostics* **8**, 4393–4408 (2018).
 35. Chen, H. & Konofagou, E. E. The size of blood-brain barrier opening induced by focused ultrasound is dictated by the acoustic pressure. *J. Cereb. Blood Flow Metab.* **34**, 1197–1204 (2014).
 36. McDannold, N., Vykhodtseva, N. & Hynynen, K. Blood-brain barrier disruption induced by focused ultrasound and circulating preformed microbubbles appears to be characterized by the mechanical index. *Ultrasound Med. Biol.* **34**, 834–840 (2008).
 37. Samiotaki, G., Vlachos, F., Tung, Y. S. & Konofagou, E. E. A quantitative pressure and microbubble-size dependence study of focused ultrasound-induced blood-brain barrier opening reversibility in vivo using MRI. *Magn. Reson. Med.* **67**, 769–777 (2012).
 38. Samiotaki, G. & Konofagou, E. E. Dependence of the Reversibility of Focused- Length In Vivo. **60**, 2257–2265 (2013).
 39. Samiotaki, G., Acosta, C., Wang, S. & Konofagou, E. E. Enhanced delivery and bioactivity of the neurturin neurotrophic factor through focused ultrasound-mediated blood--brain barrier opening in vivo. *J. Cereb. Blood Flow Metab.* **35**, 611–22 (2015).

40. O'Reilly, M. A., Hough, O. & Hynynen, K. Blood-Brain Barrier Closure Time After Controlled Ultrasound-Induced Opening Is Independent of Opening Volume. *J. Ultrasound Med.* **36**, 475–483 (2017).
41. Downs, M. E. *et al.* Correction: Long-term safety of repeated blood-brain barrier opening via focused ultrasound with microbubbles in non-human primates performing a cognitive task. *PLoS One* **10**, (2015).
42. Olumolade, O. O., Wang, S., Samiotaki, G. & Konofagou, E. E. Longitudinal Motor and Behavioral Assessment of Blood–Brain Barrier Opening with Transcranial Focused Ultrasound. *Ultrasound Med. Biol.* **42**, 2270–2282 (2016).
43. Tung, Y. S. *et al.* In vivo transcranial cavitation threshold detection during ultrasound-induced blood-brain barrier opening in mice. *Phys Med Biol* **55**, 6141–6155 (2010).
44. Burgess, M. T., Apostolakis, I. & Konofagou, E. E. Power cavitation-guided blood-brain barrier opening with focused ultrasound. *Phys. Med. Biol.* **63**, 065009 (2018).
45. Pouliopoulos, A. N., Burgess, M. T. & Konofagou, E. E. Pulse inversion enhances the passive mapping of microbubble-based ultrasound therapy. *Appl. Phys. Lett.* **113**, 044102 (2018).
46. McDannold, N., Vykhodtseva, N., Jolesz, F. A. & Hynynen, K. MRI investigation of the threshold for thermally induced blood-brain barrier disruption and brain tissue damage in the rabbit brain. *Magn Reson Med* **51**, 913–923 (2004).
47. Samiotaki, G. *et al.* Permeability assessment of the focused ultrasound-induced blood-brain barrier opening using dynamic contrast-enhanced MRI. *Phys Med Biol* **55**, 5451–5466 (2003).
48. Samiotaki, G. *et al.* Pharmacokinetic analysis and drug delivery efficiency of the focused ultrasound-induced blood-brain barrier opening in non-human primates. *Magn. Reson. Imaging* **37**, (2017).
49. Vykhodtseva, N., McDannold, N. & Hynynen, K. Progress and problems in the application of focused ultrasound for blood-brain barrier disruption. *Ultrasonics* **48**, 279–296 (2008).
50. Han, M., Hur, Y., Hwang, J. & Park, J. Biological effects of blood-brain barrier disruption using a focused ultrasound. *Biomed. Eng. Lett.* **7**, 115–120 (2017).
51. McMahon, D., Bendayan, R. & Hynynen, K. Acute effects of focused ultrasound-induced increases in blood-brain barrier permeability on rat microvascular transcriptome. *Sci. Rep.* **7**, 45657 (2017).
52. Kovacs, Z. I. *et al.* MRI and histological evaluation of pulsed focused ultrasound and microbubbles treatment effects in the brain. *Theranostics* **8**, 4837–4855 (2018).
53. Kovacs, Z. I. *et al.* Disrupting the blood-brain barrier by focused ultrasound induces sterile inflammation. *Proc. Natl. Acad. Sci. U. S. A.* **114**, E75–E84 (2017).
54. Simic, G. *et al.* Tau Protein Hyperphosphorylation and Aggregation in Alzheimer's Disease and Other Tauopathies, and Possible Neuroprotective Strategies. *Biomolecules* **6**, 6 (2016).
55. Hynynen, K., McDannold, N., Sheikov, N. A., Jolesz, F. A. & Vykhodtseva, N. Local and reversible blood-brain barrier disruption by noninvasive focused ultrasound at frequencies suitable for trans-skull sonications. *Neuroimage* **24**, 12–20 (2005).
56. McDannold, N., Vykhodtseva, N., Raymond, S., Jolesz, F. A. & Hynynen, K. MRI-guided targeted blood-brain barrier disruption with focused ultrasound: histological findings in rabbits. *Ultrasound Med. Biol.* **31**, 1527–37 (2005).

57. Choi, J. J., Pernot, M., Small, S. A. & Konofagou, E. E. Noninvasive, transcranial and localized opening of the blood-brain barrier using focused ultrasound in mice. *Ultrasound Med. Biol.* **33**, 95–104 (2007).
58. O'Reilly, M. A., Waspe, A. C., Chopra, R. & Hynynen, K. MRI-guided Disruption of the Blood-brain Barrier using Transcranial Focused Ultrasound in a Rat Model. *J. Vis. Exp.* (2012). doi:10.3791/3555
59. Marquet, F., Tung, Y.-S., Teichert, T., Ferrera, V. P. & Konofagou, E. E. Noninvasive, transient and selective blood-brain barrier opening in non-human primates in vivo. *PLoS One* **6**, e22598 (2011).
60. Downs, M. E., Buch, A., Karakatsani, M. E., Konofagou, E. E. & Ferrera, V. P. Blood-Brain Barrier Opening in Behaving Non-Human Primates via Focused Ultrasound with Systemically Administered Microbubbles. *Sci. Rep.* **5**, 15076 (2015).
61. Jordao, J. F. *et al.* Amyloid-beta plaque reduction, endogenous antibody delivery and glial activation by brain-targeted, transcranial focused ultrasound. *Exp Neurol* **248**, 16–29 (2013).
62. Leinenga, G. & Gotz, J. Scanning ultrasound removes amyloid-beta and restores memory in an Alzheimer's disease mouse model. *Sci Transl Med* **7**, 278ra33 (2015).
63. Karakatsani, M. E. *et al.* Unilateral Focused Ultrasound-Induced Blood-Brain Barrier Opening Reduces Phosphorylated Tau from The rTg4510 Mouse Model. *Theranostics* **9**, 5396–5411 (2019).
64. Nisbet, R. M. *et al.* Combined effects of scanning ultrasound and a tau-specific single chain antibody in a tau transgenic mouse model. *Brain* **140**, 1220–1230 (2017).
65. Pandit, R., Leinenga, G. & Götz, J. Repeated ultrasound treatment of tau transgenic mice clears neuronal tau by autophagy and improves behavioral functions. *Theranostics* **9**, 3754–3767 (2019).
66. Karakatsani, M. E. *et al.* Amelioration of the nigrostriatal pathway facilitated by ultrasound-mediated neurotrophic delivery in early Parkinson's disease. *J. Control. Release* (2019). doi:10.1016/j.jconrel.2019.03.030
67. Mead, B. P. *et al.* Novel Focused Ultrasound Gene Therapy Approach Noninvasively Restores Dopaminergic Neuron Function in a Rat Parkinson's Disease Model. *Nano Lett.* **17**, 3533–3542 (2017).
68. Samiotaki, G. & Konofagou, E. E. Dependence of the reversibility of focused- ultrasound-induced blood-brain barrier opening on pressure and pulse length in vivo. *IEEE Trans. Ultrason. Ferroelectr. Freq. Control* **60**, 2257–2265 (2013).
69. Choi, J. J. *et al.* Noninvasive and transient blood-brain barrier opening in the hippocampus of Alzheimer's double transgenic mice using focused ultrasound. *Ultrason. Imaging* **30**, 189–200 (2008).
70. Chen, H. *et al.* Focused ultrasound-enhanced intranasal brain delivery of brain-derived neurotrophic factor. *Sci. Rep.* **6**, 28599 (2016).
71. Jordão, J. F. *et al.* Amyloid- β plaque reduction, endogenous antibody delivery and glial activation by brain-targeted, transcranial focused ultrasound. *Exp. Neurol.* **248**, 16–29 (2013).
72. Park, J., Aryal, M., Vykhodtseva, N., Zhang, Y.-Z. & McDannold, N. Evaluation of permeability, doxorubicin delivery, and drug retention in a rat brain tumor model after ultrasound-induced blood-tumor barrier disruption. *J. Control. Release* **250**, 77–85 (2017).
73. Fan, C.-H. *et al.* Noninvasive, Targeted and Non-Viral Ultrasound-Mediated GDNF-

- Plasmid Delivery for Treatment of Parkinson's Disease. *Sci. Rep.* **6**, 19579 (2016).
74. Lin, C.-Y. *et al.* Non-invasive, neuron-specific gene therapy by focused ultrasound-induced blood-brain barrier opening in Parkinson's disease mouse model. *J. Control. Release* **235**, 72–81 (2016).
 75. Samiotaki, G., Acosta, C., Wang, S. & Konofagou, E. E. Enhanced delivery and bioactivity of the neurturin neurotrophic factor through focused ultrasound-mediated blood--brain barrier opening in vivo. *J. Cereb. Blood Flow Metab.* **35**, 611–22 (2015).
 76. Wang, S., Olumolade, O. O., Sun, T., Samiotaki, G. & Konofagou, E. E. Noninvasive, neuron-specific gene therapy can be facilitated by focused ultrasound and recombinant adeno-associated virus. *Gene Ther.* **22**, 104–10 (2015).
 77. Kierdorf, K. & Prinz, M. Factors regulating microglia activation. *Front Cell Neurosci* **7**, 44 (2013).
 78. da Fonseca, A. C. *et al.* The impact of microglial activation on blood-brain barrier in brain diseases. *Front Cell Neurosci* **8**, 362 (2014).
 79. Franco, R. & Fernandez-Suarez, D. Alternatively activated microglia and macrophages in the central nervous system. *Prog Neurobiol* **131**, 65–86 (2015).
 80. Perry, V. H., Nicoll, J. A. & Holmes, C. Microglia in neurodegenerative disease. *Nat Rev Neurol* **6**, 193–201 (2010).
 81. Mandrekar, S. & Landreth, G. E. Microglia and Inflammation in Alzheimer's Disease. *CNS Neurol. Disord. Drug Targets* **9**, 156–167 (2010).
 82. Combs, C. K. Inflammation and microglia actions in Alzheimer's disease. *J Neuroimmune Pharmacol* **4**, 380–388 (2009).
 83. Mhatre, S. D., Tsai, C. A., Rubin, A. J., James, M. L. & Andreasson, K. I. Microglial malfunction: the third rail in the development of Alzheimer's disease. *Trends Neurosci* **38**, 621–636 (2015).
 84. Streit, W. J., Braak, H., Xue, Q. S. & Bechmann, I. Dystrophic (senescent) rather than activated microglial cells are associated with tau pathology and likely precede neurodegeneration in Alzheimer's disease. *Acta Neuropathol* **118**, 475–485 (2009).
 85. Qian, L. & Flood, P. M. Microglial cells and Parkinson's disease. *Immunol Res* **41**, 155–164 (2008).
 86. Sheikov, N., McDannold, N., Sharma, S. & Hynynen, K. Effect of focused ultrasound applied with an ultrasound contrast agent on the tight junctional integrity of the brain microvascular endothelium. *Ultrasound Med. Biol.* **34**, 1093–104 (2008).
 87. Choi, J. J., Selert, K., Vlachos, F., Wong, A. & Konofagou, E. E. Noninvasive and localized neuronal delivery using short ultrasonic pulses and microbubbles. *Proc. Natl. Acad. Sci. U. S. A.* **108**, 16539–44 (2011).
 88. Sun, T. *et al.* Acoustic cavitation-based monitoring of the reversibility and permeability of ultrasound-induced blood-brain barrier opening. *Phys. Med. Biol.* **60**, 9079–94 (2015).
 89. McDannold, N., Arvanitis, C. D., Vykhodtseva, N. & Livingstone, M. S. Temporary disruption of the blood-brain barrier by use of ultrasound and microbubbles: safety and efficacy evaluation in rhesus macaques. *Cancer Res* **72**, 3652–3663 (2012).
 90. McDannold, N., Vykhodtseva, N. & Hynynen, K. Effects of acoustic parameters and ultrasound contrast agent dose on focused-ultrasound induced blood-brain barrier disruption. *Ultrasound Med Biol* **34**, 930–937 (2008).
 91. Choi, J. J., Wang, S., Tung, Y. S., Morrison 3rd, B. & Konofagou, E. E. Molecules of various pharmacologically-relevant sizes can cross the ultrasound-induced blood-brain

- barrier opening in vivo. *Ultrasound Med Biol* **36**, 58–67 (2010).
92. Choi, J. J. *et al.* Microbubble-size dependence of focused ultrasound-induced blood-brain barrier opening in mice in vivo. *IEEE Trans Biomed Eng* **57**, 145–154 (2010).
 93. Treat, L. H. *et al.* Targeted delivery of doxorubicin to the rat brain at therapeutic levels using MRI-guided focused ultrasound. *Int J Cancer* **121**, 901–907 (2007).
 94. Samiotaki, G. & Konofagou, E. E. Dependence of the reversibility of focused- ultrasound-induced blood-brain barrier opening on pressure and pulse length in vivo. *IEEE Trans. Ultrason. Ferroelectr. Freq. Control* **60**, 2257–2265 (2013).
 95. Wang, S., Samiotaki, G., Olumolade, O., Feshitan, J. A. & Konofagou, E. E. Microbubble type and distribution dependence of focused ultrasound-induced blood-brain barrier opening. *Ultrasound Med Biol* **40**, 130–137 (2014).
 96. Tung, Y. S., Vlachos, F., Feshitan, J. A., Borden, M. A. & Konofagou, E. E. The mechanism of interaction between focused ultrasound and microbubbles in blood-brain barrier opening in mice. *J Acoust Soc Am* **130**, 3059–3067 (2011).
 97. Marquet, F., Tung, Y. S. & Konofagou, E. E. Feasibility Study of a Clinical Blood-Brain Barrier Opening Ultrasound System. *Nano Life* **1**, 309 (2010).
 98. Marquet, F., Tung, Y. S., Teichert, T., Ferrera, V. P. & Konofagou, E. E. Noninvasive, transient and selective Blood-Brain barrier opening in Non-Human primates in vivo. *PLoS One* **6**, 1–7 (2011).
 99. Samiotaki, G., Vlachos, F., Tung, Y. S. & Konofagou, E. E. A quantitative pressure and microbubble-size dependence study of focused ultrasound-induced blood-brain barrier opening reversibility in vivo using MRI. *Magn Reson Med* **67**, 769–777 (2012).
 100. Marquet, F. *et al.* Real-time, transcranial monitoring of safe blood-brain barrier opening in non-human primates. *PLoS One* **9**, e84310 (2014).
 101. Vlachos, F., Tung, Y. S. & Konofagou, E. E. Permeability assessment of the focused ultrasound-induced blood-brain barrier opening using dynamic contrast-enhanced MRI. *Phys Med Biol* **55**, 5451–5466 (2010).
 102. Deffieux, T. & Konofagou, E. E. Numerical study of a simple transcranial focused ultrasound system applied to blood-brain barrier opening. *IEEE Trans Ultrason Ferroelectr Freq Control* **57**, 2637–2653 (2010).
 103. Arvanitis, C. D., Livingstone, M. S., Vykhotseva, N. & McDannold, N. Controlled ultrasound-induced blood-brain barrier disruption using passive acoustic emissions monitoring. *PLoS One* **7**, e45783 (2012).
 104. Wu, S. Y. *et al.* Transcranial cavitation detection in primates during blood-brain barrier opening--a performance assessment study. *IEEE Trans Ultrason Ferroelectr Freq Control* **61**, 966–978 (2014).
 105. Liu, H. L. *et al.* Hemorrhage detection during focused-ultrasound induced blood-brain-barrier opening by using susceptibility-weighted magnetic resonance imaging. *Ultrasound Med Biol* **34**, 598–606 (2008).
 106. Schneider, U., Pedroni, E. & Lomax, A. The calibration of CT Hounsfield units for radiotherapy treatment planning. *Phys Med Biol* **41**, 111–124 (1996).
 107. Duck, F. A. Chapter 4 - Acoustic Properties of Tissue at Ultrasonic Frequencies. in *Physical Properties of Tissues* (ed. Duck, F. A.) 73–135 (Academic Press, 1990). doi:<https://doi.org/10.1016/B978-0-12-222800-1.50008-5>
 108. Wu, S. Y. *et al.* Efficient Blood-Brain Barrier Opening in Primates with Neuronavigation-Guided Ultrasound and Real-Time Acoustic Mapping. *Sci Rep* **8**, 7978 (2018).

109. Kulik, T., Kusano, Y., Aronhime, S., Sandler, A. L. & Winn, H. R. Regulation of cerebral vasculature in normal and ischemic brain. *Neuropharmacology* **55**, 281–288 (2008).
110. Cavaglia, M. *et al.* Regional variation in brain capillary density and vascular response to ischemia. *Brain Res* **910**, 81–93 (2001).
111. Kinoshita, M., McDannold, N., Jolesz, F. A. & Hynynen, K. Targeted delivery of antibodies through the blood–brain barrier by MRI-guided focused ultrasound. *Biochem. Biophys. Res. Commun.* **340**, 1085–1090 (2006).
112. Samiotaki, G., Acosta, C., Wang, S. & Konofagou, E. E. Enhanced delivery and bioactivity of the neurturin neurotrophic factor through focused ultrasound-mediated blood-brain barrier opening in vivo. *J. Cereb. Blood Flow Metab.* **35**, 611–22 (2015).
113. Burgess, A., Shah, K., Hough, O. & Hynynen, K. Focused ultrasound-mediated drug delivery through the blood-brain barrier. *Expert Rev. Neurother.* **15**, 477–91 (2015).
114. Liu, H.-L. *et al.* Magnetic resonance monitoring of focused ultrasound/magnetic nanoparticle targeting delivery of therapeutic agents to the brain. *Proc. Natl. Acad. Sci. U. S. A.* **107**, 15205–10 (2010).
115. Sun, T. *et al.* Closed-loop control of targeted ultrasound drug delivery across the blood-brain/tumor barriers in a rat glioma model. *PNAS* **114**, E10281–E10290 (2017).
116. Lipsman, N. *et al.* Blood–brain barrier opening in Alzheimer’s disease using MR-guided focused ultrasound. *Nat. Commun.* **9**, 2336 (2018).
117. Carpentier, A. *et al.* Clinical trial of blood-brain barrier disruption by pulsed ultrasound. *Sci. Transl. Med.* **8**, 343re2 LP-343re2 (2016).
118. Abrahao, A. *et al.* First-in-human trial of blood–brain barrier opening in amyotrophic lateral sclerosis using MR-guided focused ultrasound. *Nat. Commun.* **10**, 4373 (2019).
119. Karakatsani, M. E. M., Samiotaki, G. M., Downs, M. E., Ferrera, V. P. & Konofagou, E. E. Targeting Effects on the Volume of the Focused Ultrasound-Induced Blood-Brain Barrier Opening in Nonhuman Primates in Vivo. *IEEE Trans. Ultrason. Ferroelectr. Freq. Control* **64**, 798–810 (2017).
120. Pellerin, M., Yankeelov, T. E. & Lepage, M. Incorporating contrast agent diffusion into the analysis of DCE-MRI data. *Magn. Reson. Med.* **58**, 1124–1134 (2007).
121. Wu, L. *et al.* Dynamic contrast-enhanced (DCE) MRI assessment of microvascular characteristics in the murine orthotopic pancreatic cancer model. *Magn. Reson. Imaging* **33**, 737–760 (2015).
122. Grobner, T. Gadolinium – a specific trigger for the development of nephrogenic fibrosing dermopathy and nephrogenic systemic fibrosis? *Nephrol. Dial. Transplant.* **21**, 1104–1108 (2006).
123. Yang, L. *et al.* Nephrogenic Systemic Fibrosis and Class Labeling of Gadolinium-based Contrast Agents by the Food and Drug Administration. *Radiology* **265**, 248–253 (2012).
124. Kanda, T., Ishii, K., Kawaguchi, H., Kitajima, K. & Takenaka, D. High Signal Intensity in the Dentate Nucleus and Globus Pallidus on Unenhanced T1-weighted MR Images: Relationship with Increasing Cumulative Dose of a Gadolinium-based Contrast Material. *Radiology* **270**, 834–841 (2014).
125. McDonald, R. J. *et al.* Intracranial Gadolinium Deposition after Contrast-enhanced MR Imaging. *Radiology* **275**, 772–782 (2015).
126. Robert, P. *et al.* Methodological Aspects for Preclinical Evaluation of Gadolinium Presence in Brain Tissue: Critical Appraisal and Suggestions for Harmonization - A Joint Initiative. *Invest. Radiol.* **53**, 499–517 (2018).

127. Runge, V. M. Safety of the Gadolinium-based Contrast Agents for Magnetic Resonance Imaging, Focusing in Part on Their Accumulation in the Brain and Especially the Dentate Nucleus. *Invest. Radiol.* **51**, 273–279 (2016).
128. Rasschaert, M. *et al.* Moderate Renal Failure Accentuates T1 Signal Enhancement in the Deep Cerebellar Nuclei of Gadodiamide-Treated Rats. *Invest. Radiol.* **52**, 255–264 (2017).
129. Cao, Y. *et al.* Effect of Renal Function on Gadolinium-Related Signal Increases on Unenhanced T1-Weighted Brain Magnetic Resonance Imaging. *Invest. Radiol.* **51**, 677–682 (2016).
130. Renz, D. M. *et al.* Comparison of Unenhanced T1-Weighted Signal Intensities Within the Dentate Nucleus and the Globus Pallidus After Serial Applications of Gadopentetate Dimeglumine Versus Gadobutrol in a Pediatric Population. *Invest. Radiol.* **53**, 119–127 (2018).
131. Tamrazi, B. *et al.* Changes in Signal Intensity of the Dentate Nucleus and Globus Pallidus in Pediatric Patients: Impact of Brain Irradiation and Presence of Primary Brain Tumors Independent of Linear Gadolinium-based Contrast Agent Administration. *Radiology* **287**, 452–460 (2018).
132. Rasschaert, M. *et al.* Gadolinium Retention, Brain T1 Hyperintensity, and Endogenous Metals. *Invest. Radiol.* **53**, 328–337 (2018).
133. Fretellier, N. *et al.* Does age interfere with gadolinium toxicity and presence in brain and bone tissues?: A comparative gadoterate versus gadodiamide study in juvenile and adult rats. *Invest. Radiol.* **54**, 61–71 (2019).
134. Gale, E. M. & Caravan, P. Gadolinium-Free Contrast Agents for Magnetic Resonance Imaging of the Central Nervous System. *ACS Chem. Neurosci.* **9**, 395–397 (2018).
135. Malheiros, J. M., Paiva, F. F., Longo, B. M., Hamani, C. & Covolan, L. Manganese-Enhanced MRI: Biological Applications in Neuroscience. *Front. Neurol.* **6**, 161 (2015).
136. Massaad, C. A. & Pautler, R. G. Manganese-enhanced magnetic resonance imaging (MEMRI). *Methods Mol. Biol.* **711**, 145–174 (2011).
137. Petcharunpaisan, S., Ramalho, J. & Castillo, M. Arterial spin labeling in neuroimaging. *World J. Radiol.* **2**, 384–398 (2010).
138. Lansberg, M. G. *et al.* Advantages of adding diffusion-weighted magnetic resonance imaging to conventional magnetic resonance imaging for evaluating acute stroke. *Arch. Neurol.* **57**, 1311–6 (2000).
139. Moseley, M. E. *et al.* Diffusion-weighted MR imaging of acute stroke: correlation with T2-weighted and magnetic susceptibility-enhanced MR imaging in cats. *AJNR. Am. J. Neuroradiol.* **11**, 423–9 (1990).
140. Tiwari, Y. V., Lu, J., Shen, Q., Cerqueira, B. & Duong, T. Q. Magnetic resonance imaging of blood–brain barrier permeability in ischemic stroke using diffusion-weighted arterial spin labeling in rats. *J. Cereb. Blood Flow Metab.* **37**, 2706–2715 (2017).
141. Bevers, M. B. *et al.* Apparent Diffusion Coefficient Signal Intensity Ratio Predicts the Effect of Revascularization on Ischemic Cerebral Edema. *Cerebrovasc. Dis.* **45**, 93–100 (2018).
142. Fragata, I. *et al.* Prediction of clinical outcome in subacute subarachnoid hemorrhage using diffusion tensor imaging. *J. Neurosurg.* 1–9 (2018). doi:10.3171/2017.10.JNS171793
143. Filippi, M., Cercignani, M., Inglese, M., Horsfield, M. A. & Comi, G. Diffusion tensor magnetic resonance imaging in multiple sclerosis. *Neurology* **56**, 304–11 (2001).

144. Inglese, M. & Bester, M. Diffusion imaging in multiple sclerosis: research and clinical implications. *NMR Biomed.* **23**, 865–72 (2010).
145. Abbott, N. J., Patabendige, A. A. K., Dolman, D. E. M., Yusof, S. R. & Begley, D. J. Structure and function of the blood-brain barrier. *Neurobiol. Dis.* **37**, 13–25 (2010).
146. Le Bihan, D. *et al.* Diffusion tensor imaging: concepts and applications. *J. Magn. Reson. Imaging* **13**, 534–46 (2001).
147. Bammer, R. Basic principles of diffusion-weighted imaging. *Eur. J. Radiol.* **45**, 169–184 (2003).
148. Mori, S. & Zhang, J. Diffusion Tensor Imaging (DTI). *Encycl. Neurosci.* 531–538 (2009). doi:10.1016/B978-008045046-9.00315-6
149. Mukherjee, P., Berman, J. I., Chung, S. W., Hess, C. P. & Henry, R. G. Diffusion Tensor MR Imaging and Fiber Tractography: Theoretic Underpinnings. *Am. J. Neuroradiol.* **29**, 632–641 (2008).
150. Westin, C. F. *et al.* Processing and visualization for diffusion tensor MRI. *Med. Image Anal.* **6**, 93–108 (2002).
151. Mamata, H. *et al.* High-resolution line scan diffusion tensor MR imaging of white matter fiber tract anatomy. *AJNR. Am. J. Neuroradiol.* **23**, 67–75 (2002).
152. Yamada, K., Sakai, K., Akazawa, K., Yuen, S. & Nishimura, T. MR tractography: a review of its clinical applications. *Magn. Reson. Med. Sci.* **8**, 165–74 (2009).
153. Basser, P. J. & Pajevic, S. Statistical artifacts in diffusion tensor MRI (DT-MRI) caused by background noise. *Magn. Reson. Med.* **44**, 41–50 (2000).
154. Basser, P. J. & Pierpaoli, C. Microstructural and physiological features of tissues elucidated by quantitative-diffusion-tensor MRI. *J. Magn. Reson. B* **111**, 209–19 (1996).
155. Focke, N. K. *et al.* Voxel-based diffusion tensor imaging in patients with mesial temporal lobe epilepsy and hippocampal sclerosis. *Neuroimage* **40**, 728–737 (2008).
156. Moriya, J. *et al.* Gray and white matter volumetric and diffusion tensor imaging (DTI) analyses in the early stage of first-episode schizophrenia. *Schizophr. Res.* **116**, 196–203 (2010).
157. Thivard, L. *et al.* Diffusion tensor imaging and voxel based morphometry study in amyotrophic lateral sclerosis: Relationships with motor disability. *J. Neurol. Neurosurg. Psychiatry* **78**, 889–892 (2007).
158. Steinbrink, C. *et al.* The contribution of white and gray matter differences to developmental dyslexia: Insights from DTI and VBM at 3.0 T. *Neuropsychologia* **46**, 3170–3178 (2008).
159. Arfanakis, K. *et al.* Diffusion tensor MR imaging in diffuse axonal injury. *AJNR. Am. J. Neuroradiol.* **23**, 794–802 (2002).
160. Marchi, N. *et al.* Consequences of Repeated Blood-Brain Barrier Disruption in Football Players. *PLoS One* **8**, (2013).
161. Blackmore, D. G. *et al.* Multimodal analysis of aged wild-type mice exposed to repeated scanning ultrasound treatments demonstrates long-term safety. *Theranostics* **8**, 6233–6247 (2018).
162. Chen, H., Brayman, A. A. & Matula, T. J. Characteristic microvessel relaxation timescales associated with ultrasound-activated microbubbles. *Appl. Phys. Lett.* **101**, 163704 (2012).
163. Avants, B. B. *et al.* A reproducible evaluation of ANTs similarity metric performance in brain image registration. *Neuroimage* **54**, 2033–2044 (2011).
164. Klein, A. *et al.* Evaluation of 14 nonlinear deformation algorithms applied to human brain

- MRI registration. *Neuroimage* **46**, 786–802 (2009).
165. Avants, B. B., Epstein, C. L., Grossman, M. & Gee, J. C. Symmetric diffeomorphic image registration with cross-correlation: evaluating automated labeling of elderly and neurodegenerative brain. *Med. Image Anal.* **12**, 26–41 (2008).
 166. Jenkinson, M., Beckmann, C. F., Behrens, T. E. J., Woolrich, M. W. & Smith, S. M. FSL. *Neuroimage* **62**, 782–790 (2012).
 167. Smith, S. M. Fast robust automated brain extraction. *Hum. Brain Mapp.* **17**, 143–155 (2002).
 168. Andersson, J. L. R. & Sotiropoulos, S. N. An integrated approach to correction for off-resonance effects and subject movement in diffusion MR imaging. *Neuroimage* **125**, 1063–1078 (2016).
 169. Ilovitsh, T. *et al.* Enhanced microbubble contrast agent oscillation following 250 kHz insonation. *Sci. Rep.* **8**, 16347 (2018).
 170. Dayton, P. A., Allen, J. S. & Ferrara, K. W. The magnitude of radiation force on ultrasound contrast agents. *J. Acoust. Soc. Am.* **112**, 2183–2192 (2002).
 171. Koruk, H., El Ghamrawy, A., Pouliopoulos, A. N. & Choi, J. J. Acoustic Particle Palpation for Measuring Tissue Elasticity. *Appl. Phys. Lett.* **107**, 223701–04 (2015).
 172. Kotopoulis, S. & Postema, M. Microfoam formation in a capillary. *Ultrasonics* **50**, 260–8 (2010).
 173. Lazarus, C., Pouliopoulos, A. N., Tinguely, M., Garbin, V. & Choi, J. J. Clustering dynamics of microbubbles exposed to low-pressure 1-MHz ultrasound. *J. Acoust. Soc. Am.* **142**, 3135–3146 (2017).
 174. Pouliopoulos, A. N. *et al.* Rapid short-pulse sequences enhance the spatiotemporal uniformity of acoustically driven microbubble activity during flow conditions. *J. Acoust. Soc. Am.* **140**, 2469–2480 (2016).
 175. Postema, M., Marmottant, P., Lancée, C. T., Hilgenfeldt, S. & de Jong, N. Ultrasound-induced microbubble coalescence. *Ultrasound Med. Biol.* **30**, 1337–44 (2004).
 176. Palanchon, P., Tortoli, P., Versluis, M. & de Jong, N. Optical observations of acoustical radiation force effects on individual air bubbles. *IEEE Trans. Ultrason. Ferroelectr. Freq. Control* **52**, 104–110 (2005).
 177. Pouliopoulos, A. N. & Choi, J. J. Superharmonic microbubble Doppler effect in ultrasound therapy. *Phys. Med. Biol.* **61**, 6154–6171 (2016).
 178. Feinberg, D. A. & Mark, A. S. Human brain motion and cerebrospinal fluid circulation demonstrated with MR velocity imaging. *Radiology* **163**, 793–799 (1987).
 179. Maier, S. E., Hardy, C. J. & Jolesz, F. A. Brain and cerebrospinal fluid motion: real-time quantification with M-mode MR imaging. *Radiology* **193**, 477–483 (1994).
 180. Holdsworth, S. J., Rahimi, M. S., Ni, W. W., Zaharchuk, G. & Moseley, M. E. Amplified magnetic resonance imaging (aMRI). *Magn. Reson. Med.* **75**, 2245–2254 (2016).
 181. Terem, I. *et al.* Revealing sub-voxel motions of brain tissue using phase-based amplified MRI (aMRI). *Magn. Reson. Med.* **80**, 2549–2559 (2018).
 182. Morse, S. V. *et al.* Rapid short pulse ultrasound delivers drugs uniformly across the murine blood-brain barrier with negligible disruption. *Radiology* **291**, 181625 (2019).
 183. Gyöngy, M. & Coussios, C.-C. Passive cavitation mapping for localization and tracking of bubble dynamics. *J. Acoust. Soc. Am.* **128**, EL175-80 (2010).
 184. Haworth, K. J., Bader, K. B., Rich, K. T., Holland, C. K. & Mast, T. D. Quantitative Frequency-Domain Passive Cavitation Imaging. *IEEE Trans. Ultrason. Ferroelectr. Freq.*

- Control* **64**, 177–191 (2017).
185. Lauzon, C. B. *et al.* Simultaneous analysis and quality assurance for diffusion tensor imaging. *PLoS One* **8**, e61737 (2013).
 186. Pouliopoulos, A. N. *et al.* A Clinical System for Non-invasive Blood-Brain Barrier Opening Using a Neuronavigation-Guided Single-Element Focused Ultrasound Transducer. *Ultrasound Med. Biol.* (2019). doi:10.1016/j.ultrasmedbio.2019.09.010
 187. Lin, K. J. *et al.* Quantitative micro-SPECT/CT for detecting focused ultrasound-induced blood-brain barrier opening in the rat. *Nucl Med Biol* **36**, 853–861 (2009).
 188. Fan, C.-H., Lin, C.-Y., Liu, H.-L. & Yeh, C.-K. Ultrasound targeted CNS gene delivery for Parkinson's disease treatment. *J. Control. Release* **261**, 246–262 (2017).
 189. Rosenblad, C. *et al.* Protection and regeneration of nigral dopaminergic neurons by neurturin or GDNF in a partial lesion model of Parkinson's disease after administration into the striatum or the lateral ventricle. *Eur J Neurosci* **11**, 1554–1566 (1999).
 190. Oiwa, Y., Yoshimura, R., Nakai, K. & Itakura, T. Dopaminergic neuroprotection and regeneration by neurturin assessed by using behavioral, biochemical and histochemical measurements in a model of progressive Parkinson's disease. *Brain Res* **947**, 271–283 (2002).
 191. Grondin, R. *et al.* Intraputamenal infusion of exogenous neurturin protein restores motor and dopaminergic function in the globus pallidus of MPTP-lesioned rhesus monkeys. *Cell Transpl.* **17**, 373–381 (2008).
 192. Bartus, R. T. *et al.* Safety/feasibility of targeting the substantia nigra with AAV2-neurturin in Parkinson patients. *Neurology* **80**, 1698–1701 (2013).
 193. Lang, A. E. *et al.* Randomized controlled trial of intraputamenal glial cell line-derived neurotrophic factor infusion in Parkinson disease. *Ann Neurol* **59**, 459–466 (2006).
 194. Salvatore, M. F. *et al.* Point source concentration of GDNF may explain failure of phase II clinical trial. *Exp Neurol* **202**, 497–505 (2006).
 195. Nutt, J. G. *et al.* Randomized, double-blind trial of glial cell line-derived neurotrophic factor (GDNF) in PD. *Neurology* **60**, 69–73 (2003).
 196. Hoffer, B. J. *et al.* Glial cell line-derived neurotrophic factor reverses toxin-induced injury to midbrain dopaminergic neurons in vivo. *Neurosci Lett* **182**, 107–111 (1994).
 197. Horger, B. A. *et al.* Neurturin exerts potent actions on survival and function of midbrain dopaminergic neurons. *J Neurosci* **18**, 4929–4937 (1998).
 198. Taylor, T. N., Greene, J. G. & Miller, G. W. Behavioral phenotyping of mouse models of Parkinson's disease. *Behav Brain Res* **211**, 1–10 (2010).
 199. Sirsi, S. & Borden, M. Microbubble Compositions, Properties and Biomedical Applications. *Bubble Sci Eng Technol* **1**, 3–17 (2009).
 200. Treeby, B. E., Jaros, J., Rendell, A. P. & Cox, B. T. Modeling nonlinear ultrasound propagation in heterogeneous media with power law absorption using a k-space pseudospectral method. *J Acoust Soc Am* **131**, 4324–4336 (2012).
 201. Kamimura, H. A. S. *et al.* Chirp- and random-based coded ultrasonic excitation for localized blood-brain barrier opening. *Phys. Med. Biol.* **60**, 7695–7712 (2015).
 202. Harding, A. J., Halliday, G. M. & Cullen, K. Practical considerations for the use of the optical disector in estimating neuronal number. *J Neurosci Methods* **51**, 83–89 (1994).
 203. West, M. J., Slomianka, L. & Gundersen, H. J. Unbiased stereological estimation of the total number of neurons in the subdivisions of the rat hippocampus using the optical fractionator. *Anat Rec* **231**, 482–497 (1991).

204. Ruifrok, A. C. & Johnston, D. A. Quantification of histochemical staining by color deconvolution. *Anal Quant Cytol Histol* **23**, 291–299 (2001).
205. Smeyne, R. J. *et al.* Assessment of the Effects of MPTP and Paraquat on Dopaminergic Neurons and Microglia in the Substantia Nigra Pars Compacta of C57BL/6 Mice. *PLoS One* **11**, e0164094 (2016).
206. Baquet, Z. C., Williams, D., Brody, J. & Smeyne, R. J. A Comparison of Model-Based (2D) and Design-Based (3D) Stereological Methods for Estimating Cell Number in the Substantia Nigra pars compacta of the C57BL/6J Mouse. *Neuroscience* **161**, 1082–1090 (2009).
207. Frielingsdorf, H., Schwarz, K., Brundin, P. & Mohapel, P. No evidence for new dopaminergic neurons in the adult mammalian substantia nigra. *Proc Natl Acad Sci U S A* **101**, 10177–10182 (2004).
208. Rangasamy, S. B., Soderstrom, K., Bakay, R. A. & Kordower, J. H. Neurotrophic factor therapy for Parkinson's disease. *Prog Brain Res* **184**, 237–264 (2010).
209. Hadaczek, P., Johnston, L., Forsayeth, J. & Bankiewicz, K. S. Pharmacokinetics and bioactivity of glial cell line-derived factor (GDNF) and neurturin (NTN) infused into the rat brain. *Neuropharmacology* **58**, 1114–1121 (2010).
210. Jackson-Lewis, V. & Przedborski, S. Protocol for the MPTP mouse model of Parkinson's disease. *Nat Protoc* **2**, 141–151 (2007).
211. Tatton, N. A. & Kish, S. J. In situ detection of apoptotic nuclei in the substantia nigra compacta of 1-methyl-4-phenyl-1,2,3,6-tetrahydropyridine-treated mice using terminal deoxynucleotidyl transferase labelling and acridine orange staining. *Neuroscience* **77**, 1037–1048 (1997).
212. Tande, D. *et al.* New striatal dopamine neurons in MPTP-treated macaques result from a phenotypic shift and not neurogenesis. *Brain* **129**, 1194–1200 (2006).
213. Nathanson, J. L., Yanagawa, Y., Obata, K. & Callaway, E. M. Preferential labeling of inhibitory and excitatory cortical neurons by endogenous tropism of adeno-associated virus and lentivirus vectors. *Neuroscience* **161**, 441–450 (2009).
214. Yaguchi, M. *et al.* Characterization of the properties of seven promoters in the motor cortex of rats and monkeys after lentiviral vector-mediated gene transfer. *Hum Gene Ther Methods* **24**, 333–344 (2013).
215. Kelly, P. H. & Roberts, D. C. Effects of amphetamine and apomorphine on locomotor activity after 6-OHDA and electrolytic lesions of the nucleus accumbens septi. *Pharmacol Biochem Behav* **19**, 137–143 (1983).
216. Karakatsani, M. E., Blesa, J. & Konofagou, E. E. Blood-brain barrier opening with focused ultrasound in experimental models of Parkinson's disease. *Mov. Disord.* **34**, 1252–1261 (2019).
217. Doody, R. S. *et al.* Phase 3 trials of solanezumab for mild-to-moderate Alzheimer's disease. *N Engl J Med* **370**, 311–321 (2014).
218. Salloway, S. *et al.* Two phase 3 trials of bapineuzumab in mild-to-moderate Alzheimer's disease. *N Engl J Med* **370**, 322–333 (2014).
219. Sevigny, J. *et al.* The antibody aducanumab reduces Aβ plaques in Alzheimer's disease. *Nature* **537**, 50–56 (2016).
220. Jordao, J. F. *et al.* Antibodies targeted to the brain with image-guided focused ultrasound reduces amyloid-beta plaque load in the TgCRND8 mouse model of Alzheimer's disease. *PLoS One* **5**, e10549 (2010).

221. McMahon, D. & Hynynen, K. Acute Inflammatory Response Following Increased Blood-Brain Barrier Permeability Induced by Focused Ultrasound is Dependent on Microbubble Dose. *Theranostics* **7**, 3989–4000 (2017).
222. Liu, H. L. *et al.* In vivo assessment of macrophage CNS infiltration during disruption of the blood-brain barrier with focused ultrasound: a magnetic resonance imaging study. *J Cereb Blood Flow Metab* **30**, 177–186 (2010).
223. Metropolis, N. & Ulam, S. The Monte Carlo method. *J Am Stat Assoc* **44**, 335–341 (1949).
224. Spires, T. L. *et al.* Region-specific dissociation of neuronal loss and neurofibrillary pathology in a mouse model of tauopathy. *Am J Pathol* **168**, 1598–1607 (2006).
225. Wes, P. D. *et al.* Tau overexpression impacts a neuroinflammation gene expression network perturbed in Alzheimer's disease. *PLoS One* **9**, e106050 (2014).
226. Barlow, A. L., Macleod, A., Noppen, S., Sanderson, J. & Guerin, C. J. Colocalization analysis in fluorescence micrographs: verification of a more accurate calculation of pearson's correlation coefficient. *Microsc Microanal* **16**, 710–724 (2010).
227. Gate, D., Rezai-Zadeh, K., Jodry, D., Rentsendorj, A. & Town, T. Macrophages in Alzheimer's disease: the blood-borne identity. *J. Neural Transm.* **117**, 961–970 (2010).
228. Raeside, D. E. Monte Carlo principles and applications. *Phys Med Biol* **21**, 181–197 (1976).
229. James, F. Monte-Carlo Theory and Practice. *Reports Prog. Phys.* **43**, 1145–1189 (1980).
230. Cameron, B. & Landreth, G. E. Inflammation, microglia, and Alzheimer's disease. *Neurobiol Dis* **37**, 503–509 (2010).
231. Jeong, H.-K., Ji, K., Min, K. & Joe, E.-H. Brain inflammation and microglia: facts and misconceptions. *Exp. Neurobiol.* **22**, 59–67 (2013).
232. Dunn, K. W., Kamocka, M. M. & McDonald, J. H. A practical guide to evaluating colocalization in biological microscopy. *Am. J. Physiol. Physiol.* **300**, C723–C742 (2011).
233. Bachmann, M. F., Jennings, G. T. & Vogel, M. A vaccine against Alzheimer's disease: anything left but faith? *Expert Opin. Biol. Ther.* **19**, 73–78 (2019).
234. Cummings, J., Lee, G., Ritter, A., Sabbagh, M. & Zhong, K. Alzheimer's disease drug development pipeline: 2019. *Alzheimer's Dement. (New York, N. Y.)* **5**, 272–293 (2019).
235. Idhah, A. *et al.* Safety and Feasibility of Repeated and Transient Blood–Brain Barrier Disruption by Pulsed Ultrasound in Patients with Recurrent Glioblastoma. *Clin. Cancer Res.* (2019). doi:10.1158/1078-0432.CCR-18-3643
236. Burgess, A. *et al.* Alzheimer Disease in a Mouse Model: MR Imaging–guided Focused Ultrasound Targeted to the Hippocampus Opens the Blood-Brain Barrier and Improves Pathologic Abnormalities and Behavior. *Radiology* **273**, 736–745 (2014).
237. Poon, C. T. *et al.* Time course of focused ultrasound effects on β -amyloid plaque pathology in the TgCRND8 mouse model of Alzheimer's disease. *Sci. Rep.* **8**, 14061 (2018).
238. Drummond, E. & Wisniewski, T. Alzheimer's disease: experimental models and reality. *Acta Neuropathol.* **133**, 155–175 (2017).
239. Billings, L. M., Oddo, S., Green, K. N., McGaugh, J. L. & LaFerla, F. M. Intraneuronal Abeta causes the onset of early Alzheimer's disease-related cognitive deficits in transgenic mice. *Neuron* **45**, 675–688 (2005).
240. Oddo, S. *et al.* Genetically augmenting tau levels does not modulate the onset or progression of Abeta pathology in transgenic mice. *J. Neurochem.* **102**, 1053–1063

- (2007).
241. Yang, M. *et al.* Reduced excitatory neurotransmission and mild autism-relevant phenotypes in adolescent Shank3 null mutant mice. *J. Neurosci.* **32**, 6525–6541 (2012).
 242. Stover, K. R., Campbell, M. A., Van Winssen, C. M. & Brown, R. E. Early detection of cognitive deficits in the 3xTg-AD mouse model of Alzheimer's disease. *Behav. Brain Res.* **289**, 29–38 (2015).
 243. Oddo, S. *et al.* Triple-transgenic model of Alzheimer's disease with plaques and tangles: intracellular Abeta and synaptic dysfunction. *Neuron* **39**, 409–421 (2003).
 244. Caccamo, A., Ferreira, E., Branca, C. & Oddo, S. p62 improves AD-like pathology by increasing autophagy. *Mol. Psychiatry* **22**, 865–873 (2017).
 245. Chan, T. F. & Vese, L. A. Active contours without edges. *IEEE Trans. Image Process.* **10**, 266–277 (2001).
 246. Gonzalez, R. C., Woods, R. E. & Eddins, S. L. *Digital Image processing using MATLAB*. (Pearson/Prentice Hall, 2004).
 247. Karakatsani, M. E., Kugelman, T., Wang, S., Duff, K. & Konofagou, E. Unilateral focused ultrasound-induced blood-brain barrier opening alters spatial profile of hyperphosphorylated tau in an Alzheimer's mouse model. in *IEEE International Ultrasonics Symposium, IUS* (2017). doi:10.1109/ULTSYM.2017.8091655
 248. Pandit, R., Leinenga, G. & Gotz, J. Repeated ultrasound treatment of tau transgenic mice clears neuronal tau by autophagy and improves behavioral functions. *Theranostics* **9**, 3754–3767 (2019).
 249. Guo, J. *et al.* In vivo detection and automatic analysis of GABA in the mouse brain with MEGA-PRESS at 9.4 T. *NMR Biomed* **31**, (2018).
 250. Morrison, H. W. & Filosa, J. A. A quantitative spatiotemporal analysis of microglia morphology during ischemic stroke and reperfusion. *J. Neuroinflammation* **10**, 782 (2013).